Analytical and Computational Methods for Design and Characterization of Materials with Novel Mechanical Properties

By

Chan Soo Ha

A dissertation submitted in partial fulfillment of
the requirements for the degree of

Doctor of Philosophy
(Engineering Mechanics)

at the
University of Wisconsin - Madison
2018

Date of final oral examination: 08/13/2018

The dissertation is approved by the following members of the Final Oral Committee:
Roderic S. Lakes, Professor, Engineering Physics
Michael E. Plesha, Professor, Engineering Physics
Wendy C. Crone, Professor, Engineering Physics
Izabela Szlufarska, Professor, Materials Science and Engineering
Dan Negrut, Professor, Mechanical Engineering

Abstract

Most engineering applications have relied on conventional materials of which their material properties such as elastic moduli, the coefficient of thermal expansion, Poisson's ratio, etc. are considered to be intrinsic. Engineered materials employing dissimilar elements and/or carefully designed geometries, also called as metamaterials (in Greek, the word 'meta' means 'beyond' or 'superior'), can provide material response beyond the limitations of the conventional materials. Hence, they can offer new types of structures with novel properties that are not found in nature. Examples of such extraordinary properties include negative refractive index, negative Poisson's ratio (also known as 'anti-rubber' or 'auxetic'), and negative stiffness. Due to their unique, unprecedented, and beneficial properties, the engineered materials have been of considerable interest in the development of materials with advanced functionalities in various engineering fields such as biomedical sciences, health care, aerospace, automobile, microelectromechanical systems (MEMS), national defense, etc.

This dissertation presents several engineered materials with novel mechanical properties that have been systematically designed and analyzed using various approaches including theory, finite element analysis, and experiment. These newly designed materials are categorized into three overarching themes: 1) Hierarchical structures with controllable thermal expansion. 2) Cosserat structures with advanced functionalities. 3) Energy absorption structure.

The first overarching theme deals with the design and analysis of hierarchical structures with controllable thermal expansion. First, a thermoelastic triangular cell lattice composed of bi-material curved ribs is examined via finite element analysis (FEA) to determine if bonded (or fixed) connections between neighboring ribs can lead to zero thermal expansion. Results have showed that a lattice with bonded joints gives rise to substantial positive thermal expansion regardless of changes in both rib slenderness ratio and rib curvature. A square lattice design utilizing bi-material curved ribs with bonded joints is suggested to achieve zero thermal expansion. Next, a chiral negative

Poisson's ratio lattice with thermal expansion of large magnitude is developed and analyzed by analytical and experimental approaches. Such a lattice consisting of curved bi-metallic rib elements can exhibit thermal expansion larger than that of either constituent in magnitude, and this is shown with a good agreement between the two approaches. Designs for positive, zero, or negative thermal expansion can also be achieved by controlling geometric parameters of the lattice. These two studies in the context of hierarchical structures with controllable thermal expansion have provided useful insights to design dimensionally stable structures subjected to considerable changes in temperature.

For the next overarching theme, several Cosserat structures with novel multi-functional properties are presented. First, a chiral three-dimensional (3D) cubic lattice is developed. This lattice is composed of multiple unit cells exhibiting stretch-twist coupling associated with chirality. FEA following by a customized post-processing developed in MATLAB has revealed that tuning geometry facilitates to control its mechanical properties such as elastic moduli, Poisson's ratio, and stretch-twist coupling. The lattice is then designed to be elastically isotropic to provide a better interpretation and practicability, and this is accomplished by utilizing an elastic relation $E = 2G(1+\nu)$ as a measure of isotropy. The designed chiral 3D isotropic cubic lattice exhibits negative Poisson's ratio and significant size effects in torsion. Such size effects cannot be analyzed by a classical theory of elasticity. Thus, Cosserat elasticity, including additional degrees of freedom which can give rise to a richer framework to describe materials than the classical elasticity, is adopted and have revealed large size effects approaching a factor of five in torsional rigidity. In a similar vein, another Cosserat structure consisting of rotating cubes with pivots at their corners is presented. This structure has unusual behavior in a sense that it is compliant in tension but rigid in torsion and bending. Analytical expressions for strains are derived and compared with that computed from computer-aided design models. Arbitrarily large bulk compliance is verified together with a large negative Poisson's ratio. Due to these unusual behaviors, this structure is not classically elastic but can be considered as an extreme Cosserat solid. According to designs of the present Cosserat structures, various beneficial properties including stiff yet light-weight, stretch-twist coupling, size effect, tailorable mechanical property, and a large negative Poisson's ratio are achievable. Furthermore,

these designs enable to develop and manufacture multi-functional applications without the need of different types of homogeneous materials.

Lastly, a lattice structure capable of energy absorption is designed and investigated numerically and experimentally. The concept of negative stiffness is employed to develop a tetra-beam-plate unit cell exhibiting snap-through behavior to provide energy absorption phenomenon. This unit cell is designed to be elastically stable itself even for the presence of negative stiffness and does not rely on hinges or residual stress. Nonlinear FEA is performed to establish a criterion for designing the unit cell to exhibit the desirable snap-through behavior as a function of the selected geometric parameters. This criterion offers to modify design space such as tailoring the performance of energy absorption capacity and controlling force threshold. According to this criterion, a set of geometric parameters is chosen to create energy absorption lattice structures with different sizes for nonlinear FEA and experiments using physical models fabricated by selective laser sintering (SLS) method. Both numerical and experimental approaches have revealed hysteresis clearly in load-displacement relationships of the designed structure in response to cyclic loading, indicating its energy absorption capability. Moreover, drop tests are performed to quantify energy loss due to impact in terms of the coefficient of restitution. Lower rebound heights are observed for the structure exhibiting the designed snap-through behavior, which demonstrates energy dissipation. Due to its capability to absorb energy, the present lattice structure may be useful in vibration isolators, impact absorbers, protective devices, and so forth.

In summary, newly engineered materials presented in this dissertation can offer access to previously unoccupied material design space that is not achievable by utilizing homogeneous materials solely. Their unprecedented properties may be of considerable interest in diverse engineering applications such as sandwich panel cores, sensors, actuators, dampers, protective devices, etc. Furthermore, they may open up new dimension for designing next-generation engineered materials with advanced functionality.

Contents

List of Figures

List of Tables

List of Abbreviations

AR	aspect ratio
AM	additive manufacturing
ASCII	American standard code for information interchange
BJ	binder jetting
BVS	broadband viscoelastic spectroscopy
CAD	computer-aided design
CLIP	continuous liquid interface production
CNC	computer numerical control
COR	coefficient of restitution
CTE	coefficient of thermal expansion
DOD	drop on demand
DOF	degree of freedom
FDM	fused deposition modeling
FE	finite element
FEA	finite element analysis
FEM	finite element method
FFF	fused filament fabrication
FLM	fused layer modeling/manufacturing
FS	factor of safety
DMLM	direct metal laser melting
DNA	deoxyribonucleic acid

MEMS	microelectromechanical systems
MJ	material jetting
LM	laser melting
LS	laser sintering
PA	polyamide
PEC	polymer engineering center
PLA	polyactic acid or polyactide
PMMA	polymethyl methacrylate
SD	standard deviation
SLA	Stereolithography
SLM	selective laser melting
SLS	selective laser sintering
STL	stereolithography (file format)
WID	Wisconsin institute for Discovery
QZS	quasi-zero-stiffness

Nomenclature

a	cube side length of three-dimensional chiral lattice
a_1, a_2	thickness of material one and two, respectively
α	coefficient of thermal expansion or inclined angle
α	inclined angle of tetra-beam-plate unit cell
AR	aspect ratio of bi-material curved rib
A_{eff}	effective area of three-dimensional chiral lattice
B	strain-displacement matrix
d_{sphere}	diameter of sphere
δ_{ij}	Kronecker's delta
d	outer diameter of circular node of two-dimensional chiral lattice
d	prescribed displacement
d	rib diameter of three-dimensional chiral unit cell
d_{beam}	beam diameter of tetra-beam-plate unit cell
d_{max}	prescribed displacement resulting in fully deformed state
ΔT	uniform temperature change
e	coefficient of restitution
E	elastic modulus
ϵ_{ij}	engineering strain
e_{ijk}	permutation symbol
e_{ij}	small strain tensor
F_{exp}	experimental force magnitude

F_{num}	numerical force magnitude
g	gravitational constant
γ/ϵ_z	twist angle / axial strain
$2h$	height of plate of tetra-beam-plate unit cell
h	total thickness of bi-metallic curved rib
h_0	initial drop height
h_{f}	rebound height
h_{low}	low initial drop height
h_{high}	high initial drop height
I	area moment of inertia
J	polar moment of inertia
K	bulk modulus
L_{arc}	arc length of curved rib
L/a	aspect ratio of three-dimensional chiral lattice
L	center-to-center cube spacing of three-dimensional chiral unit cell
ℓ_b	Cosserat characteristic length for bending
ℓ_t	Cosserat characteristic length for torsion
λ	Lamé constant
L_{rib}	length of bi-metallic curved rib
l_{rib}	rib length of of three-dimensional chiral unit cell
m_{ij}	couple stress tensor
p	multiplier for prescribed displacement
m_{sphere}	mass of sphere
m	thickness ratio of material one to material two
N	coupling number
$N_{\text{snap-through}}$	number of snap-through occurrence

N_{layer}	number of layers in energy absorption lattice
n	elastic modulus ratio of material one to material two
n	number of cells per side of three-dimensional chiral lattice
ν	Poisson's ratio
P	applied point load
ϕ	cube tilt angle of cube structure
ϕ	micro-rotation vector
Ψ	polar ratio
ϕ	rotation of circular node of two-dimensional chiral lattice
r_t	diagonal distance from the center of tetra-beam-plate unit cell to its corner
r_i	macro-rotation vector
ρ_{opt}	optimized radius of curvature
r	outer radius of circular node of two-dimensional chiral lattice
ρ	radius of curvature
ρ	density
r_b	rib radius of three-dimensional chiral unit cell
R	spacing between node centers of two-dimensional chiral lattice
G	shear modulus
G_{asy}	asymptotic (or classical) shear modulus
σ_{ij}	usual Cauchy (or force) stress tensor (asymmetric)
$(\sigma_{\text{equiv}})_{\text{max}}$	maximum equivalent stress
σ_{yield}	yield stress
σ_{ult}	ultimate stress
T	applied torque or moment
θ	included angle of bi-material curved rib
$\tan\delta$	loss tangent

θ_{opt}	optimized included angle of bi-material curved rib
τ	shear stress
t_w	thickness of plate of tetra-beam-plate unit cell
u_i	displacement
v_i	initial velocity
v_f	final velocity
V	volume fraction

Chapter 1

Introduction

1.1 Background information

1.1.1 Controllable thermal expansion

Dimensional stability subject to large temperature change is essential or desirable for various engineering applications, particularly in fields such as aerospace, civil engineering and microelectronics [1]. With such temperature changes, thermal stresses are likely caused by different thermal expansions in components of a structure which contains materials with dissimilar coefficients of thermal expansion (CTE). In extreme thermal surroundings, structures are subject to considerable thermal strains and/or thermo-mechanical fatigue which may result in structural failure. Thermal gradients can also affect dimensional stability in sensitive applications in which precise positioning of parts is critical. A material's CTE is therefore a key consideration when selecting materials for engineering applications with such large gradients in temperature [2]. Thermal expansion for a linear elastic isotropic material with linear thermal expansion properties is described as follows.

$$\epsilon_{ij} = \frac{1+\nu}{E}\sigma_{ij} - \big[\frac{\nu}{E}\sigma_{ij} - \alpha\Delta T\big]\delta_{ij} \tag{1.1}$$

where ν is Poisson's ratio, E is Young's modulus, α is CTE, and δ_{ij} is Kronecker's delta. Thermal expansion of crystalline solids is considered to be an intrinsic property to each material since it is attributed to the anharmonicity (i.e., nonlinearity) of the interatomic potential. Thermal expansion

in common materials tends to decrease with increasing elastic modulus [3]. Some materials such as Zirconium tungstate, $Zr(WO_4)_2$, have negative thermal expansion. Unlike other negative expansion solids, it has negative thermal expansion throughout a temperature range of more than 1000 °C.

Thermal expansion of composite materials had been realized to be bounded by the expansion coefficient of the constituent phases [4]. Particularly, the bounds for α of isotropic composite materials of two solid phases in terms of constituent expansions α_1 and α_2, bulk moduli K_1 and K_2 are as follows.

$$\begin{aligned} \alpha &= \alpha_1 V_1 + \alpha_2 (1 - V_1) \\ \alpha &= \alpha_1 V_1 \frac{K_1}{K} + \alpha_2 (1 - V_1) \frac{K_2}{K} \end{aligned} \tag{1.2}$$

where V_1 is the volume fraction of phase 1 and K is the bulk modulus of the composite. Similarly with the classical Voigt-Reuss and Hashin-Shtrikman bounds that provides limits on the elastic modulus of composites [5] [6] [7], Equation 1.2 assumes that the two phases are perfectly bonded, that there is no porosity, and that each phase has a positive definite strain energy. Such bounds can be useful in the study of complex composites or biological tissues where the structure is so complicated that one cannot readily study the relation between structure and physical properties. If any of the assumptions above is relaxed, arbitrarily large or small values of expansion is possible, which is higher than the upper bound or lower than the lower bound. Three-phase bounds assuming positive definite energy is also possible when allowing void space [8] [9].

Cellular solids include void space (i.e., porosity). Thermal expansion of the cellular solid is the same as that of the solid from which it is made if the ribs (struts) in a foam or honeycomb is homogeneous [10]. With two solid phases and void space, arbitrarily high positive or negative thermal expansion can be achieved in composites [11]. Provided this concept, it is then possible to design composites with high thermal expansion with the aid of topology optimization [12]. Extreme values of expansion can be achieved in dense composites with slip interfaces [13]. Two and three

dimensional cellular solids made of bi-material curved rib elements can give a rise to any desired thermal expansions (such as zero, or large positive, or large negative) [3] [11]. The difference in CTEs leads to bending of the rib in response to temperature change, which results in a decrease of the distance between its ends. This change in length gives rise to the thermal expansion of the lattice as a whole. Large values of piezoelectric sensitivity are also possible; lattices with bi-material piezoelectric elements have been developed and analyzed [14] and investigated experimentally [15].

1.1.2 Cosserat continuum theory

Generalized continuum theories for mechanical behavior allowing degrees of freedom that are not considered in the classical theory of elasticity have developed over the centuries: for example couple stresses, body couples, and local motions by Voigt [16], and E. and F. Cosserat [17]. A key idea of these theories is the Cosserat continuum has six degrees of freedom at each point of a medium.

Mindlin and Tiersten [18] in 1962 introduced the indeterminate couple stress theory in which the rotation of a material point is the same as the local rotation of the surrounding medium; this represents a constrained Cosserat continuum with three degrees of freedom. This constraint leads to the indeterminacy of both the anti-symmetric part of the stress tensor and the spherical part of the couple stress tensor. A characteristic length (i.e., couple stress constant) was introduced in this theory, which is a material property. Classical elasticity is obtained when this length parameter vanishes.

Eringen and Suhubi [19] [20] in 1964 developed a nonlinear theory of microelastic solids that needs 42 constitutive functions of the joint invariants of the kinematic variables to represent the continuum. These 42 functions are reduced to 18 material constants in the linear isotropic forms; Mindlin [21] in 1964 who derived a linear theory via variational principles obtained similar results. The theory by Erigen and Suhubi includes a special case of a linear couple stress if the microrotation tensor and the stress moment tensor are required to be anti-symmetric. Such a constraint is identical to a case when one specifies rigid microelements in an elastic matrix. The linear displacements are kinematically independent of the microrotation, and generalized Cosserat continuum with the six

degrees of freedom is preserved. The stress and couple stress tensors are fully established, and the number of elastic constants is reduced to six. Due to the greater generality of this couple stress theory compared to the Mindlin-Tiersten theory, Eringen [22] in 1966 renamed it as micropolar elasticity.

The constitutive equations for an anisotropic Cosserat elastic solid [23] are as follows.

$$\sigma_{ij} = C_{ijkl}\epsilon_{kl} + P_{ijkl}\phi_{k,l} \tag{1.3}$$

$$m_{ij} = Q_{ijkl}\phi_{k,l} + P_{ijkl}\epsilon_{kl} \tag{1.4}$$

where ϵ_{kl} is the strain tensor, σ_{ij} is the (asymmetric) Cauchy stress tensor, C_{ijkl} is the elastic modulus tensor. m_{ij} is the couple stress tensor in unit of moment per unit area which is asymmetric in general. P_{ijkl} and Q_{ijkl} are Cosserat constants that contribute to sensitivity to local gradient of microrotation vector. The Cosserat microrotation vector ϕ is kinematically independent of the macrorotation vector $r_i = (e_{ijk}u_{k,j})/2$ which is associated with the motion of neighboring points. The usual Einstein summation convention is used and the comma denotes differentiation with respect to ensuring subscripts, which represent Cartesian coordinates.

Cosserat isotropic solids

The constitutive equations of linear isotropic non-chiral micropolar elasticity, considered to be identical to the Cosserat elasticity, are as follows [23].

$$\sigma_{ij} = \lambda\epsilon_{kk}\delta_{ij} + 2G\epsilon_{ij} + \kappa e_{ijk}(r_k - \phi_k) \tag{1.5}$$

$$m_{ij} = \alpha\phi_{k,k}\delta_{ij} + \beta\phi_{i,j} + \gamma\phi_{j,i} \tag{1.6}$$

in which the usual Einstein summation convention is employed and the comma represents differentiation with respect to spatial variables. The constants λ and $(2\mu+\kappa) = 2G$ have the same meaning

as in classical elasticity. σ_{kl} is the (asymmetric) usual (Cauchy or force) stress tensor, m_{ij} is the couple stress tensor (moment per unit area) which is asymmetric in general, $\epsilon_{ij} = \frac{1}{2}(u_{i,j} + u_{j,i})$ is the (symmetric) small strain tensor, u_i is the displacement vector, and e_{ijk} is the permutation symbol. The microrotation vector ϕ_i refers to rotation of points of themselves, while r_i refers to the rotation associated with movement of nearby points.

As described in Equations 1.5 and 1.5, there are six elastic constants for an isotropic Cosserat linear solid (α, β, γ, κ, λ, G) compared with two for the classical solids; α, β, and γ refer to sensitivity to rotation gradients, and κ refers to the degree of coupling between fields. Note that Eringen [23] uses $2\mu + \kappa = 2G$, consequently μ is different from the shear modulus G in this notation. The following technical constants obtained from the tensorial constants are useful in terms of physical insight as follows.

$$\text{Young's modulus } E = \frac{2G(3\lambda + 2G)}{2\lambda + 2G} \tag{1.7}$$

$$\text{Shear modulus } G \tag{1.8}$$

$$\text{Poisson's ratio } \nu = \frac{\lambda}{2(\lambda + G)} \tag{1.9}$$

$$\text{Characteristic length for torsion } \ell_t = \left[\frac{\beta + \gamma}{2G}\right]^{1/2} \tag{1.10}$$

$$\text{Characteristic length for bending } \ell_b = \left[\frac{\gamma}{4G}\right]^{1/2} \tag{1.11}$$

$$\text{Coupling number } N = \left[\frac{\kappa}{2G + \kappa}\right]^{1/2} \tag{1.12}$$

$$\text{Polar ratio } \Psi = \frac{\beta + \gamma}{\alpha + \beta + \gamma} \tag{1.13}$$

The classical solid can be obtained as a special case of the Cosserat solid allowing α, β, γ, κ to tend to zero. The case of $N = 1$ (its upper bound) can be interpreted as couple stress theory [18] [24] [25]. This corresponds to $\kappa \to \infty$, which implies a situation permitted by energetic considerations such as, for example, incompressibility in classical elasticity. In contrast, the case

$\kappa \to 0$, or equivalently, $N = 0$, decouples the rotational and translational degrees of freedom.

In many aspects from a classically elastic solid, a Cosserat solid is predicted to behave differently as follows: dispersion of transverse waves [23], the existence of new types of waves [23], size effects in torsion [26] and in bending [27] of a cylindrical member, a reduction in the concentration of stress around holes [28] [29] [30], a modification of the mode shapes in vibrating bodies [18] and in human compact bone, which is a natural composite material [31].

Cosserat chiral isotropic solids

Chiral materials and structures do not have a center of symmetry (i.e., noncentrosymmetry); they are not invariant to inversion of coordinates. Chirality is not revealed in classical elasticity. For chiral solids viewed as a continuum, which is isotropic with respect to direction, chiral Cosserat constitutive equations are as follows [32].

$$\sigma_{kl} = \lambda\epsilon_{rr}\delta_{kl} + 2G\epsilon_{kl} + \kappa e_{klm}(r_m - \phi_m) + C_1\phi_{r,r}\delta_{kl} + C_2\phi_{k,l} + C_3\phi_{l,k} \tag{1.14}$$

$$m_{kl} = \alpha\phi_{r,r}\delta_{kl} + \beta\phi_{k,l} + \gamma\phi_{l,k} + C_1\epsilon_{rr}\delta_{kl} + (C_2 + C_3)\epsilon_{kl} + (C_3 - C_2)e_{klm}(r_m - \phi_m) \tag{1.15}$$

The elastic constants C_1, C_2 and C_3 denote the effect of chirality. There are nine elastic constant whereas isotropic non-chiral Cosserat elasticity mentioned previously has six. Cosserat elastic constants were determined by analysis of 2D chiral lattices [33] [34] and obtained experimentally in non-chiral foams [35] [36].

New phenomena are predicted qualitatively in chiral materials. A rod deforms in torsion in response to tensile load [32]. Examples of chiral materials include crystalline materials such as quartz and sugar which are chiral on an atomic scale, as well as composites with helical inclusions or spiraling fibers.

Size effects

Classical elasticity has no length scale. Hence, there is no predicted sensitivity to gradients of strain. A structural length scale can be found in composites and foams. This length scale provides experimentally observed size effects; the predictions of classical elasticity do not agree with the rigidity of slender bars or plates. In addition, the toughness of materials has a length scale (in unit of $\mathrm{MPa}\sqrt{\mathrm{m}}$); for example, for foams the toughness is connected with the cell size [10].

Cosserat elasticity, also known as micropolar elasticity, is a continuum elasticity theory that contains a length scale. A size effect is observed in the torsion of circular cylinders of Cosserat elastic materials [26]. Slender cylinders appear stiffer than that expected via classical elasticity. In the bending of plates and of beams, a similar size effect is predicted [27]. In tension, no size effect is predicted since there is no strain gradient. In addition, waves with short wavelength reveal dispersion; the velocity depends upon frequency. Size effects are seen to occur in torsion and bending of foams [36]. A natural composite, human compact bone, also exhibit size effect [37]. In classical elasticity, effective shear modulus is independent of specimen size. This study [37] showed experimentally that the apparent modulus increases significantly as the specimen diameter becomes smaller. In a view of micro-structure, twist of each individual osteon as a large fiber that contributes to the twisting moment.

An isotropic Cosserat solid has six elastic constants, as given in Equations 1.5 and 1.6, and these constants can be obtained from size effect experiments [38] [39]. As these constants tend to zero, the characteristic lengths also tend to zero, and the Cosserat elasticity becomes classical elasticity for which there is no characteristic length. The stress concentration factor for a circular hole is seen to be smaller in composites compared to a value via classical elasticity, and larger holes exhibit more stress concentration than small ones. Cosserat elasticity can predict such situations.

1.1.3 Negative Poisson's ratio

Classical isotropic solids may be described using two elastic constants, Young's modulus E and Poisson's ratio ν. While Young's modulus is considered to be a measure of stiffness and has a wide

range from several KPa for soft materials to 1 TPa for diamond, Poisson's ratio is typically between 0.25 and 0.35 for most common materials and approaches 0.5 for rubbery materials. Poisson's ratio is practically important since it governs the deformation fields of elastic objects. Poisson's ratio also influences wave speeds in a material. Longitudinal waves propagate much faster than shear waves if Poisson's ratio is large. In contrast, a small Poisson's ratio leads to shear waves propagate faster than longitudinal waves [40].

Poisson's ratio, named after a French mathematician Siméon Denis Poisson [41], is defined as the ratio of transverse contraction strain to longitudinal extension strain in the direction of stretching force.

$$\nu = -\frac{\epsilon_{\text{transverse}}}{\epsilon_{\text{longitudinal}}} \tag{1.16}$$

where ϵ is the change in length divided by the original length as defined in elementary form. Nearly all ordinary materials have a positive Poisson's ratio. That is, they become smaller in cross-section when stretched and larger when compressed. For example, a rubber band becomes narrower in cross section when it is stretched.

Negative Poisson's ratio is permissible theoretically. Materials with $-\nu$ expand laterally subjected to tensional load. Foams with ν as small as -0.7 with enhanced resilience [42] [43], α-cristobalite with ν equal to -0.16 [44], a planar chiral lattice with ν equal to -1 [45], cubic elemental metals exhibiting $-\nu$ in the [110] direction [46], and metamaterials with negative Poisson's ratio and bistability based on reentrant origami [47] have been made. Negative Poisson's ratio materials are often termed as 'anti-rubber' in a *New York Times* survey [48] of the 1987 *Science* article [42], 'auxetics' [49], and 'dilational' [50]. The term 'dilational' arises from the fact that negative Poisson's-ratio-materials easily undergo volume changes but are stiff to shear. In contrast, rubbery materials are stiff in relation to volume change (i.e., resist volumetric (bulk) deformation) but readily undergo shape changes (i.e., shear deformation). Theoretically, the allowable range of Poisson's ratio for three-dimensional isotropic solids is from -1 to $\frac{1}{2}$ [2]. This is based on intrinsic structural

stability of materials in view of energy considerations [51]. A stable material with free surfaces must be in a minimum energy state at zero strain. The bulk modulus B and shear modulus G must be greater than zero for an isotropic solid with free surfaces to be stable under conditions of prescribed surface load. For isotropic objects, four common elastic constants (E, G, B, and ν) are interrelated. For example, the Young's modulus is $E = 2G(1+\nu)$, the bulk modulus is $B = 2G\frac{1+\nu}{3(1-2\nu)}$. Thus, to be stable, the range of Poisson's ratio for isotropic solids with free surfaces and with no constraints is $-1 < \nu < \frac{1}{2}$. In contrast, Poisson's ratio for anisotropic materials is not as limited as compared to that of isotropic materials. For solids having sufficient anisotropy, Poisson's ratio can occur in a range from $-\infty$ to ∞. The negative Poisson's ratio effect is not from Cosserat elasticity. The classical theory of elasticity has no length scale. Negative Poisson's ratio does not require the characteristic length scale appears in Cosserat or micropolar elasticity.

1.1.4 Negative stiffness

For most elastic materials, stiffness is positive (i.e., positive force to displacement ratio). That is, these materials tend to resist deflection or deformation by an applied force. Negative stiffness is a counter-intuitive phenomenon that entails a reversal of the usual directional relationship between force and displacement, and it can occur in pre-strained objects such as models of single foam cells [43], buckled flexible tubes forming kinks (which contain stored energy at a state of equilibrium) [52], and lumped systems containing discrete buckled tubes [53].

An object or structure with negative stiffness is usually unstable itself. A constrained buckled column with 'S'-shaped configuration is in unstable equilibrium [54]. However, a structure may be stable if constrained under some circumstances. For snap-through response due to negative stiffness which can be caused by pressing laterally on the column, one can stabilize the column with a lateral constraint. Structures with negative stiffness can also be stabilized by incorporation in heterogeneous materials or composites. This process can offer extreme values of physical properties. For example, a lumped system composed of discrete buckled tubes exhibits both tunable negative

stiffness and resulting extreme damping [53], composites with negative stiffness inclusions in a viscoelastic matrix give rise to higher stiffness and mechanical damping than that of either constituent [55], a composite made of a pure tin matrix with negative stiffness inclusions of ferroelastic vanadium dioxide results in extreme (viscoelastic) mechanical damping and large anomalies in stiffness [56], particulate composites with a negative stiffness inclusions in a viscoelastic matrix display extreme thermal expansion and other extreme linear coupled filed properties such as piezoelectricity and pyroelectricity [57], composites made with a small volume fraction of negative stiffness inclusions disclose overall stiffness much higher than that of either constituent [58], a simple spring model with pre-load to exhibit negative stiffness gives rise to extreme overall stiffness [59], composite materials with negative stiffness due to constraint upon a phase transformation disclose material properties greater than those of either constituent [60], and composite materials containing barium titanate inclusions in a tin matrix exhibit a viscoelastic (Young's) modulus much higher than that of either constituent and stiffer than diamond over a narrow temperature range [61].

These extreme behaviors exceed classical bounds [62], where composite properties cannot exceed the properties of the constituents. Such bounds are based on theorems assuming that each constituent does not have initial stored energy. In contrast, an object with negative stiffness initially contains stored energy; composite stability can be enhanced by viscoelastic dissipation, if present [61].

Recently, due to its unique and beneficial aspect, negative stiffness behavior has been of considerable interest in various engineering applications [63] including energy harvesting/dissipation [64] [65] [66] [67] [68], shock/vibration isolation and damping [69] [70] [71] [72] [73] [74] [75], and sensitivity enhancement [76] [77] [78].

1.2 Thesis organization

This dissertation presents the development and characterization of materials with novel mechanical properties and contains three main themes: 1) Hierarchical structures with controllable thermal

expansion. 2) Cosserat structures with advanced functionalities. 3) Energy absorption structure.

Chapters 2 and 3 provide the design and analysis of hierarchical structures with controllable thermal expansion. First, the feasibility of zero thermal expansion for a thermoelastic triangular cell lattice with fixed (or bonded) joints is examined in Chapter 2. This lattice is composed of bi-material curved ribs to control thermal expansion due to bending of the ribs. Finite element analysis (FEA) utilizing a commercial code called ANSYS APDL is adopted to explore the effects of joint conditions on the lattice. The effects of both rib curvature and rib slenderness ratio are also investigated. By extending the idea of hierarchical structures with controlling thermal expansion in another direction, a chiral negative Poisson's ratio lattice with thermal expansion of large magnitude is presented in Chapter 3. This lattice utilizes bi-metallic rib elements and circular nodes to achieve control of thermal expansion. Using geometric relations of the lattice together with Timoshenko's beam theory, analytical expressions that predict the thermal expansion coefficient of an individual bi-metallic rib element are derived. Laboratory experiment is performed to validate the analytical result.

Cosserat structures with advanced functionalities are presented in Chapter 4 through 6. First, the development and characterization of a chiral three-dimensional (3D) cubic lattice are discussed in Chapter 4. This lattice contains multiple unit cells that consist of deformable beams and rigid cubical nodules. A design of this unit cell is inspired by the shape of deoxyribonucleic acid (DNA) to employ chirality giving rise to stretch-twisting coupling in response to external stimulus. Geometric dependency of mechanical properties and Cosserat effects are examined by FEA following by a customized post-processing developed in MATLAB. In Chapter 5, a similar analysis as Chapter 4 is performed but focuses on designing elastically isotropic Cosserat solids. Size effects in torsion are studied in accord with Cosserat elasticity. In Chapter 6, another 3D Cosserat structure consisting of cubes connected by pivots at their corners is presented. This structure is designed to undergo arbitrarily large volumetric changes while it is compliant in tension but rigid in torsion and bending. Hence, it has zero Young's modulus and zero bulk modulus. To validate this behavior, analytical expressions predicting strains are derived and compared to that computed from 3D computer-aided

design (CAD) models created by a commercial CAD software SolidWorks.

The last main theme of the development and analysis of an energy absorption lattice structure is discussed in Chapter 7. A design of a tetra-beam-plate unit cell exhibiting snap-through behavior is proposed by utilizing negative stiffness from geometric nonlinearities caused by large deflection of the constituent beams. Nonlinear FEA is employed to establish a criterion for designing the unit cell to exhibit the desirable snap-through behavior as a function of the selected geometric parameters of the unit cell. This criteria is then used to choose a set of geometric parameters of the unit cell to create energy absorption structures for numerical and experimental studies. Physical models representing such structures are fabricated by selective laser sintering (SLS) method. The two studies are demonstrated to reveal energy absorption capability of the designed structures which is indicated by hysteresis in the load-displacement relationships in response to cyclic loading. Correlation analysis between the two approaches is performed, and energy loss due to impact in terms of the coefficient of restitution is investigated by performing drop tests.

Lastly, Chapter 8 makes concluding remarks regarding the work presented in this dissertation and covers future work in this research area.

Chapter 2

Simulations of thermoelastic triangular cell lattices with bonded joints by finite element analysis

The following chapter has been published:
C. Ha, M. E. Plesha, and R. S. Lakes, "Simulations of thermoelastic triangular cell lattices with bonded joints by finite element analysis", Extreme Mechanics Letters, 12, 101-107 (2017).

Abstract Thermoelastic triangular cell lattices composed of bi-material curved ribs were designed and analyzed by finite element simulation. Positive, negative, or zero thermal expansion was possible by varying rib curvature if joints can pivot freely, as expected. Welded or bonded joints result in nonzero expansion but smaller in magnitude than that of a constituent material having higher thermal expansion coefficient. The effects of rib curvature variation for bonded joints were found to be negligible. Rib slenderness for both joints did not influence the coefficient of thermal expansion. We present a square lattice with bonded joints that has zero net thermal expansion; each curved bi-material rib has zero expansion.

2.1 Introduction

Various engineering structures in fields such as aerospace, civil engineering, and microelectronics often undergo large temperature changes [1]. They lead to thermal stresses caused by different thermal expansions in components of a structure which are made of materials with dissimilar coefficients of thermal expansion. In the field of aerospace, supersonic and hypersonic vehicles exhibit significant thermal stresses, and thermodynamic propulsion plants also experience similar stresses [79]. For these structures, dimensional stability (i.e., structural integrity) is surely a key consideration. An example of the importance of dimensionally stable design of structures is the Hubble space telescope; considerable thermal distortions were produced by rapid temperature changes during its orbit, which led to undesired vibration of the telescope and the arrays [80]. A material's coefficient of thermal expansion is thus clearly one of the driving factors when selecting materials for structures subject to large fluctuations in temperature [2].

Materials of zero or minimal thermal expansion can provide dimensionally stable designs of structures subject to large temperature change. For example, zero or nearly zero thermal expansion is desirable in fields in which precise positioning of parts is critical, such as optics and electronics [81]. Similarly, aerospace and civil engineering applications, like piping systems designed with tight dimensional tolerances, are required to have minimal or zero thermal expansion for achieving dimensional stability under extreme variation in temperature [82]. By contrast, materials exhibiting negative thermal expansion are of interest for applications need to contract with increases in temperature [83]. It is also possible to control any desired thermal expansions (such as zero, or large positive, or large negative) in composite materials with void spaces by tuning design of their microstructure [11] [84].

Recently, Lehman and Lakes [85] showed that zero coefficient of thermal expansion in a lattice made of bi-material curved rib elements can be achieved by designing hierarchical material structures with carefully chosen geometry and materials while optimizing the total mechanical stiffness of a thermoelastic triangular lattice, as shown in Figure 2.1. Two different metals with different positive

thermal expansion coefficients were used to design this microstructure, which is composed of ribs whose cross section was rectangular. The difference in thermal expansion coefficients leads to bending of the rib during temperature change, which results in a decrease of the distance between its ends which is exactly counterbalanced by overall thermal expansion of the rib. By carefully tuning geometric parameters of the bi-material curved rib, zero net thermal expansion in a honeycomb or lattice structure can be achieved. An overall thermal expansion coefficient for an individual bi-material curved rib element with pin-ended joints, as depicted in Figure 2.2, is provided by Equation 2.1 [85]. The derivation of this equation was based on Timoshenko's work for bi-material strips [86]

$$\begin{aligned}\alpha_{net} = (\alpha_1 - \alpha_2)\frac{L_{arc}}{t}\Big(\frac{\theta}{12}\Big)\frac{6(1+m^2)}{3(1+m)^2+(1+mn)(m^2+\frac{1}{mn})} \\ + \ \frac{\alpha_1+\alpha_2}{2} \ + \ (\alpha_2-\alpha_1)\Big[\frac{4m^2+3m+\frac{1}{mn}}{nm^3+4m^2+6m+\frac{1}{mn}+4}-\frac{1}{2}\Big]\end{aligned} \tag{2.1}$$

where α_1 and α_2 are the thermal expansion coefficients of material one and two, respectively, E_1 and E_2 are the elastic modulus of material one and two, respectively, L_{arc} is the arc length of the curved rib, m is the thickness ratio of material one to material two (i.e., $m = \frac{a_1}{a_2}$), n is the elastic modulus ratio of material one to material two (i.e., $n = \frac{E_1}{E_2}$), θ is the included angle and t is the total thickness of the rib. In order to obtain zero coefficient of thermal expansion, material one, positioned on the inner portion of the curved rib, is required to have a smaller thermal expansion coefficient than material two on the outer portion. Invar was used as material one, while material two was steel, and their material properties are given in Table 2.1.

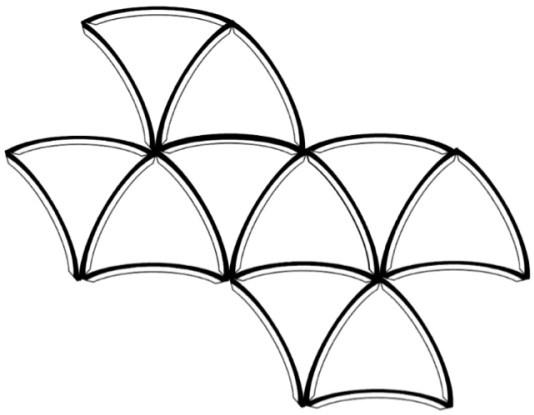

FIGURE 2.1: The equilateral triangular lattice composed of bi-material curved ribs [85]. Material one with a lower coefficient of thermal expansion is shown as white (on the inner portion of each rib), while material two with a higher coefficient of thermal expansion is shown as black (on the other portion of each rib).

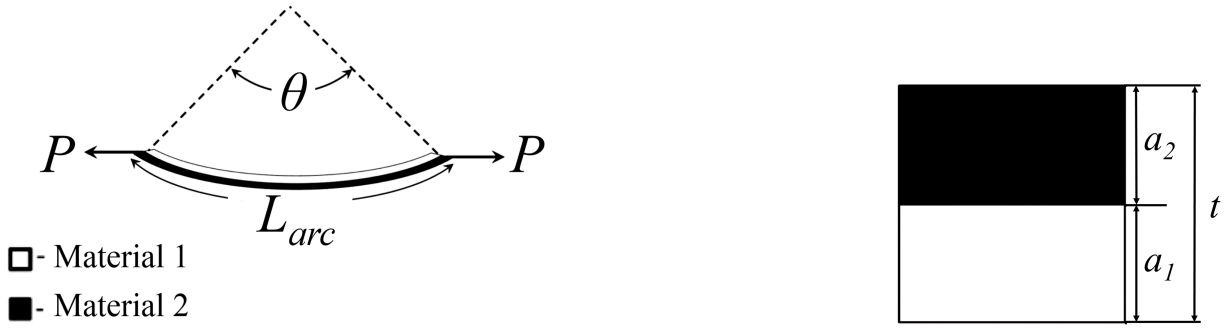

(A) (B)

FIGURE 2.2: (a) The loading state used to determine analytical results of zero coefficient of thermal expansion on the bi-material curved rib for pin-ended joints [85]. (b) L_{arc} is the arc length of the rib, θ is the included angle, and P represents axially applied load. The cross-sectional area of the bi-material curved rib [85] is shown.

TABLE 2.1: Material properties of selected materials.

	Material 1 (invar)	**Material 2 (steel)**
Elastic modulus, E	140 GPa	200 GPa
CTE, α	1 μstrain/K	12 μstrain/K
Poisson's ratio, ν_{LT}	0.28	0.3

The analysis of such a lattice [85] relies on pin-ended joints between the bi-material curved ribs. These joints allow a force transmission to adjacent ribs while rotation is unconstrained; the ends of adjoining ribs are free to rotate with respect to one another. For these reasons, the curvature, and hence the moment, throughout a rib is uniform, with the result that it was straightforward to obtain the analytic solution given in Equation 2.1. For other engineering reasons such as limitations during the manufacturing process, bonded (or welded) joints between these ribs may be desirable or may be necessary. For example, we are currently investigating the use of 3-D printing to fabricate new materials, and this technology will most likely require bonded joints. With bonded joints, the curvature and moment will not be uniform and the resulting differential equations will be difficult or impossible to solve in closed form. Hence, the use of finite element analysis is effective.

In the present manuscript, an individual bi-material curved rib connected by pin-ended joints was modeled using the commercial finite element program ANSYS APDL to verify the analytical results of reference [85]. A finite element model of the bi-material curved rib with bonded joints was then created and studied to determine if it could achieve zero or reduced thermal expansion. For both ribs, the effective coefficients of thermal expansion were calculated. The effects of rib curvature and of rib slenderness for both joints were also investigated. To incorporate the effects of interactions between adjacent ribs in a lattice, several finite element models of a thermoelastic triangular lattice were created by assembling the finite element models representing each of individual bi-material curved ribs. The influence of bonded joints between such ribs in the lattice was then investigated subject to uniform temperature change. The effective thermal expansion coefficient of the lattice was also computed. A change in the orientation of some of the ribs in the lattice was studied to observe how such a change would influence the overall thermal expansion. Finally, we conclude this paper with discussion of a square lattice with bonded joints that has zero net thermal expansion provided that each rib has zero thermal expansion.

2.2 An individual bi-material curved rib

2.2.1 Determination of optimized geometric parameters

In order to achieve zero thermal expansion coefficient of an individual bi-material curved rib, geometric parameters and material properties need to be specified carefully [85]. With Equation 2.1 describing the net thermal expansion coefficient of the rib in terms of geometric parameters and elastic moduli of the two materials, the included angle to obtain a zero net thermal expansion coefficient can be numerically computed by varying the invar fraction, as illustrated in Figure 2.3. Invar fraction is the ratio of the thickness of invar to the total thickness of the rib, and the rib aspect ratio, AR, is the ratio of the arc length to the total thickness of the rib. Each curve denotes a different aspect ratio for representing slenderness of the rib. Materials used in this graph are typical invar and steel. The prior analytical results described an optimum invar fraction as approximately 45 % [85]. The input to FEM requires a more precise value than is needed to draw graphs for an analytical result. This value was extracted from Equation 2.1 to show that the optimum fraction was actually 46.39 % regardless of the rib aspect ratio. This parameter was confirmed by obtaining desired thermal expansion of a rib with pin-ended joints by finite element analyses.

The optimum invar fraction of 46.39 % was then substituted into Equation 2.1 to obtain optimized geometric parameters of an individual bi-material curved rib. With the total thickness of the rib of 1 mm and the rib aspect ratio of 10, the included angle was calculated as 0.4909 radians, the radius of curvature was found to be 20.3684 mm, and the thickness of materials one and two was computed as 0.4639 mm and 0.5361 mm, respectively. These optimized values are summarized in Table 2.2.

TABLE 2.2: Optimized geometric parameters of an individual bi-material curved rib.

Optimized geometric parameters	**Values**
The thickness of the material 1, a_1	0.4639 [mm]
The thickness of the material 2, a_2	0.5361 [mm]
The included angle, θ	0.4909 [radians]
The radius of curvature, ρ	20.3684 [mm]

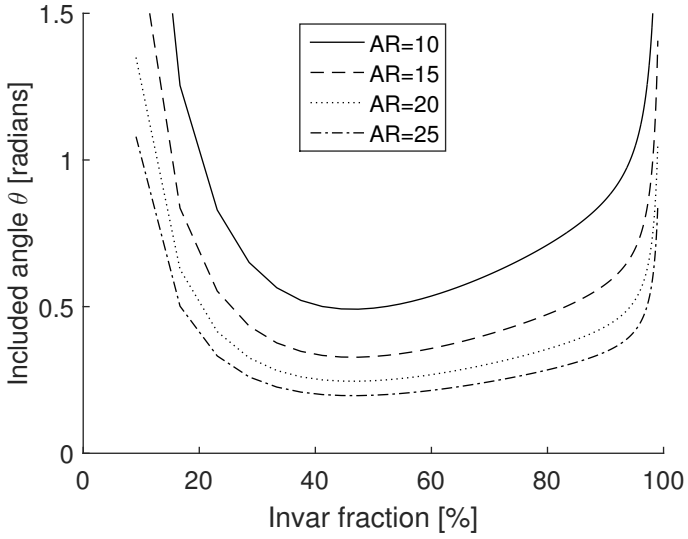

FIGURE 2.3: The included angle of the bi-material curved rib versus the invar fraction with various aspect ratios to achieve zero thermal expansion coefficient. For all aspect ratios, the minimum included angle θ, which corresponds to the rib with the least curved geometry, occurs for the invar fraction of approximately 46.39 %.

2.2.2 Design of an individual bi-material curved rib

Baseline finite element model

A baseline finite element model of an individual bi-material curved rib, as depicted in Figure 2.4a, was created by using the optimized geometric parameters given in Table 2.2. This model allows simulation of both the pin-ended and the bonded joints by imposing two different sets of support conditions. For design of the baseline model, PLANE 183 elements were used in ANSYS with linear elastic isotropic plane stress behavior. The width in the direction perpendicular to xy-plane was 1 mm. This element is a higher order two-dimensional 8-node element, and has a quadratic displacement behavior and two degrees of freedom (d.o.f.) at each node: nodal translation in the x and y directions. Material one positioned on the inner portion of the rib was invar, while material two on the outer portion was steel. The material properties given in Table 2.1 for invar and steel were used for this model.

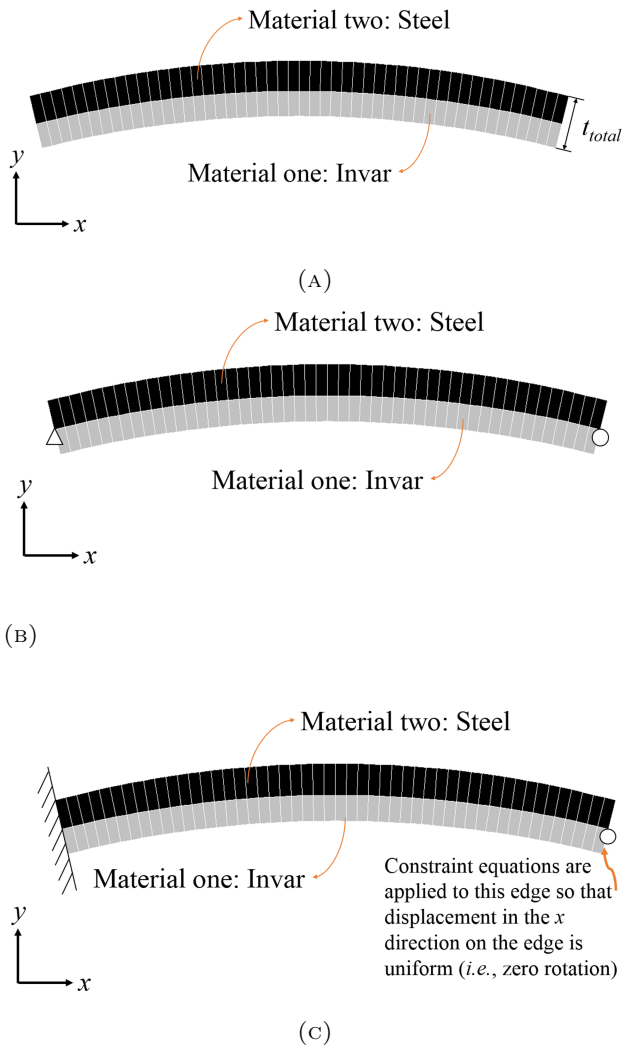

FIGURE 2.4: (a) A two-dimensional baseline finite element model of an individual bi-material curved rib. PLANE 183 elements in ANSYS were used with plane stress behavior. Geometric parameters listed in Table 2.2 were applied to this model. The width was set to 1 mm in the direction perpendicular to xy-plane. All nodes and elements lie in the plane of the figure. (b) A two-dimensional finite element model describing a simply supported bi-material curved rib. (c) A two-dimensional finite element model describing an individual bi-material curved rib with bonded joints.

In general, an increase in the number of finite elements in a model produces greater accuracy of the results at the expense of greater computation time. A convergence analysis was performed to determine a suitable number of elements in order to have acceptable accuracy. The model meshed

with 100 elements per rib was considered as reference. It was found that at least 80 elements per rib were required to obtain displacement error less than 1 %. For this reason, unless specified otherwise throughout this paper, all of the finite element models are meshed using a total of 100 elements per rib.

Finite element model of an individual bi-material curved rib with pin-ended joints

The finite element model shown in Figure 2.4b was created so that it could reproduce the same support conditions that were employed in the analytical study [85]. Namely, this model is simply supported with a pin at the left and a roller at the right that constrains the vertical motion at the right tip. Hence, this model is appropriate to verify the prior study of a zero net thermal expansion of an individual bi-material curved rib with pin connections at ends [85]. Since the support conditions do not constrain rotation at either end, both ends are allowed to rotate freely, and the right end is free to displace horizontally due to either an axial load at the right tip or a temperature change. Note that the supports (i.e., locations of the pin and the roller) are positioned at the interface between materials.

Finite element model of an individual bi-material curved rib with bonded joints

A finite element model representing an individual bi-material curved rib with bonded joints on both ends was developed, as shown in Figure 2.4c. This model is built-in at the left and is supported with a roller at the right tip with constraint equations that prevent rotation of the right end while allowing a uniform translation of the right end in the x direction (i.e., nodal displacements of the right end in the x direction are uniform). Hence, these support conditions represent bonded joints at both ends of the curved rib. Note that the roller support is located at the interface between materials on the right edge.

2.2.3 Results and discussion

Thermal expansion of an individual bi-material curved rib with bonded joints

Uniform temperature changes, ΔT, of 1K, 10K, 20K, 50K, and 100K were applied to both finite element models with pin-ended and bonded joints. Since our models are linear elastic, only one temperature change would be adequate to characterize the thermal expansion behavior, but we believe the usefulness of the results is enhanced by considering multiple temperature changes. Note that the finite element model with the pin-ended joints was used to numerically study the validity and/or limitations of the analytical results [85] regarding parameters that allow design of a rib with a zero net thermal expansion. Thus, this model was expected to have zero thermal expansion. For useful comparisons, additional finite element models for a homogeneous curved rib made entirely of invar or entirely of steel were also modeled, and the corresponding thermal expansions were computed numerically for both the pin-ended and the bonded joints.

Figure 2.5 demonstrates numerically obtained horizontal tip displacements for both homogeneous and bi-material curved ribs as a function of uniform temperature change. In this graph, solid data points represent the ribs with the bonded joints, while the ribs that are pin connected are illustrated as hollow data points. As expected, for homogeneous ribs, there was very small difference in horizontal tip displacements regardless of the joint conditions; these ribs produced uniform thermal expansion which resulted in no cross section rotation of the ends, and the coefficients of thermal expansion were about 1 μstrain/K for a rib made of invar and about 12 μstrain/K for a rib made of steel. This is consistent with the notion that constraint of rotation should not be influenced by uniform deformation.

A bi-material curved rib with pin-ended joints produced nearly zero horizontal tip displacements. The corresponding coefficient of thermal expansion was found to be 0.1884 μstrain/K. Therefore it can be concluded that there is good agreement between the finite element model and the analytical results [85]. On the other hand, a bi-material curved rib with bonded joints showed a substantial increase in the horizontal tip displacement, and the thermal expansion coefficient of this rib was

computed to be 8.0157 μstrain/K. This rib experienced a horizontal tip displacement that is 42.5 times larger than that for the pin-ended joints subjected to the same temperature change, but still exhibited approximately 33 % less expansion than that of a homogeneous rib made of steel.

The constraint of rotation reduces the bending effect that would otherwise enable the bi-material curved rib to achieve zero expansion. As a result, it appears that the optimized geometric parameters to obtain zero thermal expansion according to the analytical results [85] need to be revised for a rib with bonded joints.

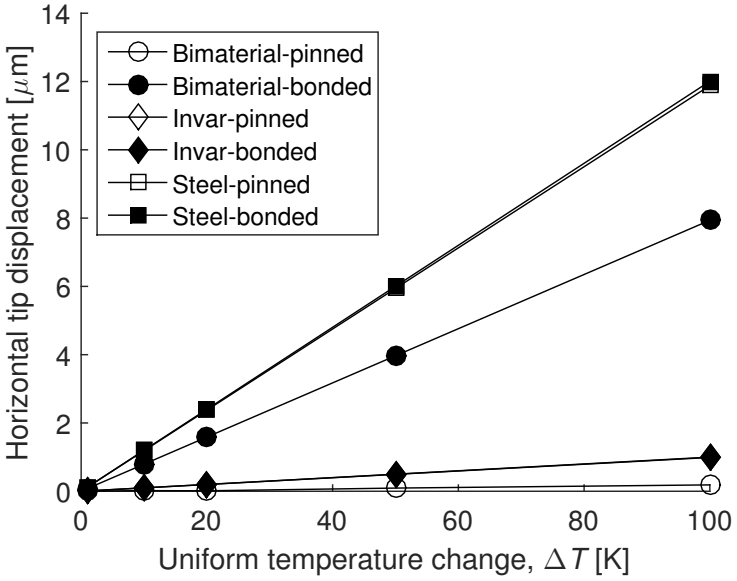

FIGURE 2.5: The horizontal tip displacement of homogeneous and bi-material curved ribs versus uniform temperature change, ΔT.

The effects of rib curvature

A further investigation on a bi-material curved rib with bonded joints was performed to determine whether careful tuning of the geometric parameters could result in zero net thermal expansion. Four rib curvatures were generated by varying the radius of curvature, ρ, and the included angle, θ, simultaneously while holding a constant distance between the ends of the rib constant, as shown

in Figure 2.6. The thick solid curve shown represents the rib curvature obtained using the optimized geometric parameters (ρ_{opt} and θ_{opt}) given in Table 2.2. Geometric parameters for other rib curvatures are given in Table 2.3.

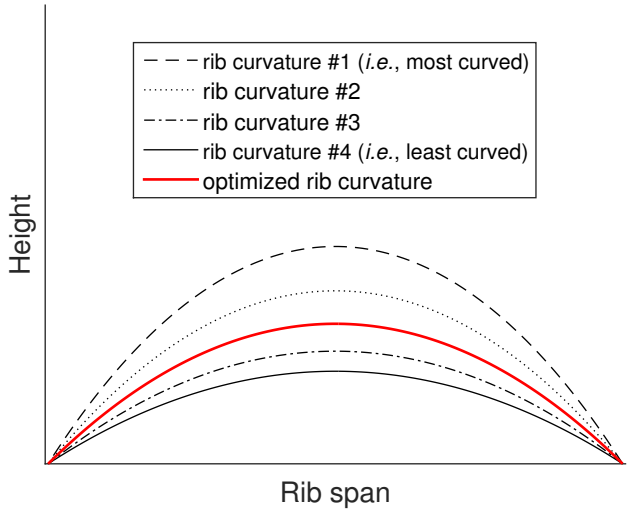

FIGURE 2.6: Several rib curvatures, shown to scale, for the bi-material curved rib. Each curve was generated by varying the optimized geometric parameters while holding a constant distance between the ends of the rib constant. The thick solid curve shown represents the optimized curvature of the bi-material curved rib [85].

TABLE 2.3: Geometric parameters for several rib curvatures. The radius of rib curvature and the included angle were varied simultaneously while holding a constant distance between the ends of the rib constant.

	ρ/ρ_{opt}	θ/θ_{opt}
Rib curvature #1	0.685	1.541
Rib curvature #2	0.816	1.232
Rib curvature #3	1.237	0.806
Rib curvature #4	1.5	0.663

The baseline finite element model of the bi-material curved rib was modified in order to develop finite element models of the bi-material curved rib having rib curvatures shown in Figure 2.6. Similar to the analysis in the previous section, horizontal tip displacements of these models due to uniform temperature changes were computed numerically and are illustrated in Figure 2.7. In addition to

the ribs with bonded joints, pin-ended ribs associated with each rib curvature shown in Figure 2.6 were also studied to observe how they would result in thermal expansion depending on varying the rib curvature under uniform temperature change. As before, hollow data points illustrate the ribs with pin-ended joints, while solid data points represent the ribs with bonded joints.

As depicted in Figure 2.7, the horizontal tip displacements of the bi-material curved ribs with pin-ended joints decrease as the rib becomes more curved (i.e., increasing rib curvature). If the rib is more curved than one designed based on optimal parameters leading to zero thermal expansion, material two with a higher coefficient of thermal expansion (i.e., the outer portion of the rib) dominates deformation, which leads to negative thermal expansion. On the other hand, material one with a lower coefficient of thermal expansion plays a substantial role resulting in positive thermal expansion when the rib is less curved. This indicates that such ribs allow one to produce either positive or negative thermal expansion by varying rib curvature (i.e., changing ρ and θ simultaneously) while holding other geometric parameters constant.

In contrast, for the ribs with bonded joints, the horizontal tip displacements were not altered significantly regardless of how much these ribs were curved. The thermal expansion coefficients for these ribs were found to be approximately 8 μstrain/K. A study of the effect of rib curvature was done by holding a constant distance between the ends of the rib while varying the radius of curvature, ρ, the included angle, θ, and the arc length, L_{arc}. For the ribs with bonded joints, the bending moment that is produced varies depending on the rib curvature. As the rib curvature increases, the arc length extends, which minimizes the effect of the bending moment. This results in the minimal influence on thermal expansion.

Consequently, it would be desirable to have an analytical solution for a rib with bonded joints. This would help to explore the design space to determine if and how zero thermal expansion could be obtained. However, even with such a solution, it would not provide the same results as for a rib with bonded connections that is part of a lattice, because of the effects of rotation of the ends.

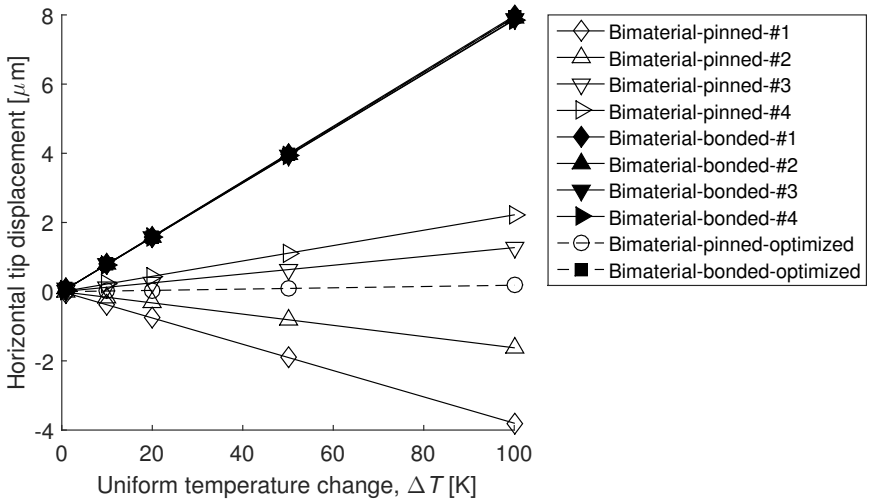

FIGURE 2.7: The horizontal tip displacement versus uniform temperature change. Each line represents the horizontal tip displacement of the bi-material curved ribs for several rib curvatures described in Figure 2.6 with either pin-ended or bonded joints. While the ribs with the pin-ended joints can produce either positive or negative thermal expansion by controlling geometric parameters, such thermal expansions are not possible with the ribs with the bonded joints.

The effects of rib aspect ratio

If ribs are straight and slender, it is known that a lattice with bonded joints behaves similarly to a lattice with pin joints. A difference is observed in the present lattice which has curved ribs. The reason is that curved ribs when deformed tend to rotate at the end. A bending moment is generated at a bonded joint but not at a pin joint. If ribs are straight there is neither a tendency to rotate nor a bending moment.

A brief study of the effects of aspect ratio, AR, was carried out. As defined earlier, the aspect ratio is the ratio of the rib's arc length to its total thickness; increasing AR corresponds to an increasingly slender rib. Although we do not present detailed results here, we found that under uniform temperature change, regardless of aspect ratio, a rib with pin-ended joint achieves nearly zero thermal expansion, and thermal expansion of a rib with bonded joints is unchanged. Thus, the role of bending moments in ribs with the bonded joints continues importantly even for slender ribs.

2.3 Thermoelastic triangular lattices composed of bi-material curved ribs

In Section 2.2 of this paper, finite element models were developed to represent individual bi-material curved ribs with pin-ended and bonded joints. Although these finite element models have provided insightful results, they do not necessarily characterize the thermal expansion behavior of a lattice that is composed of these ribs. Thus, it is necessary to develop finite element models of possible lattice structures, and several of these are considered in this section and the next.

2.3.1 Design of a thermoelastic triangular bi-material lattice

A finite element model of a thermoelastic triangular bi-material lattice

A finite element model of a two-dimensional equilateral triangular lattice composed of bi-material curved ribs was created by assembling the finite element model of an individual bi-material curved rib, as shown in Figure 2.8a. The elastic moduli and thermal expansion coefficients for invar and steel described in Table 2.1 were applied to the model. Thus, this model is adequate to represent the lattice proposed by reference [85]. Node numbers at the locations of joints are shown in this figure. This model is supported by a pin at node 1 (i.e., the left-bottom node) and rollers at nodes 2, 3, 4, and 5 (i.e., the remaining bottom nodes). Additionally, in order to reproduce bonded joints between the ribs in the lattice, a rotational degree of freedom (i.e., rotation about the z direction) on edges at both ends of the ribs needs to be constrained in such a way that adjacent edges of adjoining ribs have the same rotational displacement. To do so, each of these edges was meshed with two BEAM 189 elements in ANSYS APDL, as shown in Figures 2.9a and 2.9b. This element is a three-dimensional quadratic three-node beam element having six degrees of freedom at each node; three translations in the x, y, and z directions and rotations about the x, y, and z directions. To render these beam elements as two-dimensional, the superfluous degrees of freedom for all nodes of the beam elements were constrained to have zero values (i.e., for each node of the beam elements, translation in the z direction and rotations about the x and y axes were given zero prescribed

values). Moreover, a stiffer elastic modulus (100 times stiffer than steel) and the same rectangular cross sectional area were applied to the beam elements compared to that of the baseline model of an individual bi-material curved rib, for representing a realistic bonded joint in practice. A thermal expansion coefficient of these beam elements used at the ends was also set to zero.

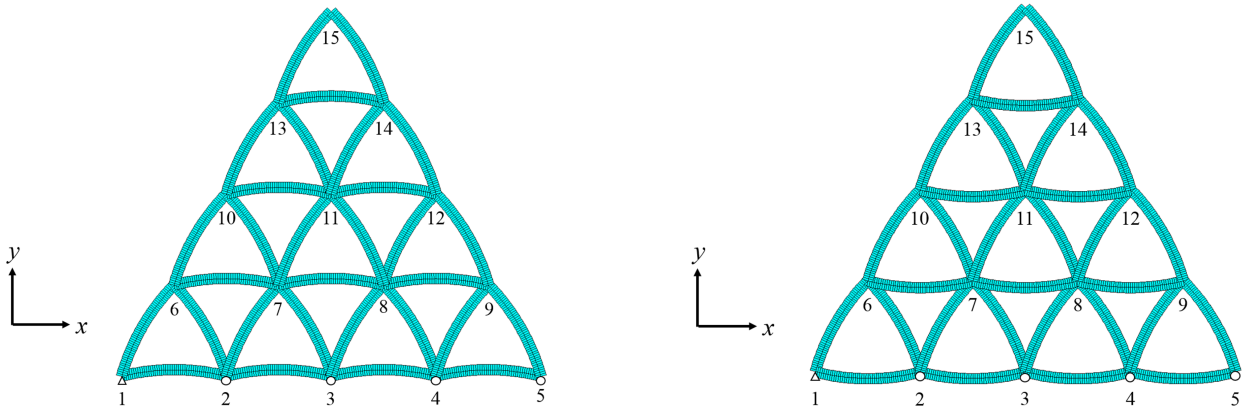

FIGURE 2.8: (a) A two-dimensional equilateral triangular lattice composed of bi-material curved ribs. Node numbers at the locations of joints are shown. (b) A two-dimensional equilateral triangular lattice composed bi-material curved ribs with reversed rib curvatures. This model is identical to that described in Figure 2.8a except the bottom ribs of each cell have been reversed.

A finite element model of a thermoelastic triangular bi-material lattice with reversed rib curvatures

Figure 2.8b shows a finite element model representing a two-dimensional equilateral triangular lattice where the bottom ribs of each cell in the lattice are reversed compared to Figure 2.8a. Material properties, element types used for modeling, nodal locations, and support conditions are identical to the finite element model of the lattice described in the previous section.

2.3.2 Results and discussion

Thermal expansion of a thermoelastic triangular bi-material lattice

Uniform temperature changes, ΔT, of 1K, 10K, 20K, 50K, and 100K were considered. Figure 2.10

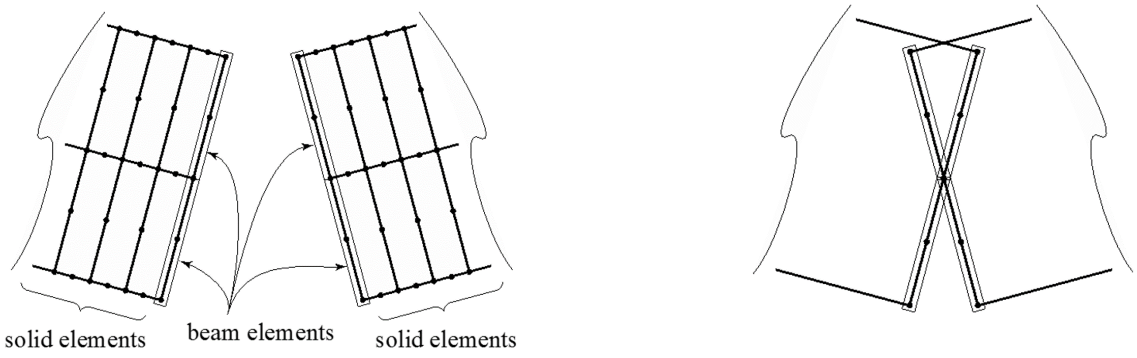

(A) (B)

FIGURE 2.9: A representation of bonded joints in the lattice model using four 3-node beam elements (BEAM 183) on the ends of ribs. Two ribs are shown separated for clarity. (a) The rib has two stiff beam elements, and similarly for the rib on the right. (b) The nodes and element edges for the solid elements are not shown for clarity. The beam elements share a common node, and due to their high stiffness, they are essentially rigid and effectively model a bonded connection between the two ribs.

illustrates overall thermal expansions in the x and y directions of a thermoelastic triangular bi-material lattice with two different joint conditions (i.e., pin-ended and bonded joints), respectively. Solid data points represent the lattices with the bonded joints while the pin-ended lattices are given as hollow data points. Such displacements of homogeneous lattices made entirely of invar or entirely of steel were also plotted in these figures for useful comparisons. The results showed that the overall thermal expansion displacements of the bi-material lattice with the bonded joints were significantly larger in both x and y directions than those with the pin-ended joints; the corresponding effective coefficients of thermal expansion were calculated to be approximately 6.6707 μstrain/K for the bonded lattice and -0.0326 μstrain/K for the pin-ended lattice.

As a result, a pin-ended bi-material lattice allows tuning of thermal expansion coefficient to approach zero, while a similar lattice with bonded joints exhibits substantial thermal expansion. Moreover, it is worthwhile noting that the pin-ended bi-material lattice produces very small negative coefficient of thermal expansion rather than small positive value that has been observed in a study of an individual bi-material curved rib with pin-ended joints. Thus, an analytical solution for a lattice

with bonded joints would be desirable, which would help to study the design space to determine whether zero thermal expansion could be obtained.

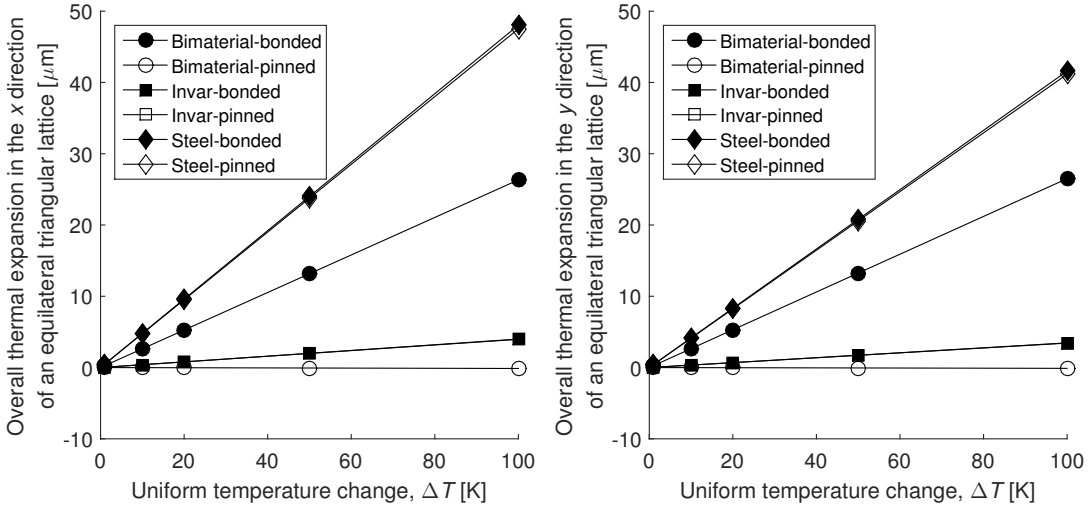

FIGURE 2.10: Overall thermal expansions in the x and y direction of a thermoelastic triangular lattice composed of bi-material curved ribs with two different joint conditions.

Thermal expansion of a thermoelastic triangular bi-material lattice with reversed rib curvatures

Figure 2.11 illustrates overall thermal expansions in the x and y directions of a thermoelastic triangular bi-material lattice having reversed curvature bottom ribs of each cell (shown in Figure 2.8b) with both pin-ended and bonded joints due to uniform temperature changes. A change in the orientation of the rib curvature from concave-down to concave-up had negligible effect on the overall thermal expansion in a pin-ended lattice regardless of its material constitution. On the other hand, such change resulted in an overall thermal expansion of a lattice with bonded joints that is larger in the x direction by a factor of 1.20 and in the y direction by a factor of 1.03, when compared to a similar lattice with no reversed rib curvatures. Therefore, it appears that thermal expansion of a bi-material lattice with bonded joints is sensitive to the shape of each cell.

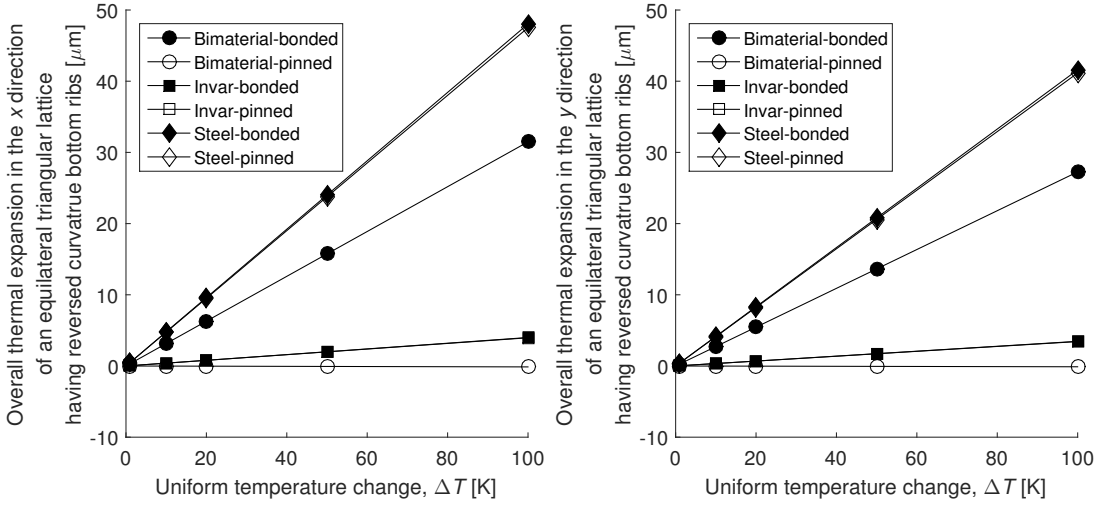

FIGURE 2.11: Overall thermal expansions in the x and y direction of a thermoelastic triangular lattice having reversed curvature bottom ribs of each cell composed of bi-material curved ribs with two different joint conditions.

2.4 A square lattice composed of bi-material curved ribs

Zero thermal expansion in lattices with bonded joints is possible if ribs are orientated with cubic symmetry, as shown in Figure 2.12. This lattice is stiff in the principal directions but not in oblique directions. Due to a uniform temperature change, each rib produce the same displacement and rotation. However, the joint rotation of each rib is accommodated by equal rotation of adjoining ribs, hence there is zero moment in each rib at each joint, even though joints are bonded. This leads to zero net thermal expansion provided that each rib individually has zero net thermal expansion and provided the temperature change is uniform. Due to a temperature gradient, this lattice will likely have thermal expansion, although perhaps this will be small. Further finite element studies are needed to elucidate this behavior.

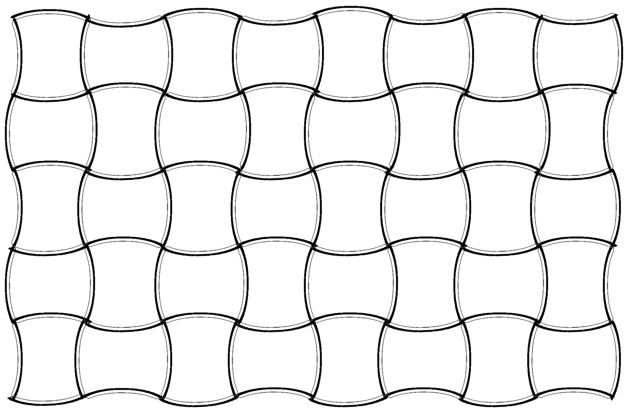

FIGURE 2.12: A square lattice composed of bi-material curved ribs with bonded joints. This lattice will display zero thermal expansion provided each rib has zero thermal expansion and the temperature change is uniform.

2.5 Conclusions

This manuscript shows that an individual bi-material curved rib with pin-ended joints can exhibit desired thermal expansion, as expected. On the other hand, a rib with bonded joints produced substantial positive thermal expansion. The effects of rib curvature variation were negligible on thermal expansion of a rib with bonded joints, while a rib with pin-ended joints depended highly on it. The effective coefficient of thermal expansion of a rib with both pin-ended and bonded joints stays the same regardless of different slenderness. The role of bending moments in curved ribs bonded at the joints persists even for slender ribs. Similar results were observed for equilateral triangular lattices with these two different joint conditions. A change in the orientation of some of the ribs in a lattice had a negligible thermal expansion change in pin-ended lattices regardless of its material constitution. However, for lattices with bonded joints, the shape of cells in the lattice strongly influence the overall thermal expansion. A square lattice composed of bi-material curved ribs with bonded joints can provide zero expansion.

Acknowledgements The work presented in this paper was supported by the Defense Advanced Research Projects Agency-Lawrence Livermore National Laboratory (DARPA-LLNL) via

grant B593206.

Chapter 3

Controllable thermal expansion of large magnitude in chiral negative Poisson's ratio lattices

The following chapter has been published:
C. Ha, E. Hestekin, J. Li, M. E. Plesha, and R. S. Lakes, "Controllable thermal expansion of large magnitude in chiral negative Poisson's ratio lattice", Physica Status Solidi (b), 252 (7), 1431-1434 (2015).

Abstract Lattices of controlled thermal expansion are presented based on planar chiral lattice structure with Poisson's ratio approaching -1. Thermal expansion values can be arbitrarily large positive or negative. A lattice was fabricated from bimetallic strips and the properties analyzed and studied experimentally. The effective thermal expansion coefficient of the lattice is about $\alpha = -3.5 \times 10^{-4}\mathrm{K}^{-1}$. This is much larger in magnitude than that of constituent metals. Nodes were observed to rotate as temperature was changed corresponding to a Cosserat thermoelastic solid.

3.1 Introduction

Materials with large thermal expansions have many potential applications as thermal actuators. Available materials such as common metals, alloys, and polymers have a limited range of expansion that may not suffice for some applications. Composite materials may be considered, but until recently were not thought to be promising, because thermal expansion of a two phase composite has been constrained by analytical bounds [4]. The expansion of the composite cannot be larger than the maximum expansion of the constituents. These bounds were derived assuming that the two phases are perfectly bonded, also that there is no porosity, and that each phase has a positive definite strain energy. If one relaxes any of these assumptions, one can achieve arbitrarily large or small values of expansion. For example if the composite contains void space, lattices may be envisaged with controllable expansion of large or small magnitude, or even negative expansion [11] [3]. The ribs in the lattice can be made of a sandwich of two materials of different thermal expansion, giving rise to bending [86]. In a related vein, lattices with bi-material piezoelectric elements have been developed and analyzed [14] and studied experimentally [15]; these lattices give rise to large values of piezoelectric sensitivity.

The concept used in the present research is based on a planar chiral lattice with Poisson's ratio -1 [34]. The Poisson's ratio was determined experimentally and analytically. Experiments revealed that the Poisson's ratio is approximately constant for axial compressive strains up to 25%. This is in contrast to the nonlinearity observed in the Poisson's ratio of negative Poisson's ratio foams [42] and of honeycombs [87] with inverted hexagonal cells of bow-tie shape. Negative Poisson's ratio materials are commonly referred to as "auxetic". Chiral lattices have been analyzed [33] in the context of Cosserat (micropolar) elasticity [23] in which rotation of points has physical significance. Analysis shows this lattice has the largest Cosserat characteristic length scale of all known lattice topologies [88].

Chiral lattices have been considered for use as chiral honeycomb [89] [90] in sandwich panels for airplane wings that change shape, and they have been analyzed for buckling [91] and other

characteristics such as stop bands in wave propagation [92]; they have also been fitted with sensors and actuators for possible use as smart structures [93].

3.2 Procedure

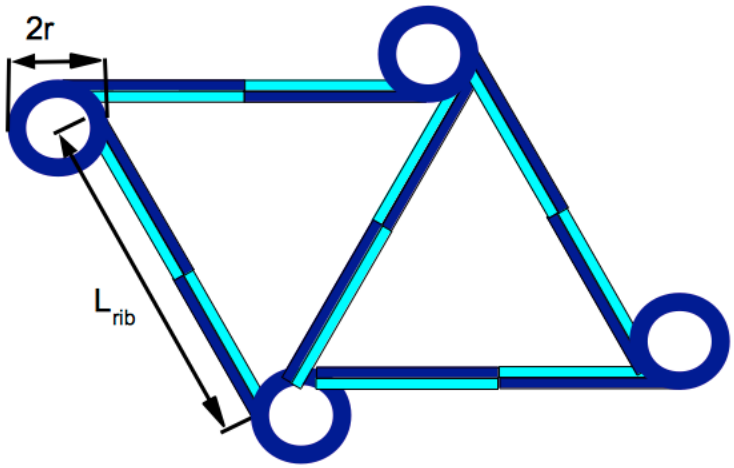

FIGURE 3.1: Chiral lattice structure with bi-material ribs with alternating orientation. Two materials indicated as light and dark, differ in their thermal expansion.

The lattice structure is chiral in plane and gives rise to a Poisson's ratio approaching -1. To achieve control of the thermal expansion, the lattice structure makes use of bi-material rib elements as shown in Figure 3.1. These ribs bend upon a temperature change, giving rise to node rotation and to strain of the lattice.

As for materials, the most active bimetallic strip material available was used: Engineered Materials Solutions "P675R" strip [94]. Its high expansion alloy is 52.8% by weight and is composed of 72% manganese, 18% copper, and 10% nickel. Its low expansion alloy is 36% nickel and 64% iron [94]. The thermal expansion coefficient for constituent metals is from about 10×10^{-6} K^{-1} (for iron) to 22×10^{-6} K^{-1} (for manganese). The low expansion alloy appears to be Invar, with $\alpha = 1.3 \times 10^{-6}$ K^{-1} and the high expansion alloy [95], $\alpha = 27.2 \times 10^{-6}$ K^{-1}.

The strips were first cut from a large roll of bimetallic sheet. The strips were cut to a length of $L_{rib} = 75$ mm, and a width of 10 ± 0.2 mm. The thickness of the strips is $h = 0.25 \pm 0.05$ mm. The high and low expansion sides were determined by heating a strip on a hot plate and observing the curvature. The circular nodes used for the chiral cells were cut from a chlorinated PVC plastic pipe with outer diameter $d = 16$ mm and wall thickness 2 mm. In an initial trial, a lattice was made by bonding constituents with conventional cyanoacrylate cement, but the glue joints did not survive repeated excursions to 70°C. Constituents were bonded with Loctite type 491 cement, intended for use at elevated temperature up to 400°C. The lattice cells were constructed following the design in Figure 3.1 except that some overlap of rib segments was provided to facilitate bonding, rather than cementing end to end. The same type 491 cement was used to make the mid-rib joints. The lattice consisted of six triangular cells arranged in a hexagonal pattern.

Temperature control was achieved using a Fisher model 126 muffle furnace. The lattice was placed in the furnace behind a calibrated length scale. Digital photographs were taken from the same height and angle for all measurements. Isolation from ambient temperature was achieved by taping a transparent plastic film over the furnace. A thermocouple lead was placed in the middle of the lattice for temperature measurements. Output indicated that the plastic film was a sufficient insulator from ambient temperature outside the furnace. With this configuration, digital photographs of the lattice in room temperature air were taken (25°C), followed by photographs at temperatures up to 120°C. Specifically the lattice was photographed in the furnace at ambient temperature, then the temperature was progressively increased. Further digital photographs of the lattice were taken at elevated temperature, then more photographs were taken during slow cooling. Some further experiments were conducted below ambient temperature by using the uniform low temperature outdoors in winter. Dimensions of the lattice in the vertical and horizontal directions were measured from the digital images using Photoshop software. The scale in the digital images was about 150 pixels/cm.

3.3 Analysis

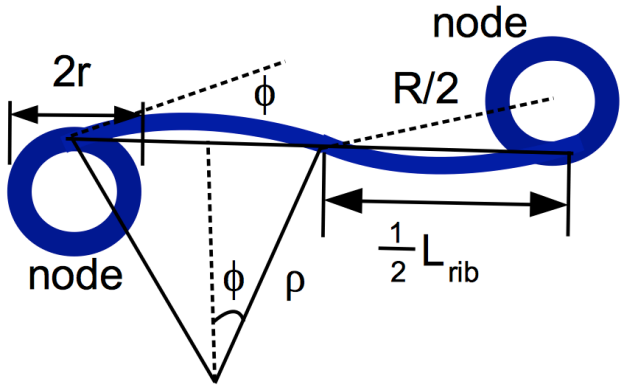

FIGURE 3.2: Bending of a rib in a chiral lattice structure.

Ribs are assumed to be sufficiently slender that deformation from axial strain is negligible in comparison with deformation due to bending of the ribs. Nodes are assumed to be rigid. Also, thermal expansion is assumed to occur freely without constraint. In the chiral lattice, strain is geometrically linked to rotation ϕ, node outer radius r and the spacing R of nodes between centers [34]:

$$\epsilon = \frac{r\phi}{R} \tag{3.1}$$

A temperature change causes bending of the bi-material rib segments which produces curvature with radius ρ in which the included angle is 2ϕ as shown in Figure 3.2. So

$$\phi = \frac{L_{rib}}{4\rho} \tag{3.2}$$

where the rib length L_{rib} is such that, from the diagram,

$$R = \sqrt{L_{rib}^2 + (2r)^2} \tag{3.3}$$

Each half of the rib has a uniform curvature but in the opposite direction because the bi-material

strips have opposite orientation. Hence, the deformed rib has an S shape. Combining Equations 3.1 - 3.3 yields

$$\epsilon = \frac{r}{4\rho}\frac{1}{\sqrt{1+(2r/L_{rib})^2}} \tag{3.4}$$

The thermal expansion α is expressed in terms of specific curvature ${\rho_s}^{-1} = \rho^{-1}/\delta T$ so

$$\alpha = \frac{r}{4\rho_s}\frac{1}{\sqrt{1+(2r/L_{rib})^2}}. \tag{3.5}$$

But the curvature is provided by the manufacturer [94] as a specific curvature parameter κ = 37 - 41 $\times 10^{-6}\frac{mm}{mm}{}^{\circ}\mathrm{C}^{-1}$ that incorporates the change of curvature with temperature change; in the following a value of 40 is used. ${\rho_s}^{-1} = \frac{\kappa}{h}$, so with $h = 0.25$ mm, substituting the dimensions and specification of κ in Equation 3.5, the lattice has expansion of magnitude $\alpha = 320 \times 10^{-6}$ K^{-1}. The analysis does not provide the sign because orientation was not considered.

If one is provided with the elastic modulus and thermal expansion of each constituent, E_1 and α_1 for phase 1 and E_2 and α_2 for phase 2 respectively, and with the corresponding thickness a_1 and a_2 of each layer in the bi-material strip, then the curvature is [86],

$$\rho^{-1} = \frac{(\alpha_2-\alpha_1)\delta T}{\frac{h}{2}+\frac{2(E_1I_1+E_2I_2)}{h}[\frac{1}{E_1a_1}+\frac{1}{E_2a_2}]} \tag{3.6}$$

in which δT is temperature change, and $I_1 = \frac{a_1^3}{12}$ and $I_2 = \frac{a_2^3}{12}$ are the section moments of inertia of the layers. The total thickness is $h = a_1 + a_2$.

This lattice structure allows one to design the thermal expansion. Larger nodes give rise to a larger magnitude of thermal expansion. The sign of the expansion depends on the orientation of the bimetallic rib elements. Also, the specific curvature, hence the thermal expansion, will increase as the ribs become more slender (smaller h).

3.4 Results and discussion

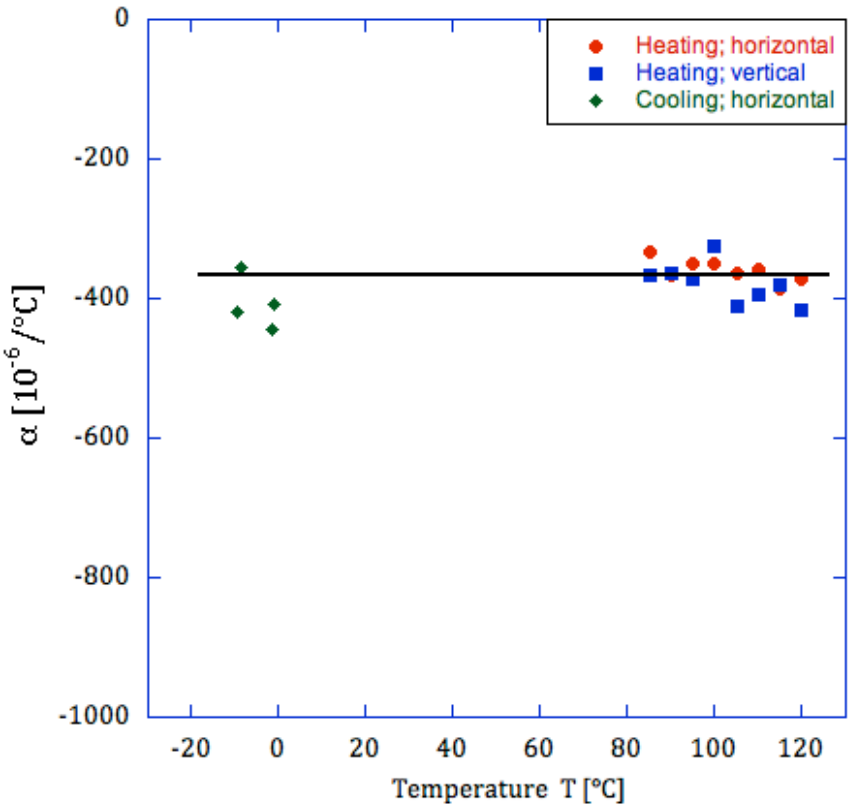

FIGURE 3.3: Experimentally determined thermal expansion coefficient α of the lattice vs. temperature. The lattice has no thermal strain at the reference temperature of 25°C

Experimentally determined thermal expansion vs. temperature is shown in Figure 3.3. The thermal expansion is negative, there is no systematic difference between expansion in the vertical and horizontal directions, and there is no systematic difference between heating and cooling. Measurements at small temperature deviations were limited by image resolution and are not shown. The straight line is a guide for the eye. Negative thermal expansion is uncommon in homogeneous materials; it entails contraction with increasing temperature and expansion with decreasing temperature. The lattice underwent substantial deformation at elevated temperature, sufficient to observe rib curvature, as shown in Figure 3.4. The maximum global strain, however, did not exceed 0.05.

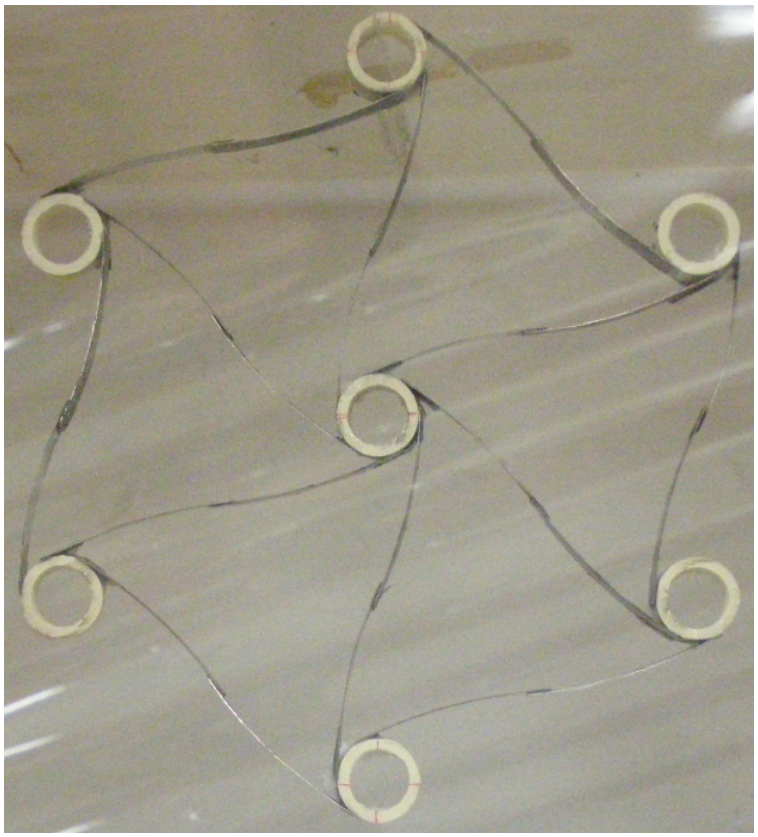

FIGURE 3.4: Deformation of lattice at 115°C in which ribs were initially straight at ambient temperature of 25°C. Horizontal and vertical refer to directions in which lattice expansion was measured.

The determination of thermal expansion α obtained via analysis and experiment are in reasonable agreement, in view of limits associated with resolution and the range of quoted specific curvature values. Also, the overlap of rib segments was not incorporated in the analysis. Too, the expansion of the polymer nodes is on the order 10^{-4} K^{-1} but the node diameter is only 1/5 the rib length. This contributes a reduction of about 5% in the total negative expansion of the lattice. The magnitude of α for the lattice is more than 30 times larger in magnitude than the α value for iron. Higher values could be obtained by using larger nodes, more slender ribs, or both. Positive thermal expansion can be achieved by reversing the orientation of the constituents of the rib elements.

Expansion can be made small by reducing the node radius r. Zero expansion is possible if the

positive axial expansion of each rib element (not considered in the present analysis due to its relative smallness) is balanced by negative expansion due to rib bending. If the ribs have layers of equal thickness, their axial expansion could be balanced by contraction due to rib bending if $r < 0.5$ mm. This is comparable to the rib thickness and the thermal expansion is likely to be sensitive to variations in dimensions. So design for zero expansion by this approach would require high precision in the geometrical parameters. Zero expansion is also possible in other lattices [3] [96].

Node rotation for a single node was $\phi = 0.15$ rad for a temperature change of 33°C. Node rotation is consistent with the notion of homogenizing the lattice as a continuum via Cosserat elasticity. Cosserat solids incorporate rotational degrees of freedom in the microstructure in addition to the usual translation. There are additional elastic constants associated with sensitivity to gradients of rotation; in three dimensions there are six elastic constants for an isotropic, non-chiral Cosserat solid; nine constants if it is chiral. Cosserat solids exhibit an internal length scale in contrast to classically elastic solids; characteristic lengths are expressed in terms of ratios of tensorial elastic constants. Cosserat elastic constants were obtained via analysis of chiral lattices [33]. Cosserat elastic constants have been determined experimentally in several non-chiral foam materials from size effect experiments [35] [36]. Specifically, slender rods in torsion or bending are observed to be more rigid than anticipated based on classical elasticity. In these foams, the characteristic length is comparable to the cell size; for these materials, 0.3-3 mm. Rotations have been studied in the context of rotational waves [97] in designed granular materials. In Cosserat solids, concentrations of stress around holes and cracks is ameliorated, so there is a link to the toughness of the material. A continuum view is more appropriate to thermoelastic lattices such as the present ones than for piezoelectric lattices. Temperature changes can be imposed globally as with a homogeneous material; by contrast piezoelectric lattices thus far entail an electrical connectivity between layers that must be provided for the piezoelectric effect to be manifest. Local rotations in isotropic Cosserat elastic materials are driven by gradients in deformation. If the material is chiral, a uniform stretch gives rise, in three dimensions, to a twisting deformation, hence rotations [32]. Stretch-twist coupling of this kind has been analyzed for cholesteric elastomers [98]. In thermo-elastic chiral materials or

lattices such as the present lattice, a uniform temperature change gives rise to local rotations.

The sign of the thermal expansion and the sign of Poisson's ratio are independent. For example, the present lattice with Poisson's ratio -1 can be made with positive thermal expansion by reversing the rib orientation or by using homogeneous ribs. As for the freedom associated with Cosserat elasticity, the characteristic length can be made large or small by choice of the size of the cells in the lattice; small cells are possible via 3-D printing methods.

As for chiral lattices, such structures have been envisaged for chiral honeycomb [90] in sandwich panels for airplane wings that change shape. Chiral honeycombs of various type have also been optimized for buckling strength [99]. Related structures containing rotating hexamers and trimers [100] and stochastic distributions of circular node sizes can have negative Poisson's ratio of large magnitude. Such structures do not have tunable thermal expansion but variants may be envisaged with such a capability. Indeed, bi-material elements in anti-tetrachiral honeycombs [101] have been analyzed via finite elements; negative properties can be obtained. In view of the additional freedom associated with thermal expansion, the present lattices may be considered further in this context or other lattices developed. The large thermal expansion of the lattice in comparison to its constituent metals can be useful in devices where a large response is desired from a small temperature change.

3.5 Conclusion

The effective thermal expansion coefficient of the chiral lattice is about $\alpha = -3.5 \times 10^{-4} \mathrm{K}^{-1}$. This is much larger in absolute magnitude than the value for known homogeneous materials. The thermal expansion can be controlled by varying the geometrical parameters of the lattice.

Acknowledgment

Partial support from the NSF via CMMI-1361832 and from DARPA-LLNL under the aegis of Dr. Judah Goldwasser is gratefully acknowledged.

Chapter 4

Chiral three-dimensional lattices with tunable Poisson's ratio

The following chapter has been published:
C. Ha, M. E. Plesha, and R. S. Lakes, "Chiral three-dimensional lattices with tunable Poisson's ratio", Smart Materials and Structures, 25 (5), 054005 (2016).

Abstract Chiral three-dimensional cubic lattices are developed with rigid cubical nodules and analyzed via finite element analysis. The lattices exhibit geometry dependent Poisson's ratio that can be tuned to negative values. Poisson's ratio tends to zero as the cubes become further apart. The lattices exhibit stretch-twist coupling. Such coupling cannot occur in a classical elastic continuum but it can occur in a chiral Cosserat solid.

4.1 Introduction

Chiral materials and structures lack a center of symmetry; they are not invariant to inversion of coordinates. For example, quartz is chiral at the inter-atomic level; left and right forms exist. Chirality may also be introduced in composites on a micro, milli, or macro scale. For example, a planar chiral lattice with Poisson's ratio -1 [34] was developed to have a constant Poisson's ratio essentially independent of strain. Analysis revealed Poisson's ratio to be -1, equal to the lower limit

for stability in 2D or in 3D. Experiments revealed Poisson's ratio to be approximately constant for axial compressive strains up to 25%. By contrast, negative Poisson's ratio of (3D) foams [42] and of (2D) honeycombs [87] with inverted hexagonal cells of bow-tie shape is dependent on strain. Two dimensional structures containing rotating hexamers and trimers [100] and distributions of node sizes can have negative Poisson's ratio of large magnitude. Negative Poisson's ratio materials have been called "auxetic" or "anti-rubber"; if the Poisson's ratio is independent of strain, they have been called "dilational".

Chiral 2D lattices have been studied for use as structural honeycomb [89] [90] in sandwich panels for airplane wings that morph or change shape. Buckling [91] [99] of such lattices has been studied in such a structural context. Lattices have been made with sensors and actuators for possible use as smart structures [93]. The lattices exhibit interesting characteristics in wave propagation (e.g., tunable band gaps [92]).

Three dimensional lattices offer design freedom in comparison with foams [10]. For example, 3D lattices with ribs organized in a triangulated structure are stiffer than foams made of the same rib material because the ribs deform axially rather than in bending [102]. A negative Poisson's ratio 3D model was developed [103] to better understand the deformation of α-cristobalite [44], a negative Poisson's ratio form of silicon dioxide. A 3D model of cubical nodules linked at their corners was developed [104] to model the nodule-fibril structure and properties of an auxetic microporous polymer [105]. Also, 3D lattices have been made with a negative Poisson's ratio [106]. Such lattices have been made using 3D printing methods.

If a lattice or foam contains a sufficient number of cells, it may be analyzed as a continuum. In most analyses (e.g., [10]), the continuum is a classical one; classical elasticity has no length scale. If the cell size is not negligible compared with length scales associated with the specimen or with strain gradients applied to it, then a more general continuum model may be appropriate. Cosserat (micropolar) elasticity [23] is such a continuum theory in which rotation of points has physical significance. For example, chiral lattices [34] have been analyzed [33] [88] in the context of Cosserat elasticity.

4.2 Analysis

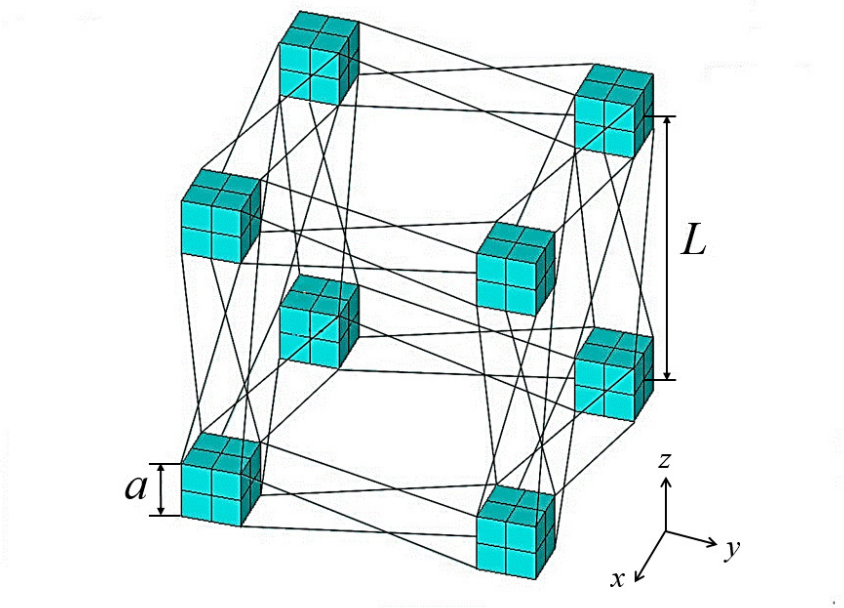

FIGURE 4.1: Unit cell of chiral lattice structure (1×1×1). The aspect ratio is defined to be L/a, where $L/a > 1$.

Lattices were constructed using the unit cell (1×1×1) shown in Figure 4.1. This cell consists of eight rigid cubes at the corners of the cell (with edge lengths a) and multiple deformable ribs (i.e., beams) connecting various corners of cubes to one another as shown. The center-to-center cube spacing is L, and the aspect ratio for the unit cell is defined to be L/a, where $L/a > 1$. The ribs are steel with $E = 200$ GPa and $\nu = 0.3$, and circular cross section with diameter of the ribs is 10 μm. This leads to the ratio of the cube side length to the rib diameter equal to be 100.

A finite element model for the unit cell was constructed using ANSYS. Each rib was modeled using one BEAM 189 element. This beam element has three nodes with six degrees of freedom at each node (three translations and three rotations); has cubic displacement interpolations; and allows for modeling bending behavior and torsion in three dimensions. Because each rib is loaded only by forces and moments at its ends, only one BEAM 189 is needed to obtain exact (or nearly exact)

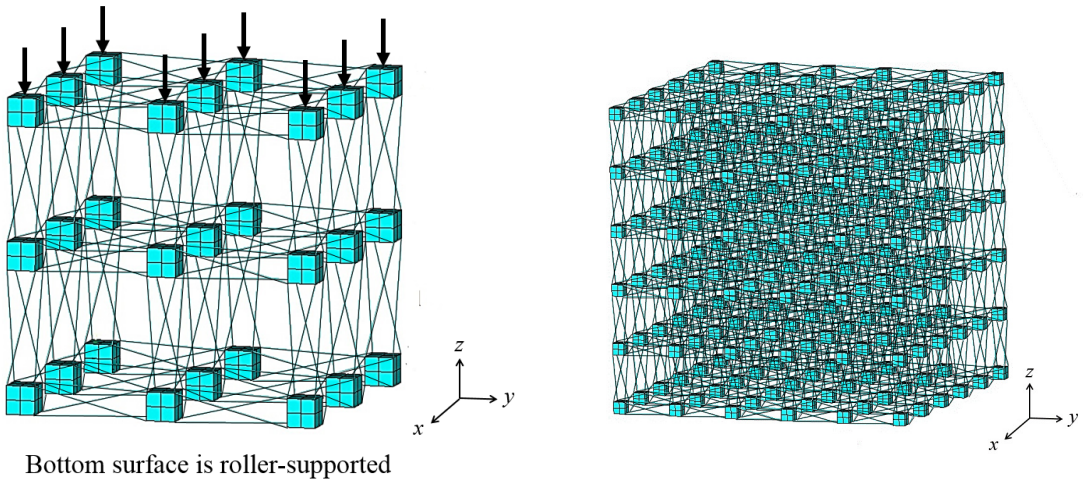

FIGURE 4.2: Examples of chiral lattice structures consisting of multiple unit cells. At left is a structure with two cells per side (2×2×2), and at right is a structure with five cells per side (5×5×5).

response [107]. Each cube was modeled using 24 SHELL 181 elements. This shell element has four nodes with six degrees of freedom at each node (three translations and three rotations). Its material properties were taken to be eight orders of magnitude greater than E of the ribs, so that effectively the cubes are rigid. As such, each cube is a hollow object where its six surfaces are discretized using four shell elements each. The merit of this treatment is that all nodes throughout the finite element model have the same degrees of freedom, especially rotations, which makes it straightforward to connect the ribs to the cubes. Note that it is tempting to use solid finite elements to model the cubes, but these elements have only translational degrees of freedom and hence it would be difficult to attach the ribs to the cubes since the sets of degrees of freedom for these elements are fundamentally different. Furthermore, by using four shell elements for each surface of a cube, there is a node present in the center of each cube's face, which is convenient for purposes of applying loads and supports.

Using this unit cell, lattices of multiple unit cells were constructed as shown in Figure 4.2, and various aspect ratios including 1.5, 1.8, 2, 2.2, 5, 10 and 20 were modeled.

To determine an effective Young's modulus of the lattices in response to axial compression

loading, equal point loads in the negative z direction were applied to the center node of each cube on the surface of the lattice (the surface with positive z as the normal direction) as shown in Figure 4.2 for the 2×2×2 lattice. Support conditions on the opposite surface of the lattice (the surface with negative z as the normal direction) consisted of zero z direction translation for all center nodes on cubes, plus a small number of additional constraints to prohibit rigid body motion of the lattice. Thus, the bottom surface of the lattice is supported by rollers and the Poisson effect is allowed to fully develop.

Finite element simulations were performed for five lattice structures (1×1×1 through 5×5×5), and for seven aspect ratios for each of these. Each finite element simulation provided the displacements and rotations of all nodes in the lattice. For each unit cell in a lattice, we computed effective strains throughout the unit cell by the following process.

Using the eight x direction displacements of each cube of one unit cell, as provided by the finite element simulation, we fit the following polynomial

$$u_x = a_1 + a_2x + a_3y + a_4z + a_5xy + a_6yz + a_7xz + a_8xyz \tag{4.1}$$

so that the coefficients $a_1 - a_8$ could be determined. Similarly, this process was repeated to obtain polynomials for the y and z direction displacements, namely u_y and u_z. Equation 5.1 allows one to embody the notion of average strain in a continuum model. Then, using the standard definition of small strains

$$\epsilon_{ij} = \frac{1}{2}(\frac{\partial u_i}{\partial x_j} + \frac{\partial u_j}{\partial x_i}) \tag{4.2}$$

where x_1, x_2 and x_3 correspond to x, y and z, respectively, we determine the effective strains throughout each unit cell of a lattice. Note that this entire process is identical to using the shape functions and $[B]$ matrix for an 8-node brick finite element. Thus, by using the $[B]$ matrix given in [107], along with the displacements of each cube in the unit cell, the effective strains throughout each unit cell are easily determined by evaluating $\{\epsilon\} = [B]\{d\}$.

4.3 Results and discussion

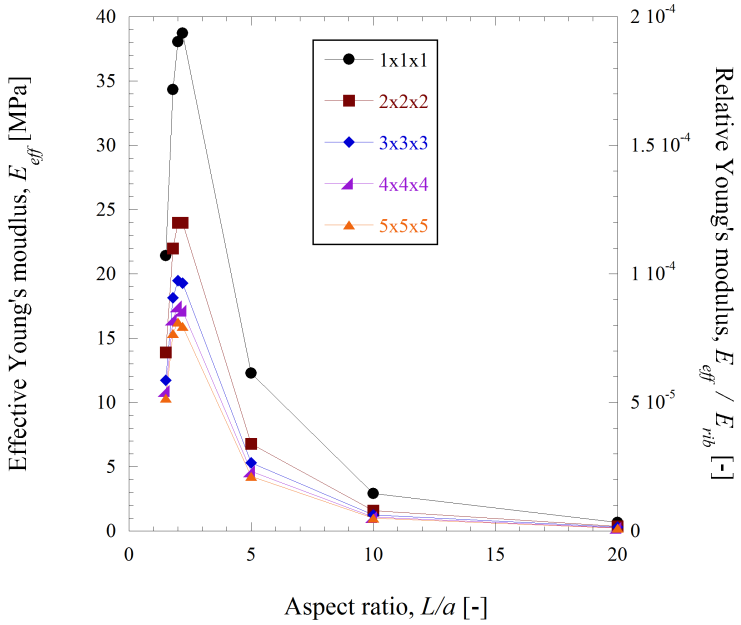

FIGURE 4.3: Effective Young's modulus in a principal direction vs. aspect ratio for chiral lattice.

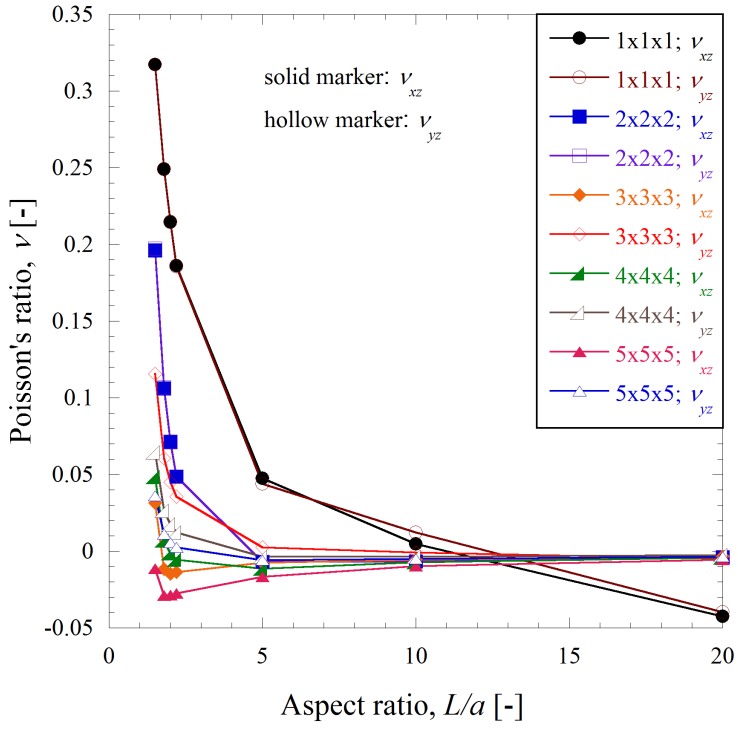

FIGURE 4.4: Poisson's ratio in a principal direction vs. aspect ratio for chiral lattice.

The effective Young's modulus in a principal direction versus aspect ratio for chiral lattice is shown in Figure 4.3. The relative Young's modulus, E_{eff}/E_{rib}, was also plotted in this figure. The effective Young's modulus first rises then decreases with aspect ratio. The decrease occurs because the round section rib elements are of constant diameter, but their length increases with aspect ratio. The lower modulus for the smallest aspect ratio is a result of the highly oblique angle of the ribs with respect to the nodules.

Poisson's ratio of the chiral lattice depends on the aspect ratio, as shown in Figure 4.4. Poisson's ratio in a principal direction tends to zero as relative rib slenderness increases except when there is only one cell. Poisson's ratio can be negative provided there are a sufficient number of cells, and for an appropriate range of aspect ratio near 2. The minimum in Poisson's ratio was delineated by conducting studies at fine intervals of Poisson's ratio. As the number of cells is increased, the lattice can be envisaged to approach a continuum for which continuum concepts are appropriate. The model

with only one cell is better viewed as a structure; it is included in the plot for completeness.

Lattices exhibit stretch twist coupling, as shown in Figure 4.5. Coupling increases with the aspect ratio except for a single cell; coupling decreases slowly with the number of cells.

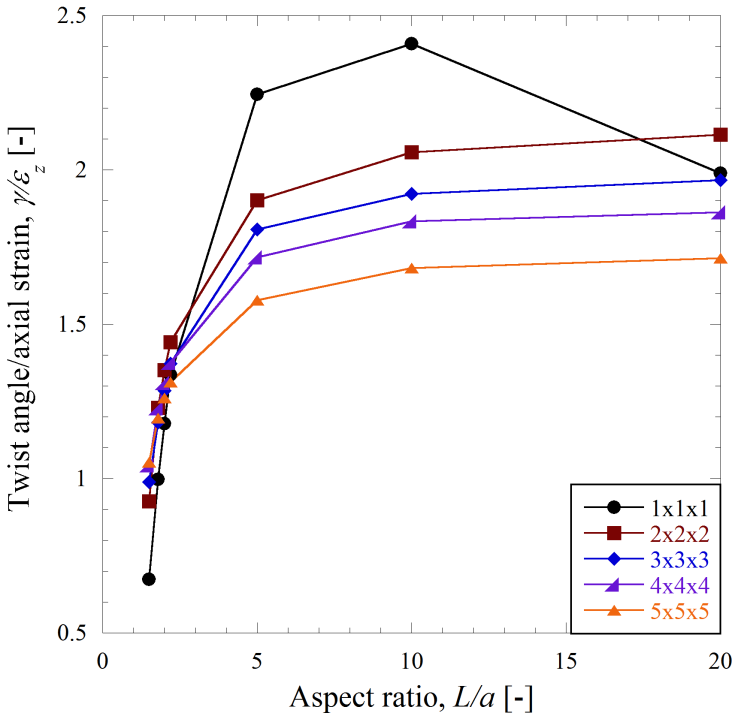

FIGURE 4.5: Stretch twist coupling, ratio of torsion strain / axial strain vs. aspect ratio for chiral lattice.

As the number of cells increases, the effective Young's modulus appears to converge to a constant value as shown in Figure 4.6. Convergence of the Poisson's ratio to an asymptotic constant value is slower. The Poisson's ratios for orthogonal directions are unequal: $\nu_{xy} \neq \nu_{yx}$. Lattices with an even number of cells on a side exhibit less anisotropy than those with an odd number of cells on a side. For a cubic classical elastic continuum, these Poisson's ratios are equal. More cells would be needed to probe convergence of Poisson's ratio to the constant, symmetric value of a classical continuum.

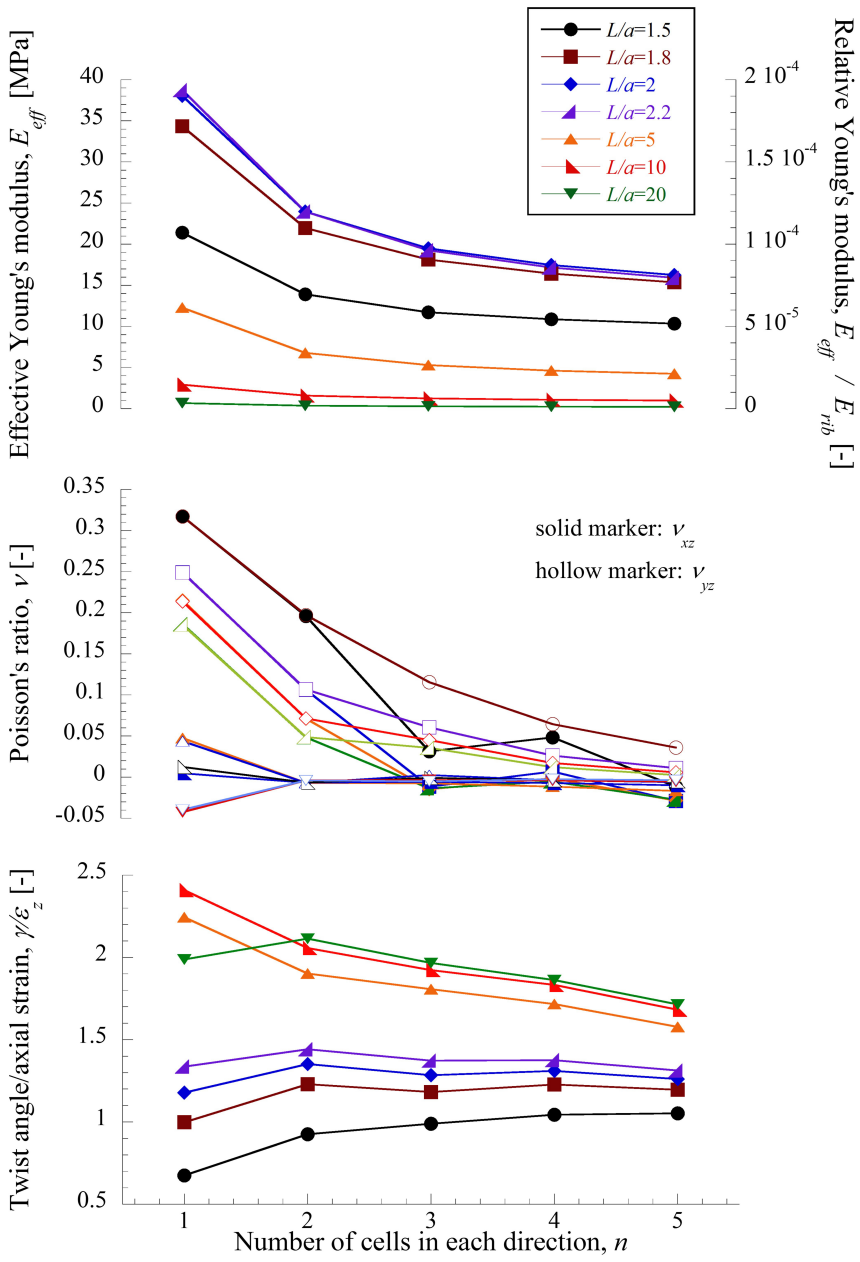

FIGURE 4.6: Effective Young's modulus, Poisson's ratio and stretch twist coupling vs. number of cells on a side.

Stretch twist coupling in the limit of a classical elastic continuum must be zero but in this series, no such asymptotic limit is reached. In the limit of sufficiently many cells, the lattice is expected to

be treatable as an equivalent continuum as is done with foams [10]. However, the continuum need not be classical. Use of a non-classical continuum model can account for some of the response of the chiral lattice as follows.

Stretch-twist coupling is associated with chirality. The twisting is either to the left or to the right. The material or structure must have the requisite asymmetry, specifically chirality, to exhibit such behavior. As for continuum models, classical elasticity does not distinguish left from right. The reason is that classical elasticity is a fourth rank tensor property. An inversion of all coordinate axes converts left to right but has no effect on tensor properties of even rank. Therefore more freedom is needed in a continuum model to account for chiral elastic effects. Cosserat elasticity provides sufficient freedom. Cosserat solids incorporate rotational degrees of freedom in the microstructure in addition to the usual translation. Cosserat solids exhibit a characteristic length scale in contrast to classically elastic solids. There are six elastic constants for a 3D isotropic, non-chiral Cosserat solid; nine constants for a 3D chiral solid. Cosserat elastic constants were calculated by analysis [33] of 2D chiral lattices [34] and determined experimentally in non-chiral foams [35] [36].

For 3D chiral solids viewed as a continuum, chiral Cosserat constitutive equations [32] are considered.

$$\sigma_{kl} = \lambda\epsilon_{rr}\delta_{kl} + 2G\epsilon_{kl} + \kappa e_{klm}(r_m - \phi_m) + C_1\phi_{r,r}\delta_{kl} + C_2\phi_{k,l} + C_3\phi_{l,k} \tag{4.3}$$

$$m_{kl} = \alpha\phi_{r,r}\delta_{kl} + \beta\phi_{k,l} + \gamma\phi_{l,k} + C_1\epsilon_{rr}\delta_{kl} + (C_2 + C_3)\epsilon_{kl} + (C_3 - C_2)e_{klm}(r_m - \phi_m) \tag{4.4}$$

The elastic constants C_1, C_2 and C_3 represent the effect of chirality. There are nine elastic constants compared with six for isotropic non-chiral Cosserat elasticity, and two for classical elasticity. As with the non-chiral case, characteristic lengths are defined based on ratios of tensorial constants; further detail is provided in an experimental study of non-chiral foam [35]. The chiral isotropic Cosserat model predicts the following.

(1) Stretch-twist coupling in a round rod of isotropic chiral material occurs and is a function of all nine elastic constants [32].

(2) Stretch-twist coupling in a round rod is nearly constant for small rod radius R; $\gamma/\epsilon \sim 1/R$ for large R much larger than the characteristic length.

(3) The transverse deformation associated with the Poisson effect is nonuniform though the material is assumed to be a uniform continuum.

The present chiral lattice has cubic symmetry and the shape is cubic, so a direct correspondence with isotropic continuum models is not to be expected. Nevertheless, the stretch twist coupling exhibited by the lattice and its slow decrease with size is anticipated in the continuum view. More detail on the Cosserat interpretation is to be provided elsewhere. The lattice model may also be modified to obtain orthotropic symmetry by providing different spacing of nodules in three orthogonal directions.

Poisson's ratio of individual cells vs. cell position in two transverse directions is shown in Figure 4.7 and Figure 4.8. As anticipated via the Cosserat continuum view, the Poisson effect is not homogeneous; it depends on position. The Poisson's ratio reported for the lattice as a whole, Figure 4.4, refers to the Poisson's ratio based on changes in the outer dimensions, corresponding to standard measurement methods. The lattice, which is cubic not isotropic, exhibits anisotropy in the Poisson effect.

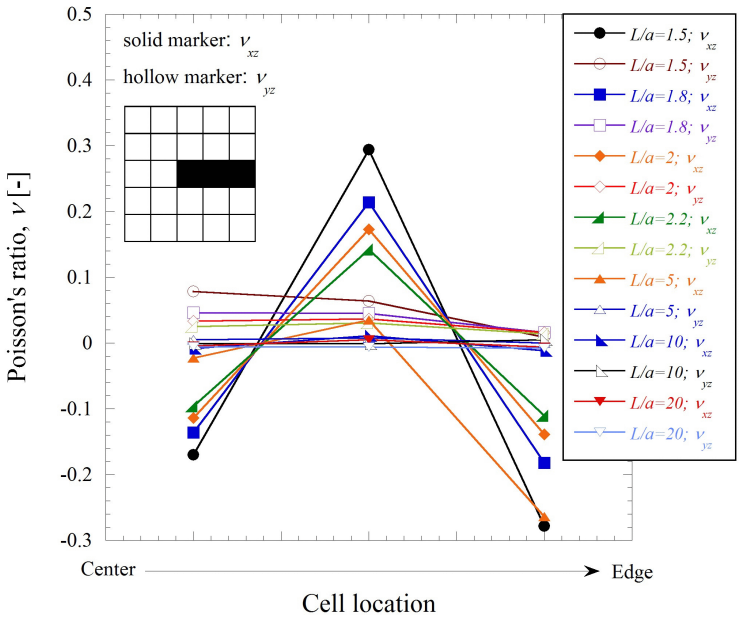

FIGURE 4.7: Poisson's ratio of individual cells vs. cell position in x direction for chiral 5×5×5 lattice.

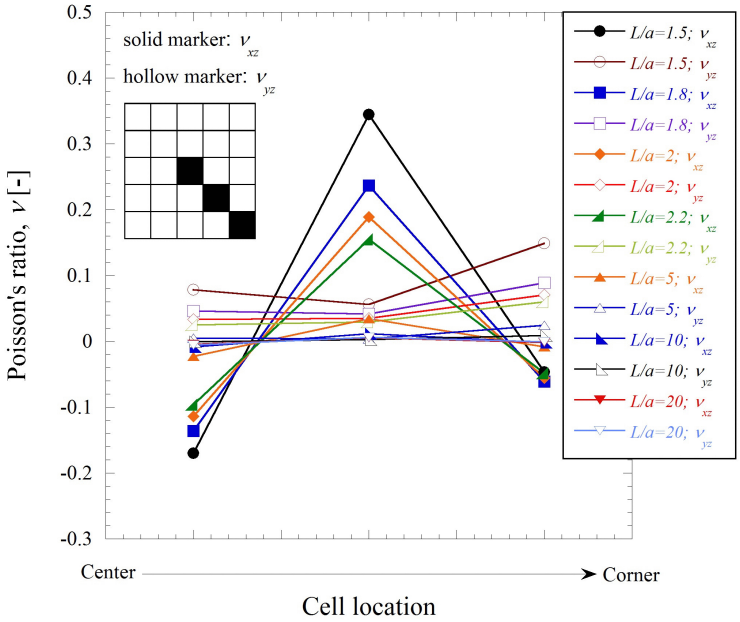

FIGURE 4.8: Poisson's ratio of individual cells vs. cell position in diagonal transverse direction for chiral 5×5×5 lattice.

The ribs in the present lattice were assumed to be made of a single material. Lattices with bi-material ribs have been studied in the context of control of thermal expansion or of piezoelectric sensitivity. For example, 2D lattices have been formulated and analyzed with controllable positive or negative expansion of large or small magnitude [11] [84], or zero thermal expansion [84] [96]. Also, 2D lattices with bi-material piezoelectric elements [14] were studied experimentally [15]; these lattices exhibit large values of piezoelectric sensitivity.

4.4 Conclusion

Chiral 3D lattices exhibit stretch-twist coupling that increases with relative slenderness of ribs. Poisson's ratio depends on geometry and can be negative. Chiral 3D lattices also exhibit Poisson's ratio that tends to zero as relative rib slenderness increases. The lattices have cubic structure and cubic symmetry. Isotropic solids are conceptually easier to model, therefore future development of lattices can aim to achieve material isotropy of the equivalent continuum.

Acknowledgment

Partial support from the NSF via Grant CMMI-1361832 and from the Petroleum Research Fund is gratefully acknowledged.

Chapter 5

Chiral three-dimensional isotropic lattices with negative Poisson's ratio

The following chapter has been published:
C. Ha, M. E. Plesha, R. S. Lakes, "Chiral three-dimensional isotropic lattices with negative Poisson's ratio", physica status solidi (b), 253 (7), 1243-1251 (2016).

Abstract Chiral three-dimensional isotropic cubic lattices with rigid cubical nodules and multiple deformable ribs are developed and analyzed via finite element analysis. The lattices exhibit geometry dependent Poisson's ratio that can be tuned to negative values. Poisson's ratio decreases from positive to negative values as the number of cells increases. Isotropy is obtained by adjustment of aspect ratio. The lattices exhibit significant size effects. Such a phenomenon cannot occur in a classical elastic continuum but it can occur in a Cosserat solid.

5.1 Introduction

Chiral materials and structures do not have a center of symmetry. There is a distinction between right and left so they are not invariant to inversion of coordinates. Quartz is a crystal that is chiral at the inter-atomic level [108]. There is left and right quartz. Chirality may also be designed in composites on various length scales. A planar chiral lattice with Poisson's ratio -1 [34] was

developed. The cell size was several centimeters. Poisson's ratio was -1, essentially independent of strain, via experiment and analysis. In contrast, negative Poisson's ratio of (3D) foams [42] and of (2D) honeycombs [87] with inverted hexagonal cells of bow-tie shape depends on strain. 2D structures with rotating hexamers and trimers [100] can exhibit negative Poisson's ratio of large magnitude. Negative Poisson's ratio materials have been called "anti-rubber" [48] or "auxetic" [49] [109].

Chiral 2D lattices have been analyzed for use as structural honeycomb [89] [90] that may be used in sandwich panels for airplane wings that morph or change shape. Buckling [91] [99] deformation of lattices of this type has been studied in a structural context. Lattices have been made with sensors and actuators [93]. These are referred to as smart structures. The lattices exhibit tunable band gaps [92] in wave propagation; potentially useful in reducing vibration.

Three dimensional lattices provide design freedom in contrast with foams [10], the structure of which is a consequence of the foaming method. 3D lattices with triangulated cells are stiffer than foams made of the same rib material. The reason is the ribs in the triangulated structure deform axially rather than in bending [102] as they do in foams. A negative Poisson's ratio 3D model was developed [103] in order to elucidate the deformation mechanisms of α-cristobalite [44], a negative Poisson's ratio form of silicon dioxide. A 3D structure containing corner-linked cubical nodules was developed [104] to model structure property relations of an auxetic microporous polymer [105]. 3D lattices with a negative Poisson's ratio [106] have been designed and fabricated.

Continuum mechanics is used when the size of an object is sufficiently larger than the size of its microstructure. In most analyses of cellular solids (e.g., [10]), the continuum is classical. Classical elasticity has no length scale. If the cell size is not small compared with length scales associated with the object or with strain gradients imposed on it, then it is sensible to use a more general continuum model. Cosserat (micropolar) elasticity [23] is a continuum elasticity theory which contains a length scale. Chiral 2D lattices [34] have been analyzed [33] [88] in the context of Cosserat elasticity.

In the present research, 3D chiral lattices [110] with cubic structure are designed to be elastically isotropic. The rationale of having isotropy is that it provides a simpler interpretation. Also, any

novel or unusual effects in an elastically isotropic solid cannot be ascribed to directional anisotropy. Size effects are studied and interpreted via Cosserat elasticity.

5.2 Analysis

Lattice structures were designed using the same finite element analysis (FEA) approach as we have done previously [110], using the FEA program ANSYS (release 14.5). Here the ribs are made thicker than in [110] and the aspect ratio is tuned to obtain elastic isotropy. Lattices were designed based on the unit cell (1×1×1) shown in Figure 5.1a. This cell was constructed using eight essentially rigid cubes at the corners of the cell (with cube side length a) and numerous deformable ribs (i.e., beams) connecting different corners of cubes to one another as shown. Note that chirality is introduced here. The center-to-center cube spacing is L, and aspect ratio of the unit cell is defined as L/a, which is always greater than unity. The ribs are made of steel with Young's modulus $E = 200$ GPa and Poisson's ratio $\nu = 0.3$, and have circular cross section with diameter of the ribs equal to 200 μm. The ratio of the cube side length to the rib diameter, a/d is then equal to 5. In prior analysis [110], this ratio was equal to 100. While such a ratio reveals behavior of stretch-dominated lattices, thicker ribs are pertinent to bend dominated structures and to the possibility of manufacture via 3D printing. A three dimensional isotropic chiral lattice was fabricated by fused deposition modeling (FDM) technology is shown in Figure 5.2. A Dimension Elite 3D printer with Stratasys ABSplus P430 thermoplastic was used here; the finest resolution is 0.178 mm. A prototype was first designed and was represented by SolidWorks 2015 in .stl (StereoLithography) format. Additional support materials (P400 SR) were removed by dissolving them in detergent and water.

A finite element model for the unit cell was constructed as described in [110]. Each rib was modeled using one beam finite element and each cube was modeled using 24 shell finite elements. The beam finite element includes shear deformation (i.e., they are based on Timoshenko beam theory). Nonetheless, despite the relatively low aspect ratio of the beams, ℓ_{rib}/d, in our model (e.g., for a lattice with L/a equal to 2, ℓ_{rib}/d is 7.07), shear deformations are not expected to be a

significant source of deformation; they are dominated by bending and torsion. The elastic modulus for the shell elements was taken to be eight orders of magnitude greater than E of the ribs, so that effectively the cubes are rigid. As such, each cube is a hollow object where its six surfaces are discretized using four shell elements each. The merit of this treatment is that all nodes throughout the finite element model have the same degrees of freedom, namely three translations and three rotations, which makes it straightforward to connect the ribs to the cubes. Furthermore, by using four shell elements for each surface of a cube, there is a node present in the center of each cube's face, which is convenient for purposes of applying loads and supports. Using this unit cell, lattices of multiple unit cells were constructed as shown in figure 5.1b, and various aspect ratios including 1.5, 1.8, 2, 2.2, 5, 10 and 20 were modeled.

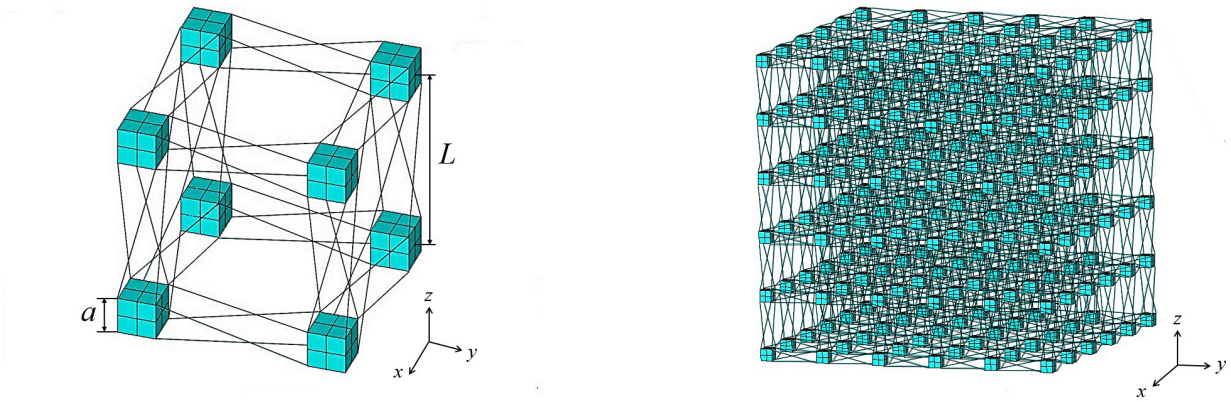

(A) (B)

FIGURE 5.1: (a) Unit cell of chiral lattice structure (1×1×1). (b) A structure with five cells per side (5×5×5). The aspect ratio is defined to be L/a, where $L/a > 1$. Note that the cubes and ribs shown here are not to scale; ribs are shown as lines for providing a better view of chirality.

To determine an effective Young's modulus of the lattices in response to axial compression loading, equal point loads in the negative z direction were applied to the center node of each cube on the upper surface of the lattice (the surface with positive z as the normal direction) as shown in Figure 5.3a for the 2×2×2 lattice. Support conditions on the opposite surface of the lattice (the

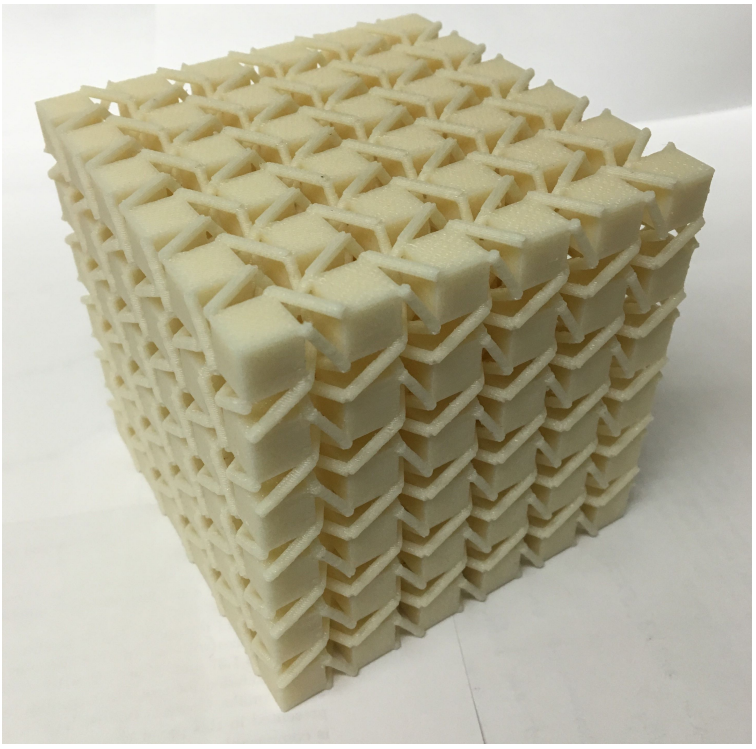

FIGURE 5.2: A photograph of a 3d-printed 5×5×5 lattice with an aspect ratio of 1.642. The lattice is about 92 mm on a side.

surface with negative z as the normal direction) consisted of zero z direction translation for all center nodes on cubes. To prohibit rigid body motion of the lattice, this surface also has the x displacement at one node and the y displacement at one node constrained, plus one more constraint to prevent rotation about the z direction. Thus, the bottom surface of the lattice is supported by rollers and the Poisson effect is allowed to fully develop. Note that there are other ways of applying uniform compression loading to the top surface of our finite element models. We have chosen to apply forces to nodes on the top surface, whereas another option is to prescribe z direction displacements. The disadvantage with the latter case is that it will not allow warping displacements in the z direction to develop, which we observe do occur due to the chirality of our model. Hence, among these two basic choices for applying loading (i.e., prescribed forces versus prescribed displacements) we believe using prescribed forces is more accurate for our purposes.

Elastic isotropy was achieved by tuning the aspect ratio such that the elastic relation $E/2G(1+$

$\nu) = 1$ between Young's modulus E, shear modulus G, and Poisson's ratio ν is obtained. To that end, pure shear loadings were applied to the lattices in order to determine an effective shear modulus. To model pure shear, equal point loads were applied to the center node of each cube on the appropriate surfaces of the lattice (the surfaces parallel to the xy and xz planes), as shown in Figure 5.3b. The surface whose normal is the negative z direction was constrained to eliminate rigid body motion of the lattice; namely, as shown in Figure 5.3b, the x, y and z displacements at one node, and y and z displacements at another node, and z displacement at yet another node are constrained. For the present chiral lattices, E and ν were obtained from a compression simulation and G from a pure shear simulation. The quantity $E/2G(1+\nu)$ was used as a measure of isotropy; this was computed for all lattice structures, except $1\times1\times1$ lattices, and for all aspect ratios. The results for the $1\times1\times1$ lattices were not used in this process because models with only one cell are better viewed as structures. Aspect ratios resulting in elastic isotropy were determined by fitting computed measures of isotropy (seven data points for each lattice structure) to a 5th degree polynomial using a least-squares best fit. Indeed, a lower degree polynomial best fit would probably be sufficient, but the merit to a 5th degree polynomial is that it is able to fit the number of data points we have (seven) better.

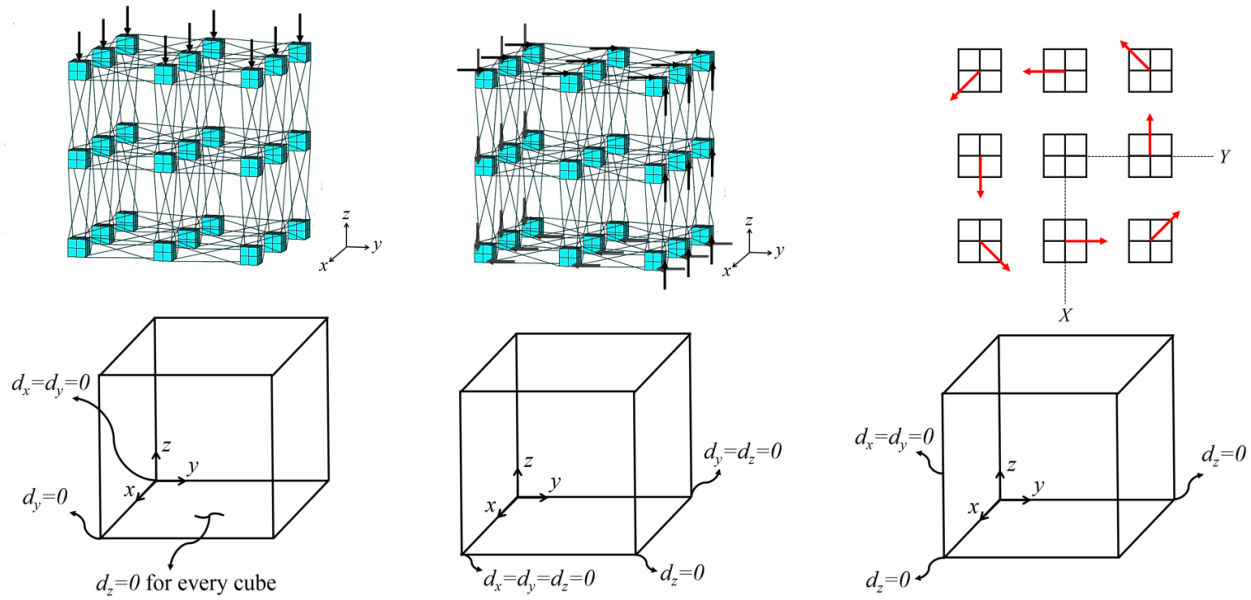

(A) (B) (C)

FIGURE 5.3: Loading cases for (a) compression, (b) pure shear, and (c) torsion, illustrated for 2×2×2 lattices. Support conditions (i.e., displacement constraints) are also shown. For (a) and (b), the arrows represent equal point loads. For (c), a local X and Y coordinate system is defined on the upper surface (i.e., the surface with positive z as the normal direction) with origin at the center of this surface, where these directions are parallel to the x and y global coordinate directions of the model. The arrows shown in (c) represent prescribed displacements in the x and y directions as given by Equation 5.11.

Finite element simulations were performed for all lattice structures (1×1×1 through 6×6×6), and for seven aspect ratios for each of these. The displacements and rotations of all nodes in the lattices were computed in each finite element simulation. Effective strains throughout each unit cell in the lattices were computed similar to our previous research [110] by using the polynomial interpolation

$$u_x = a_1 + a_2x + a_3y + a_4z + a_5xy + a_6yz + a_7xz + a_8xyz \tag{5.1}$$

The coefficients a_1 through a_8 were determined by fitting this polynomial to the eight x direction displacements for each cube in one unit cell of the lattice. Likewise, this process was repeated for determining polynomials for the y and z direction displacements, namely u_y and u_z. Equation

5.1 allows the average continuum strains throughout each unit cell to be determined by using the standard definition of small strains

$$\epsilon_{ij} = \frac{1}{2}\left(\frac{\partial u_i}{\partial x_j} + \frac{\partial u_j}{\partial x_i}\right) \tag{5.2}$$

where x_1, x_2 and x_3 correspond to x, y and z, respectively. Note that this entire process of computing the effective strains is identical to using the shape function $[N]$ and the strain-displacement matrix $[B]$ for an 8-node brick finite element

$$\{\epsilon\} = [B]\{d\} \tag{5.3}$$

where $[B] = [\partial][N]$. Thus, the effective strains throughout each unit cell were determined by evaluating Equation 5.3 with the $[B]$ matrix provided in [107] along with the displacements of each cube in the unit cell obtained from finite element the simulations.

For the three loading cases shown in Figure 5.3, the effective strains of each unit cell were averaged throughout the lattice, which gives rise to bulk effective strains of the lattice $\epsilon_{lattice}$ in a view of continuum. With this, one can determine mechanical properties of the lattice as follow. The effective Young's modulus of the lattice is given by

$$E_z = \frac{\sum_{i=1}^{(n+1)^2} P_i}{A_{eff}\epsilon_{lattice,z}} \tag{5.4}$$

where P_i represents an applied point load, n is the number of cells per side and A_{eff} is an effective area of the lattice which is defined as $(nL)^2$. Poisson's ratios for two orthogonal directions are determined as

$$\begin{aligned} \nu_{zx} &= -\frac{\epsilon_{lattice,x}}{\epsilon_{lattice,z}} \\ \nu_{zy} &= -\frac{\epsilon_{lattice,y}}{\epsilon_{lattice,z}} \end{aligned} \tag{5.5}$$

Finally, the effective shear modulus is found as

$$G_{yz} = \frac{\tau}{\gamma_{lattice,yz}} \tag{5.6}$$

where

$$\tau = \frac{\sum_{i=1}^{(n+1)^2} P_i}{A_{eff}} \tag{5.7}$$

When the size scale of specimens does not greatly exceed the microstructure size, classical elasticity may not apply. A generalized continuum theory such as Cosserat elasticity is more appropriate; the theory contains characteristic length scales. Cosserat theory of elasticity [17] [111], also known as micropolar elasticity [23], integrates a local rotation of points with respect to each other in addition to the usual translations assumed in classical elasticity.

The stress σ_{jk} (force per unit area) can be asymmetric. The resulting moment is balanced by a couple stress m_{jk} (a torque per unit area). The antisymmetric part of the stress is related to rotations. $\sigma_{jk}^{antisym} = \kappa e_{jkm}(r_m - \phi_m)$ in which κ is an elastic constant, ϕ_m is the rotation of points, called micro-rotation, e_{jkm} is the permutation symbol, and $r_k = \frac{1}{2} e_{klm} u_{m,l}$ is "macro" rotation based on the antisymmetric part of the gradient of displacement u_i. The constitutive equations [23] for linear isotropic Cosserat elasticity are

$$\sigma_{ij} = 2G\epsilon_{ij} + \lambda\epsilon_{kk}\delta_{ij} + \kappa e_{ijk}(r_k - \phi_k) \tag{5.8}$$

$$m_{ij} = \alpha\phi_{k,k}\delta_{ij} + \beta\phi_{i,j} + \gamma\phi_{j,i} \tag{5.9}$$

where δ_{ij} is the Kronecker delta and ϵ_{ij} is the microstrain tensor. In three dimensions, the quantities λ, G, α, β, γ, κ are six independent Cosserat elastic constants. An isotropic Cosserat solid thus has six elastic constants, whereas a classical elastic solid has two. If α, β, γ, and κ become zero, the equations of classical elasticity are recovered. The characteristic length in torsion is $\ell_t = \sqrt{\frac{\beta+\gamma}{2G}}$.

Cosserat effects may be revealed via size effects in torsion and in bending. Analytical solutions are available in the literature [26] [27] for round rods of isotropic non-chiral material. There is no known analytical solution for square bars of chiral material. Thus, the solution for an isotropic round bar with chiral material [26], which is exact, is used here

$$G = G_{asy}(1 + 6(\ell_t/r)^2)\left[\frac{1 - 4\Psi\chi/3}{1 - \Psi\chi}\right] \tag{5.10}$$

where $\chi = I_1(pr)/prI_0(pr)$, $p^2 = 2\kappa/(\alpha+\beta+\gamma)$, and I_0 and I_1 are modified Bessel functions of the first kind. Technical constants include the coupling number which is $N = \sqrt{\frac{\kappa}{2G+\kappa}}$ and the polar ratio is $\Psi = \frac{\beta+\gamma}{\alpha+\beta+\gamma}$. The ratio of Bessel terms inside the square brackets in Equation 5.10 reduces to 1 for $N = 1$.

To study size effects on our lattices, torsion loading was applied by prescribing displacements in the x and y directions (denoted as d_{xi} and d_{yi}, respectively) to each node i at the centers of all cubes on the upper surface of the FEA model (i.e., the surface with positive z as the normal direction, as shown in Figure 5.3c). To determine these displacements, an XY local coordinate system is defined in Figure 5.3c where the X and Y axes are parallel with the x and y axes of a global coordinate system, and the origin of the XY system is at the center of the upper face. The displacements d_{xi} and d_{yi} provide a uniform small rotation η of the upper surface about the $+z$ axis, which is equivalent to applying torque to the lattices in the same direction. The prescribed displacements are determined as follows. For a particular node i on the upper surface, its position vector, which provides its location relative to the origin of the XY coordinate system, is $\vec{r_i} = X_i\,\hat{i} + Y_i\,\hat{j}$, where X_i and Y_i are the coordinates of the node, and $\hat{i}$ and $\hat{j}$ are the usual unit vectors in the x and y directions, respectively. The surface is subjected to a rotation $\vec{\omega} = \eta\,\hat{k}$ where η is the prescribed small rotation of the surface and $\hat{k}$ is a unit vector in the z direction. Carrying out the cross product $\vec{d_i} = \vec{\omega} \times \vec{r_i}$ provides the prescribed displacements for node i as

$$d_{xi} = -\eta Y_i \quad \text{and} \quad d_{yi} = \eta X_i \tag{5.11}$$

Rigid body motion of the lattices are suppressed by imposing sufficient boundary constraints on the opposite surface (whose normal is the negative z direction); x and y displacements on one edge were constrained, and the z displacement was constrained at two corner nodes (see Figure 5.3c). Note that all nodes on the upper surface of the FEA model may displace in the z direction, thus the lattices are allowed to freely warp. In order to compute an effective shear modulus $G_{torsion}$ caused by the prescribed displacements, the reaction forces $\vec{F_i}$ for each of the nodes on the upper surface with prescribed displacements was retrieved and a net torque was obtained as

$$\vec{T} = \sum_{i=1}^{(n+1)^2} \vec{r_i} \times \vec{F_i} \tag{5.12}$$

This torque is in positive z direction and we denote its magnitude by T. The effective shear modulus for all lattice structures with different aspect ratios were then computed as

$$G_{torsion} = \frac{T(nL)}{\eta J} \tag{5.13}$$

where J is polar moment of inertia which was approximated as $J = \frac{1}{2}\pi(\frac{nL}{2})^4$. The asymptotic shear modulus G_{asy} and the characteristic length ℓ_t were determined by fitting the computed effective shear moduli $G_{torsion}$ of lattice structures (except the 1×1×1 lattice) to Equation 5.10 in nonlinear least-squares sense using MatLab; this fitting also provides p and the coupling number N. Here, the polar ratio Ψ was assumed to be 1.5; size effects are insensitive to Ψ except for size approaching zero. The radius r was taken as half the width of lattices.

Once G_{asy} and ℓ_t were found by fitting computed data to Equation 5.10, the relative stiffness Ω was computed by dividing Equation 5.10 by the asymptotic shear modulus G_{asy}, which gives the size effect as given in Equation 5.14.

$$\Omega = (1 + 6(\ell_t/r)^2)[\frac{(1 - 4\Psi\chi/3)}{1 - \Psi\chi}] \tag{5.14}$$

The elastic constants obtained by this process are technical constants not tensorial ones. The

reason is that in the absence of an analytical solution for torsion of a chiral square section bar, the solution for a round bar was used. Such a simplification cannot generate size effects via classical elasticity because classical solids do not exhibit size effects, and there is no elastic effect from chirality. The size effects must arise from generalized continuum; for example, Cosserat effects in the lattice.

5.3 Results and discussion

The effective Young's modulus and Poisson's ratio from the compression simulations and the effective shear modulus from the pure shear simulations for all lattice structures (1×1×1 through 6×6×6), and for seven aspect ratios are shown in Figures 5.4, 5.5 and 5.6. The objective is to find an aspect ratio that gives rise to elastic isotropy. Note that it was necessary to assume a modulus for rib material in order to determine mechanical properties of the lattices; the modulus of steel was chosen for convenience. Moduli of the lattice depend on the rib material and on geometry. The ratio of the effective Young's modulus of the lattice to the rib modulus, the relative Young's modulus, is independent of the assumed rib modulus, as shown in Figure 5.4. Most of the mass in the lattice is in the solid cubical nodules, so the usual modulus versus density plot is not appropriate here. The design is not intended to be light weight; studies of acoustic behavior, which depends on nodule mass, are planned. Poisson's ratio in two orthogonal directions (i.e., ν_{zx} and ν_{zy}) is found to be identical. As shown in Figure 5.5, when the aspect ratio is about 2, Poisson's ratio becomes more negative as the number of unit cells per side increases. Moreover, the effective shear modulus varies approximately by a factor of 10^5.

Note that we have performed a large number of simulations with lattices having different rib slenderness ratios, a/d. As expected, numerical values of the mechanical properties of the lattices depend on this ratio; stiffer lattices can be designed when thicker ribs are used. For example, when the rib slenderness ratio varies from 100 to 5, the magnitude of the effective Young's modulus of the lattices increases by approximately a factor of 400, and the Poisson effect was reduced by

approximately 20 %. However, trends in the mechanical properties of the lattices (e.g., the effective Young's modulus, Poisson's ratio and an effective shear modulus) remain the same. Regardless of the rib slenderness ratio, as the number of cells per side increases, a monotonically decreasing trend in the effective Young's modulus is seen, which tends to converge to a constant value, which is also observed for the effective shear modulus.

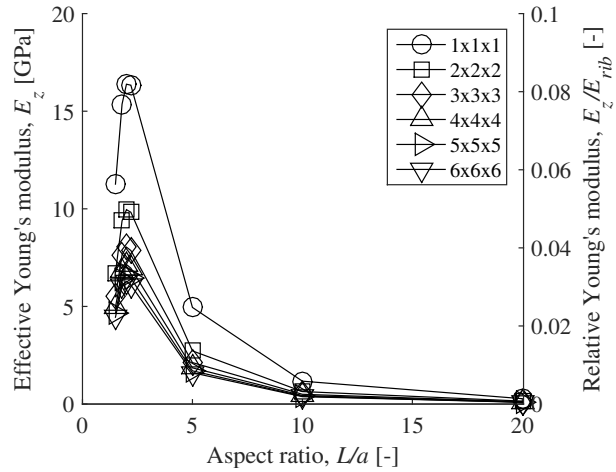

FIGURE 5.4: The effective Young's modulus and the relative Young's modulus in a principal direction versus aspect ratio.

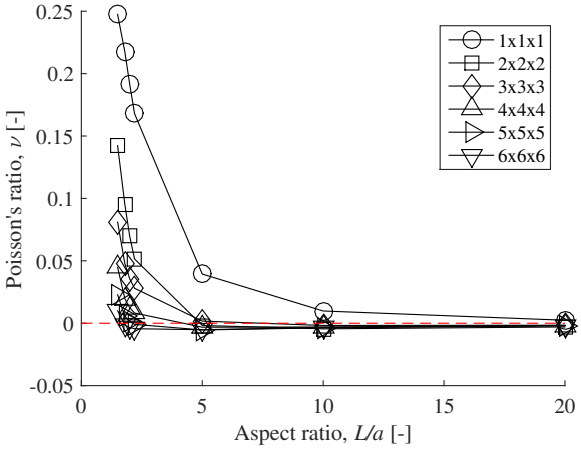

FIGURE 5.5: Poisson's ratio in a principal direction versus aspect ratio.

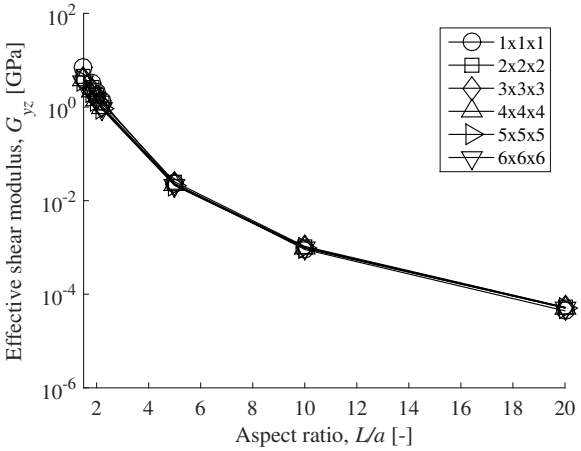

FIGURE 5.6: The effective shear modulus (from pure shear) in a principal direction versus aspect ratio.

With computed E_z, ν and G_{yz} above, the measure of isotropy, $E_z/2G_{yz}(1+\nu)$, was determined for all lattice structures except $1\times1\times1$ lattices and for all aspect ratios, as shown in Figure 5.7a. It was found that isotropy occurs when the aspect ratio is between 1.6326 and 1.6466. As seen in Figure 5.7b, the curves for all models are tightly clustered, and the goodness of fit was $R^2 = 1$. Aspect ratio L/a for isotropy was about 1.64, and this is independent of the rib slenderness ratio a/d over a range of values from 100 to 5.

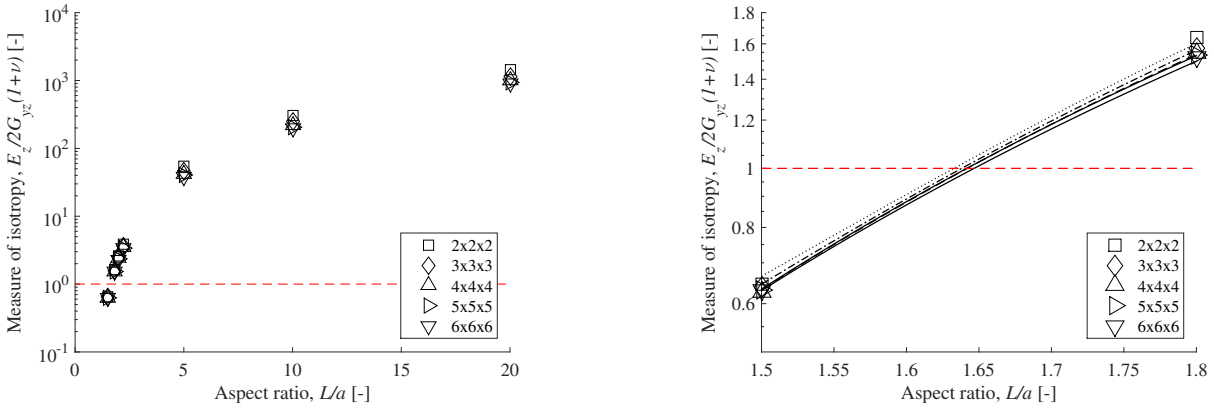

FIGURE 5.7: (a) The measure of isotropy vs. the aspect ratio for chiral lattice; a value of 1 indicates elastic isotropy. (b) An expanded scale showing fitting of data points with the least-squares 5th degree polynomial.

For three dimensional isotropic chiral lattices, the effective Young's modulus in a principal direction versus the number of cells per side is shown in Figure 5.8a. The relative Young's modulus is also plotted in this Figure. Note that the aspect ratio of these isotropic lattices was taken as 1.64; this value is an average of computed aspect ratios of all of the lattices that result in isotropy. The Young's modulus monotonically decreases and tends to converge to a constant value as the number of cells increases. A size effect in compression is anticipated in view of the Cosserat continuum in which chiral Cosserat solids have a length scale and coupling between compression and torsion [32], giving rise to stretch-twist coupling, as shown in Figure 5.8d. Poisson's ratio in this continuum view has radial dependence and size effects. A size effect in Poisson's ratio is revealed by FEA. Poisson's ratio is depicted in Figure 5.8b. When $n = 6$, Poisson's ratio becomes almost zero (e.g., $\nu = 0.0024$). Thus, negative Poisson's ratio is expected for a sufficient number of cells. By fitting the computed Poisson's ratio to a power function using nonlinear least-squares, Poisson's ratio becomes negative when n exceeds 7, and its asymptotic value is approximately -0.1393, as shown in Figure 5.9; the goodness of fit R^2 was 0.99. Note that a slow approach to asymptotic values is anticipated in the Cosserat continuum view. Cosserat elasticity allows the same range of Poisson's ratio [23] as

does classical elasticity. The Cosserat analysis applies to the full range of sizes and Poisson's ratio. Experiments are anticipated for materials with more cells. The effective shear modulus shown in Figure 5.8c has a similar trend compared to the effective Young's modulus.

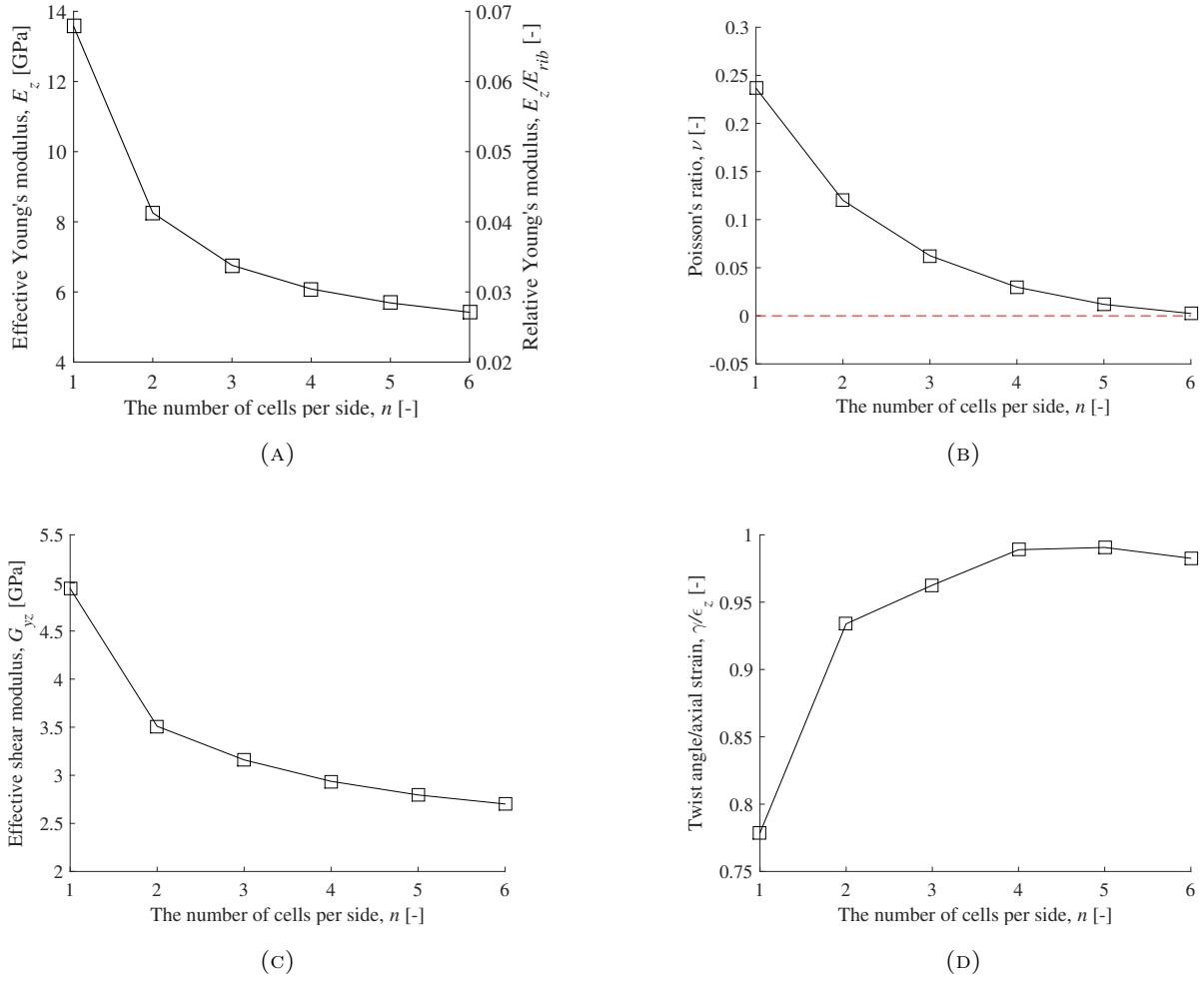

FIGURE 5.8: Three dimensional isotropic chiral lattices versus number of cells per side; (a) Effective Young's modulus. (b) Poisson's ratio. (c) Effective shear modulus (d) Stretch-twist coupling.

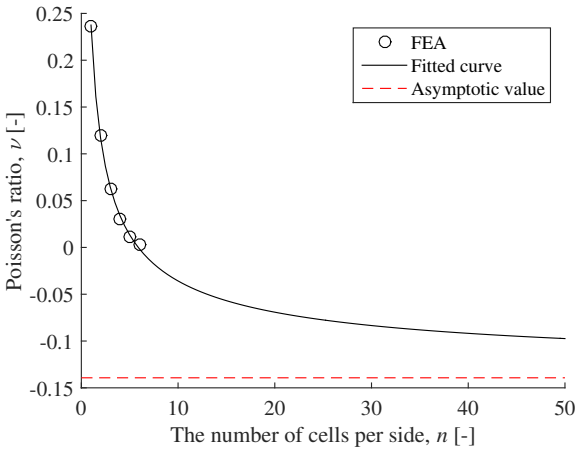

FIGURE 5.9: Interpolation and extrapolation of Poisson's ratio to a power function.

Results of torsion size effect studies are depicted in Figure 5.10. For three-dimensional isotropic chiral lattices with a/d equal to 5, $G_{asy} = 0.861$ GPa, $\ell_t = 1.55$ mm, $N = 1$, $\Psi = 1.5$. The goodness of fit was $R^2 = 0.99$. The model with only one cell is excluded for size effect studies, because it is better viewed as a structure. Classical elastic solids, unlike Cosserat solids, have a relative stiffness equal to 1 independent of size. Lattices presented in this paper clearly show significant size effects. The Cosserat characteristic length ℓ_t is comparable to the nodule spacing $L = 1.64$ mm. Moreover, since N was found to be 1, couple stress theory which is a special case of Cosserat elasticity, is appropriate. Cosserat solids with $N = 1$ (its upper bound) can be interpreted by couple stress theory [18] [25]; this corresponds to $\kappa \to \infty$; the characteristic length in Cosserat theory is equivalent to $\sqrt{3}$ times the length in couple stress theory. In the present paper, we use symbols after Eringen [23].

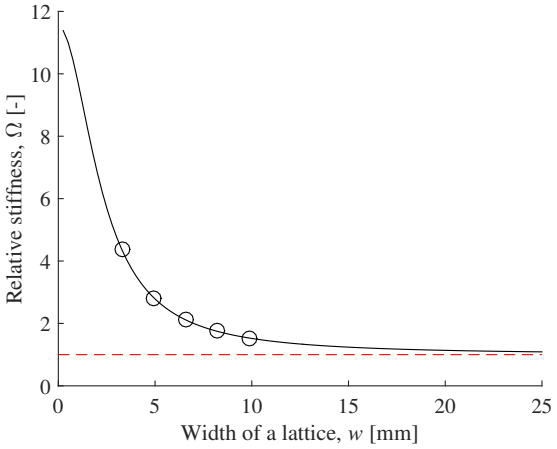

FIGURE 5.10: Size effects for three-dimensional isotropic chiral lattices for which $L/a = 1.64$ and nodule spacing $L = 1.64$ mm. Points are obtained via FEA. Curve is theoretical with $G_{asy} = 0.861$ GPa, $\ell_t = 1.55$ mm, $N = 1$, $\Psi = 1.5$; the goodness of fit, $R^2 = 0.99$. Classical elastic solids have $\Omega = 1$ (independent of width).

Size effects can also come from surface effects associated with incomplete cells, surface damage or cell connectivity that ends at the surface; such surface effects produce a softening size effect [112]. These surface effects compete with the stiffening effect of Cosserat elasticity [36]. This is of concern for foams that are cut by a machining process. The softening associated with surface effects can reduce apparent Cosserat parameters but cannot mimic a Cosserat effect because the effect is opposite.

Periodic boundary conditions can simplify analyses in which strain is uniform as in the calculation of Poisson's ratio in hexamer systems [113] [114]; also in analyses of wave motion. Because Cosserat elasticity entails sensitivity to gradients of rotation, and the size effects of interest require a free surface, periodic boundary conditions were not used in the analysis.

The constitutive equations for a Cosserat solid which is isotropic with respect to direction but not with respect to inversions are as follows [32]:

$$\sigma_{kl} = \lambda\epsilon_{rr}\delta_{kl} + 2G\epsilon_{kl} + \kappa e_{klm}(r_m - \phi_m) + C_1\phi_{r,r}\delta_{kl} + C_2\phi_{k,l} + C_3\phi_{l,k} \tag{5.15}$$

$$m_{kl} = \alpha\phi_{r,r}\delta_{kl} + \beta\phi_{k,l} + \gamma\phi_{l,k} + C_1\epsilon_{rr}\delta_{kl} + (C_2 + C_3)\epsilon_{kl} + (C_3 - C_2)e_{klm}(r_m - \phi_m) \qquad (5.16)$$

Elastic constants C_1, C_2 and C_3 are associated with the effect of chirality (i.e., noncentrosymmetry). If these constants vanish, the equations of isotropic micropolar elasticity are recovered. An exact solution for tension / compression of a round chiral Cosserat rod is available [32]; this serves as a guide for the analyst in seeking new effects. There is no available continuum solution for torsion of a square chiral bar, so a finite element approach such as the one used here is appropriate. While it is possible to obtain all six elastic constants of an isotropic Cosserat solid via experiment [35], available analysis does not suffice to determine all nine constants of a chiral solid. Therefore the characteristic length obtained is an effective one.

Chiral lattices may be of interest in the context of the stretch-twist coupling they provide, or for the potential as a framework for isotropic piezoelectric solids [115] which entail Cosserat effects. In such solids, polarization is coupled via an isotropic third rank tensor to the antisymmetric part of the stress.

5.4 Conclusion

Three dimensional isotropic chiral lattices were developed via finite element analysis. The effective Young's modulus, Poisson's ratio in two orthogonal directions and the effective shear modulus exhibit size effects. Both the effective Young's modulus and the effective shear modulus show convergence to a constant value with an increase of the cells in each side. Poisson's ratio can be negative with sufficient cells. Significant size effects, approaching a factor of five in torsion rigidity, occurred in the lattices. This reveals Cosserat elasticity.

Acknowledgment

Partial support from the NSF via Grant CMMI-1361832 and from the Petroleum Research Fund is gratefully acknowledged.

Chapter 6

Extreme Cosserat elastic cube structure with large magnitude of negative Poisson's ratio

The following chapter has been published:
C. Andrade, C. Ha, and R. Lakes, "Extreme Cosserat elastic cube structure with large magnitude of negative Poisson's ratio", Journal of Mechanics of Materials and Structures, 13 (1), 93-101 (2018).

Abstract A structure consisting of pivoting cubes is presented. It has zero Young's modulus, and zero bulk modulus. Poisson's ratio has large negative values in all directions; the structure exhibits anisotropy in Poisson's ratio. The structure is compliant in tension but rigid in torsion and bending. The Cosserat characteristic length tends to infinity.

6.1 Introduction

A 3D negative Poisson's ratio material based on transformed open cell polyurethane foam was reported [42] in 1987; it had a Poisson's ratio -0.7. It is possible to approach the isotropic lower limit -1 via structures or lattices with hinges. Negative Poisson's ratio was analyzed in a model of

rods, hinges and springs [116]; a value of -1 was calculated. A Poisson's ratio of -1 can be achieved in 2D structures containing rotating rigid units such as squares [117] connected by ideal hinges. Negative Poisson's ratio was also studied in 2D systems with rotating hexamers [113] [114] in the context of thermodynamic stability.

More recent designs with bars linked by ideal pivots allow the structure to undergo arbitrarily large volumetric strain with zero bulk modulus [118]. Negative Poisson's ratio materials have been called "dilational" [50] because they easily undergo volume changes but are difficult to shear.

It is possible to approach the isotropic lower limit -1 at small strain in analysis of a hierarchical two phase composite [50] if there is sufficient contrast between constituent properties. A 2D chiral lattice [34] exhibits a Poisson's ratio -1 over a range of strain as shown by experiment and analysis.

In the present research, we develop a structure made of cubes connected by pivots at their corners. Poisson's ratio and sensitivity to gradients are studied.

6.2 Cube structure

A structure is envisaged of cubes of side length a connected by pivots at the corners; Figure 6.1.

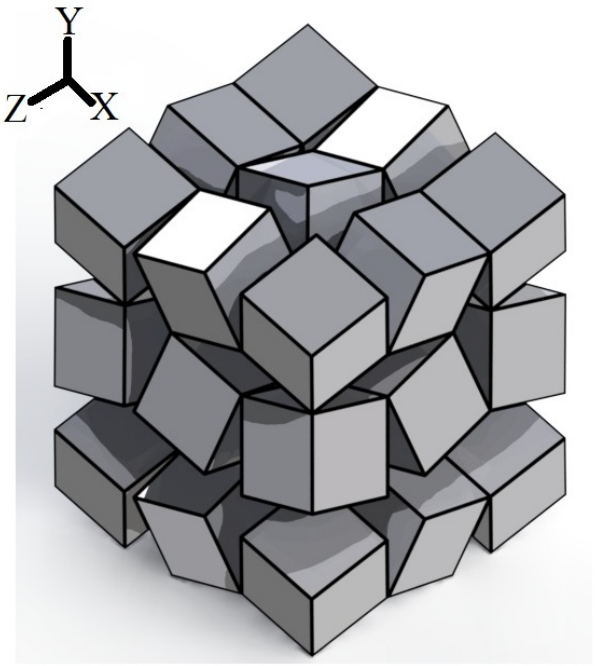

FIGURE 6.1: Cube structure, oblique view.

Views of the 3×3×3 cube structure along principal directions are shown in Figure 6.2. The rear layers of cubes are fully hidden. Deformation results in tilting of the cubes at the pivot points. This tilt causes void space to appear in the structure giving rise to a volume change. Transverse expansion of the structure under tension implies a negative Poisson's ratio.

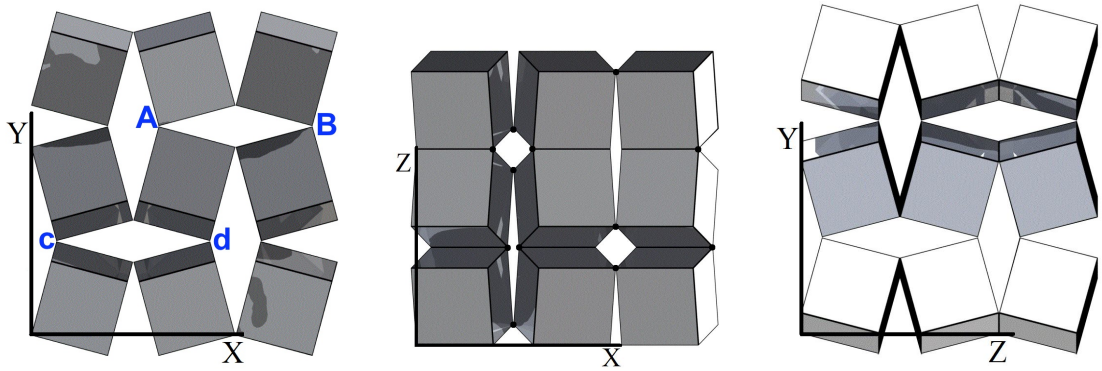

FIGURE 6.2: Cube structure, principal direction view.

6.2.1 Analysis and interpretation

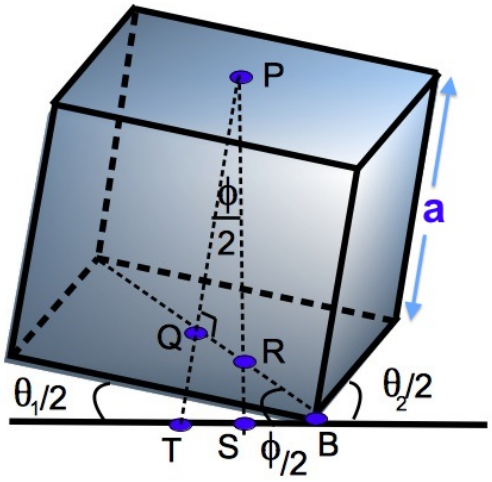

FIGURE 6.3: Analysis of cube structure deformation using two angles.

Elastic moduli and Poisson's ratio: two angles

We assume that the cubes are rigid and the pivots are ideal and allow frictionless rotation in all directions. Tensile deformation of the structure freely occurs in each axial direction: Young's modulus $E = 0$. Consequently, changes in volume occur with no resistance so the bulk modulus is zero. Shear forces in the X direction (Figure 6.2 left) on adjacent layers cause no deformation because the cube tilt cannot accommodate such motion. Shear forces in the Y direction (Figure 6.2 center) cause no deformation because edges are in contact, forming a hinge. Consequently the structure resists shear in all directions but allows tensile deformation, suggesting an extremal negative Poisson's ratio.

Strain ϵ depends on cube tilt angle ϕ, beginning at zero, as follows. Two angles are considered for simplicity and transparency; the third angle shown in Figure 6.2 right appears small and is neglected for the present. In Figure 6.3 consider the change in the length of a vertical line element during deformation. Points A and B (Figure 6.2 left) are at pivoted corners; distance a is the cube width. After deformation the vertical line from P, center of top face, intersects the bottom cube

face at R; because tilt occurs in two orthogonal directions, the intersection is along a diagonal. Points B, S and T, not necessarily collinear, are in a horizontal plane. The change in length is $\Delta L = PS - a$. The corresponding strain is $\epsilon_{yy} = \frac{PS-a}{a}$.

In triangle PQR, $cos\frac{\phi}{2} = \frac{PQ}{PR} = \frac{a}{PR}$. In triangle BQT, $tan\frac{\phi}{2} = \frac{QT}{BQ}$ so $QT = a\frac{\sqrt{2}}{2}tan\frac{\phi}{2}$. Also, $PT = a + QT = a(1 + \frac{\sqrt{2}}{2}tan\frac{\phi}{2})$, but in triangle PST, $cos\frac{\phi}{2} = \frac{PS}{PT}$ so $PS = PTcos\frac{\phi}{2}$ with $PT = a + QT$. Then, $PS = a(1 + \frac{\sqrt{2}}{2}tan\frac{\phi}{2})cos\frac{\phi}{2}$.

So the strain in terms of tilt angle is

$$\epsilon_{yy} = (1 + \frac{\sqrt{2}}{2}tan\frac{\phi}{2})cos\frac{\phi}{2} - 1 \tag{6.1}$$

If the angle is sufficiently large, the force has a line of action passing through a pivot. The force generates no moment to cause further rotation. For ϵ_{xx} as seen in the XY plane, the geometry is similar. However, viewed in the z direction, the effect of θ_1 alone gives the following in the linear regime of small angle.

$$\epsilon_{xx}^{\theta_1} = \frac{1}{2}tan\frac{\phi}{2} \tag{6.2}$$

but θ_2 rotates the corresponding point on the right face center down, reducing the distance, yielding a strain

$$\epsilon_{xx} = +\frac{1}{2\sqrt{2}}tan\frac{\phi}{2} \tag{6.3}$$

The Poisson's ratio is, for small angle,

$$\nu_{xy} = -\frac{\epsilon_{xx}}{\epsilon_{yy}} = -\frac{(\frac{1}{2\sqrt{2}}tan\frac{\phi}{2})}{(1 + \frac{\sqrt{2}}{2}tan\frac{\phi}{2})cos\frac{\phi}{2} - 1} \tag{6.4}$$

From the definition, $\nu_{yx} = 1/\nu_{xy}$. For small angle, $\nu_{xy} = -1/2$; $\nu_{yx} = -2$. The structure is therefore anisotropic even though Young's modulus $E = 0$ in all directions.

As for ϵ_{zz} as seen in the YZ plane, $\epsilon_{zz} = \epsilon_{xx}$ by virtue of a similar construction (neglecting tilt in the third orthogonal direction). So $\nu_{zx} = -1$; $\nu_{xz} = -1$.

This analysis makes the simplifying assumption that tilt in the third direction is small compared with tilt in the two directions considered. Tilt in all three directions is considered in the numerical approach below.

Bending

The classical bending rigidity of a bar is $M\mathcal{R} = EI$ with $\mathcal{R}$ as the principal bending radius of curvature, and I is the area moment of inertia. Moment M is about the y axis; the z axis is along the bar. The rigidity depends only on Young's modulus E not on Poisson's ratio ν. The effect of Poisson's ratio is to alter the deformation field. For positive Poisson's ratio the cross sections curve oppositely to the principal bending curve, the familiar anticlastic curvature. A negative Poisson's ratio causes curvature in the same direction as the bending curve, synclastic curvature [42]. The three-dimensional displacement field for pure bending of a linear elastic homogeneous, isotropic bar of rectangular section is

$$u_x = -\frac{z^2 + \nu(x^2 - y^2)}{2\mathcal{R}}, \quad u_y = -\nu\frac{xy}{\mathcal{R}}, \quad u_z = \frac{xz}{\mathcal{R}} \tag{6.5}$$

So if Young's modulus E tends to zero, it should be easy to bend the bar with no effort regardless of Poisson's ratio, provided the bar obeys classical elasticity.

The cube structure, while easy to deform in tension ($E = 0$), is rigid in bending. To visualize this, in the XY plane in the left image in Figure 6.2, expansion of a line along direction AB due to bending due to a Z moment is accompanied by contraction along line cd. The pivoted cube structure requires either expansion or contraction in all directions, so the structure is rigid to bending. Lines AB and cd are in different planes but that does not affect the argument because the classical motion has the same sign on the front and back.

Bending differs from axial extension in that bending entails gradients in strain and rotation.

Classical elasticity is insensitive to gradients but Cosserat elasticity allows such sensitivity. Rigidity of the structure to bending combined with a zero tensile Young's modulus implies a Cosserat characteristic length that tends to infinity. Again, the cubes are assumed to be rigid and the pivots are assumed to be ideal.

Elastic moduli and Poisson's ratio: numerical model, three angles

Figure 6.4 illustrates views of the structure along the principal directions and points on the center of cube faces that were used to compute Poisson's ratio via a numerical model. Moreover, θ_1 and θ_2 represent angles between cube edges when the structure is viewed in the corresponding principal directions.

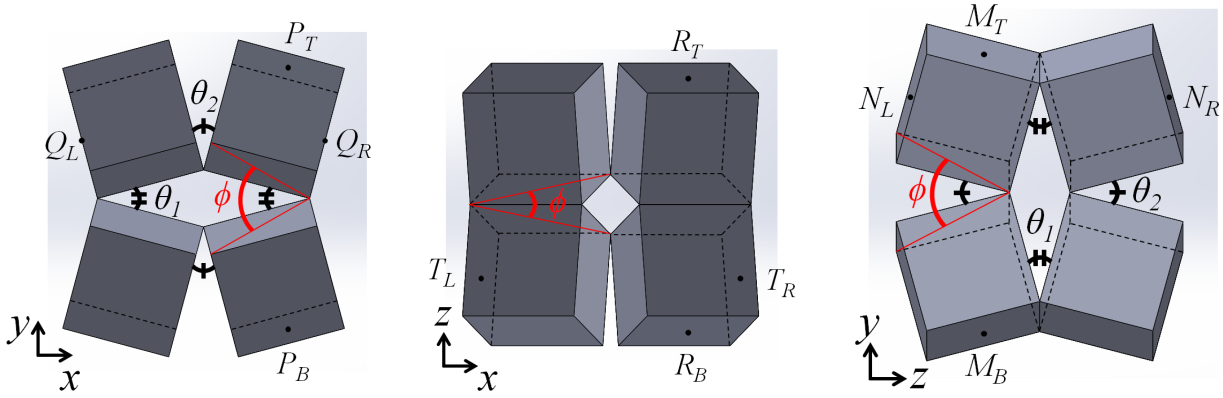

(A) (B) (C)

FIGURE 6.4: Cube structure viewed along the principal directions. All points are located at the center of cube faces. ϕ is an angle between diagonal lines of adjacent cubes. θ_1 and θ_2 represent angles between cube edges when the structure is viewed in the corresponding principal directions. For the structure shown, $\phi = 42.17°$, $\theta_1 = 30°$ and $\theta_2 = 28.96°$.

To determine the effect of motion in all three angles, the cube structure was modeled by SolidWorks commercial CAD software. In this analysis, a cube structure with a cube side length of 10 mm and with various inclined angles, ϕ, of 7.07, 14.13, 21.18, 42.17, 62.74 and 82.56 degrees.

Poisson's ratio in the principal directions was obtained as follows. The 'mate' feature in SolidWorks to was used make hinge constraints on corners. Distance was then measured using the software. The effect is purely geometrical so there was no need to use tools such as ANSYS APDL.

To obtain Poisson's ratio of the cube structure, strain and Poisson's ratio were determined in terms of the distances. First, strains in the principal directions due to the angle ϕ were computed, as given in the following equations.

$$\text{In } xy \text{ plane,} \tag{6.6a}$$

$$\epsilon_{xx} = \frac{|\overline{Q_{R,x}Q_{L,x}}| - 2a}{2a} \tag{6.6b}$$

$$\epsilon_{yy} = \frac{|\overline{P_{T,y}P_{B,y}}| - 2a}{2a} \tag{6.6c}$$

$$\text{In } xz \text{ plane,} \tag{6.6d}$$

$$\epsilon_{xx} = \frac{|\overline{T_{R,x}T_{L,x}}| - 2a}{2a} \tag{6.6e}$$

$$\epsilon_{zz} = \frac{|\overline{R_{T,z}R_{B,z}}| - 2a}{2a} \tag{6.6f}$$

$$\text{In } yz \text{ plane,} \tag{6.6g}$$

$$\epsilon_{zz} = \frac{|\overline{N_{R,z}R_{L,z}}| - 2a}{2a} \tag{6.6h}$$

$$\epsilon_{yy} = \frac{|\overline{M_{T,y}M_{B,y}}| - 2a}{2a} \tag{6.6i}$$

in which a is the cube side length and $|\overline{Q_{R,x}Q_{L,x}}|$ denotes a distance between Q_R and Q_L in the x direction in the xy plane after deformation. ϵ_{xx} is then equal to $(|\overline{Q_{R,x}Q_{L,x}}| - 2a)/2a$. With strains found in Equation 6.6, Poisson's ratio in the principal directions are

$$\nu_{xy} = -\frac{\epsilon_{xx}}{\epsilon_{yy}} = -\frac{|\overline{Q_{R,x}Q_{L,x}}| - 2a}{|\overline{P_{T,y}P_{B,y}}| - 2a} \tag{6.7a}$$

$$\nu_{xz} = -\frac{\epsilon_{xx}}{\epsilon_{zz}} = -\frac{|\overline{T_{R,x}T_{L,x}}| - 2a}{|\overline{R_{T,z}R_{B,z}}| - 2a} \tag{6.7b}$$

$$\nu_{zy} = -\frac{\epsilon_{zz}}{\epsilon_{yy}} = -\frac{|\overline{N_{R,z}R_{L,z}}| - 2a}{|\overline{M_{T,y}M_{B,y}}| - 2a} \tag{6.7c}$$

From numerical results, it was found that $\epsilon_{xx,num}$ from the xy and the xz planes were identical (i.e., $\epsilon_{xx,num}^{xy-plane} = \epsilon_{xx,num}^{xz-plane}$). Similarly, $\epsilon_{yy,num}$ in the xy plane agreed exactly with one in the yz plane, and $\epsilon_{zz,num}$ were the same for the xz and the yz planes (i.e., $\epsilon_{yy,num}^{xy-plane} = \epsilon_{yy,num}^{yz-plane}$ and $\epsilon_{zz,num}^{xz-plane} = \epsilon_{zz,num}^{yz-plane}$). This confirms that cube structures modeled by the employed CAD software were correctly designed and interpreted since computed strains were the same regardless of views in different principal directions. As a result, the superscript of strains obtained numerically were omitted in this paper as follows, unless stated otherwise.

A comparison of strains between analytical and numerical approaches was made, as shown in Figure 6.5.

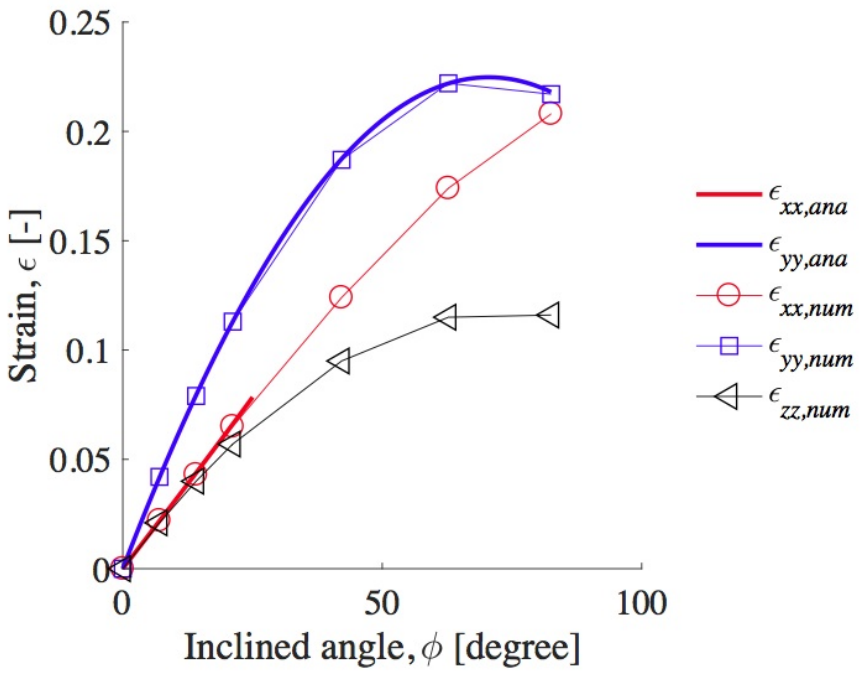

FIGURE 6.5: Strains of a cube structure as a function of the angle ϕ.

The strain ϵ_{yy} between these two approaches agreed well with one another throughout the range of ϕ. The strain ϵ_{xx} also agreed over the narrower range of strain consistent with simplifying assumptions in that analysis including neglect of the effect of the tilt in the third orthogonal direction and of higher nonlinearity.

As illustrated in Figures 6.4a and 6.4c, the effect of the orthogonal tilt is small when the angle ϕ, is small. From this, it was expected that $\epsilon_{xx,num}$ and $\epsilon_{zz,num}$ to be similar when ϕ is small, and this can be observed in Figure 6.5. In this regime (i.e., for small ϕ), strains are almost linear as a function of angle. In contrast, nonlinearity occurs when ϕ is large. The effect of the tilt in the third orthogonal direction can be quantified by θ_1 and θ_2 that represent angles between adjacent cube edges when the structure is viewed in the corresponding principal directions. For small ϕ, these two angles are similar.

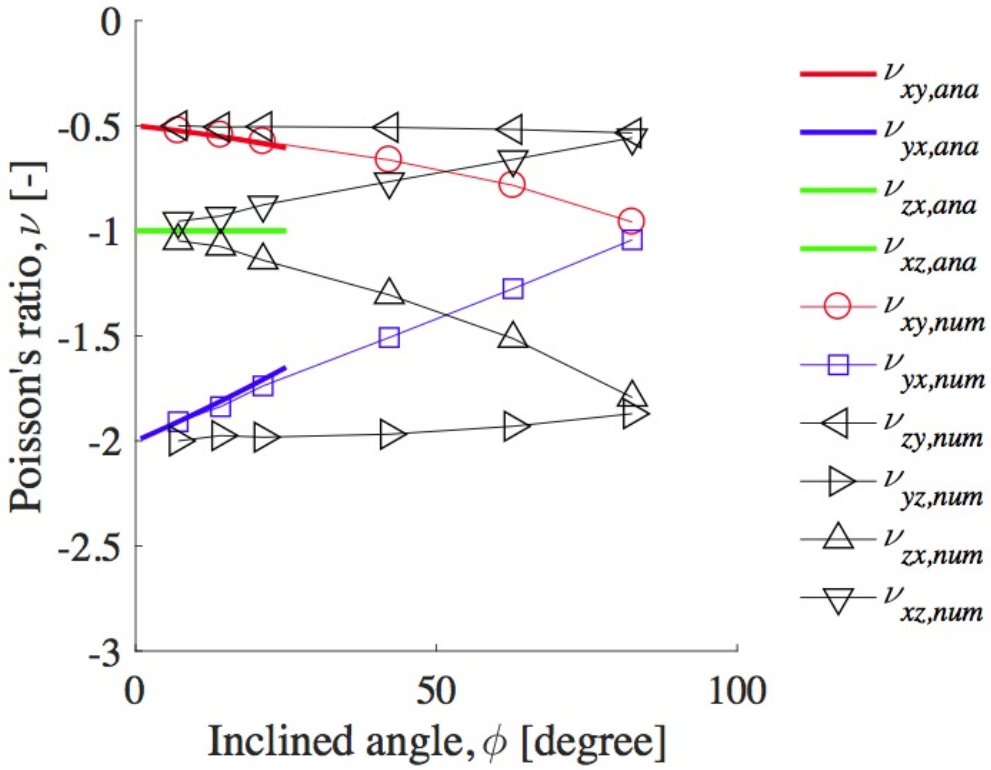

FIGURE 6.6: Poisson's ratio in all the principal directions.

In summary, for small strain, the Poisson's ratios ν_{zx} and ν_{xz} obtained by two angle analysis and three angle numerical methods are equal with a value of -1. For other directions, the simple analysis and numerical results agree within the appropriate small angle range.

6.3 Physical model

Physical models were made to aid visualization and to illustrate the concepts. An initial model was made with cubes cut from polymer foam. A design was assembled digitally using Solidworks 2016. Cubes were prepared using Solidworks in .stl (StereoLithography) format for export to a 3D printer. The method was fused deposition method (FDM). The print resolution (i.e., the minimum size of a stand alone feature) was 0.5 mm. These cubes, 2 cm wide, were manufactured using a Dimension

Elite 3D printer, of Stratasys ABSplus P430 thermoplastic. Pivots can be made by 3D printing but they are subject to considerable friction which would interfere with demonstration of the concept. Therefore a fibrous tape was cut into a dog-bone shape. Segments were taped to adjacent cubes, leaving the slender portion as a pivot. A 3×3×6 model was made with Z as the long direction.

The physical model was observed to be easy to stretch provided only one or two cubes on each end were held gently and allowed to rotate. The structure expanded fully in tension under its own weight. The model was rigid to torsion as well as to shear in different directions. The model was also rigid to cantilever bending. In both cases, slight movement associated with slack in the pivots was observed.

6.4 Discussion

Several negative Poisson's ratio structures with rotating hinged elements are known. In addition to rotating squares [117], one can have rotating rhombi [119], triangles [120], edge connected cuboids of different size [121], and complex hinged structures [118]. Such pivoted structures, including the present one, exhibit a hard nonlinearity when the structural elements come into contact and when the lattice is fully extended. Even so, the geometry of hinged structures has been used to help explain [119] the negative Poisson's ratio of materials in which the effects arise on the molecular scale.

For the present ideal structure with rigid cubes and frictionless pivots, Young's modulus is zero in tension provided the end cubes are allowed to rotate as is the case in stress control. Although tensile deformation freely occurs, the structure is rigid in bending and torsion. Classical elasticity cannot account for such behavior but Cosserat [17] (micropolar [23]) elasticity, which allows sensitivity to gradients, can do so. Cosserat theory provides characteristic length parameters as elastic constants. If the specimen size is not too much greater than the characteristic length, size effects are observed in bending and torsion; the effective modulus in bending exceeds the true Young's modulus in tension. Such effects are known in a variety of foams including negative Poisson's ratio foam [38].

However the range of Poisson's ratio is the same in Cosserat solids as in classical ones so coarse cell structure is not needed to control the Poisson's ratio [122]. The cube structure will be rigid to bending and torsion independent of how small the cubes are in comparison with the specimen size, provided the cubes are rigid and the pivots are ideal. This implies a characteristic length that is infinitely large. Such singular behavior arises from the geometrical constraints in a highly idealized structure. Similar singular behavior likely occurs in other negative Poisson's ratio hinged structures and in structures made using sliding elements [123]. Extremely large Cosserat effects leading to folding and faulting can occur in highly anisotropic materials that admit couple stress [124]. Three dimensional structures are of particular interest because in 3D, classical bending can occur either via shear at constant volume, as in rubbery materials, or of via local volume change with constant shape, as when Poisson's ratio tends to -1. A material or structure that does not allow bending cannot be classically elastic.

6.5 Conclusions

A structure of pivoting cubes is presented. It has negative Poisson's ratio of large magnitude in each direction and a tensile modulus of zero. It is rigid to bending, therefore it is not classically elastic. The structure behaves as an extreme Cosserat solid.

6.6 Acknowledgements

We gratefully acknowledge support of this research by the National Science Foundation via Grant CMMI-1361832 and by the SURE program.

Chapter 7

Design, fabrication, and analysis of lattice exhibiting energy absorption via snap-through behavior

The following chapter has been published:
C. Ha, R. S. Lakes, and M. E. Plesha, "Design, fabrication, and analysis of lattice exhibiting energy absorption via snap-through behavior", Materials & Design, 141, 426-437 (2018).

Abstract

In this study, an energy absorption lattice, comprised of multiple tetra-beam-plate unit cells with negative stiffness, was designed, fabricated by selective laser sintering method, and analyzed both numerically and experimentally. Snap-through behavior of the unit cell developed due to negative stiffness caused by geometric nonlinearity from large deflection of the constituent elastic beams, resulting in energy absorption. A criterion for the unit cell to achieve the snap-through behavior was investigated numerically in terms of the beam slenderness ratio and the inclined angle. This approach was chosen to facilitate control of energy dissipation performance and further design space such as tuning force threshold. The unit cell with the selected geometric parameters was then created and used to construct the energy absorption lattice. Load-displacement relationships

of the lattices obtained from cyclic loading tests disclosed an area enclosed by two distinct loading and unloading curves, which indicates energy dissipation. This was shown both numerically and experimentally. Drop tests were also performed to investigate energy loss of the lattices due to an impact. An energy absorption phenomenon was revealed by observing a reduced rebound height when the lattice exhibited the snap-through behavior.

7.1 Introduction

Bistable mechanisms are useful for a device that is to achieve stable states in two distinct positions without power input. Due to their notable behavior providing low power operation and prevention of external disturbances, such mechanisms have been applied to various engineering applications, including microelectromechanical systems (MEMS) [125] [126]. Examples are switches [127] [128] [129] [130], valves [131], shock sensors [132] [133], relays [134], binary modular reconfigurable robots [135] and devices for energy harvesting from vibrations [136].

Three main types of the bistable mechanism based on different design concepts have been reported in the literature. Latch-lock mechanisms were studied in [137] and [138], however complex actuation to lock and unlock was required for the mechanisms. Hinged multi-segment mechanisms were introduced in [139], [140], and [141]; these are based on zero friction, zero clearance and zero stiffness, which is difficult to accomplish with MEMS fabrication processes. Buckled beam or membrane mechanisms having residual-compressive-stress were developed in [142], [143], and [144], yet residual stress is cumbersome to achieve or control in bulk-fabricated structures. In addition, a monolithic mechanically-bistable mechanism utilizing double curved beams was studied recently, which does not rely on hinges, latches or as-fabricated internal stress (i.e., residual stress) [130].

Systems having the bistable mechanism require energy only when they are to be loaded (i.e., a charging state). At a state of unstable equilibrium (also called as a metastable state), any minor perturbation (e.g., loading, boundary condition, etc.) can give rise to one of the two stable states; the transition between the two stable states is commonly referred to as a *snap-through* process.

When structures snaps from their initial shape into a buckled shape, a considerable amount of energy is released from the system, revealed as a load drop (i.e., negative slope) in load-displacement characteristics [145]. This process is caused by their negative stiffness behavior near the unstable equilibrium position(s). In contrast to most elastic materials that tend to resist deflection or deformation in response to an applied load (i.e., positive stiffness or positive force to displacement ratio), negative stiffness is, in general, understood as a reversal of the usual directional relationship between force and displacement in pre-strained objects. For example, buckled flexible tubes forming kinks contain stored energy at a state of equilibrium [52]. Experimentally, lumped systems containing discrete buckled tubes [53] and models of single foam cells [43] were found to exhibit negative structural stiffness.

Objects or structures with negative stiffness are usually unstable by themselves [58]. A constrained buckled column with the S-shaped configuration is in unstable equilibrium [54]. Snap-through behavior from negative stiffness can be caused by pressing laterally on the column. One can stabilize the column with a lateral constraint. Structures with negative stiffness can also be stabilized by employing heterogeneous materials or composites. This approach can provide extreme values of material damping [55] [58], stiffness [61], and/or thermal expansion [57] that are greater than those of either constituent. This behavior surpasses classical bounds [62], where composite properties cannot exceed the properties of the constituents. These bounds are based on theorems assuming that each constituent does not entail initial stored energy. In contrast, structures with negative stiffness initially contain stored energy; composite stability can be enhanced by viscoelastic dissipation, if present [61]. As discussed earlier, structures with buckled flexible tubes subjected to sinusoidal load can achieve both negative stiffness and very large increases in damping [53]. The negative slope in a Lissajous figure for a tube in the post-buckled condition indicates negative stiffness. $\tan \delta$, representing damping, is negative since the phase angle δ between load and deformation is greater than 90° for the post-buckled tube. For applications requiring reduction of noise and/or vibration (e.g., sensors, hypersonic vehicles, etc.) a combination of high stiffness and high dissipation may be of interest.

Recently, negative stiffness behavior has been of interest to various engineering applications due to its unique mechanical properties [63], including (i) energy harvesting/dissipation, (ii) shock/vibration isolation and damping, and (iii) sensitivity enhancement.

(i) As a result of experiments and finite element simulations, the response of assemblies consisting of topologically interlocked cube-shaped elements have showed a pronounced nonlinear response to out-of-plane point loadings (i.e., indentation), which featured a distinct hysteresis, post-peak softening, a negative stiffness during unloading, and localized irreversible rotations [64]. This interlocking-based structure is capable of providing considerable energy dissipation and substantial resistance to large-scale fracture propagation. 3D-printed porous elastomeric structures modeled by micro-architected design were studied, which showed distinct load response with direction-dependent behavior including negative stiffness [65]. This work revealed that cellular solids via the micro-architected design can tailor mechanical response independently and suggested that such ordered materials may replace stochastic foams in energy absorption applications. Negative stiffness honeycombs comprising unit cells from curved beam structures were found to exhibit substantial mechanical energy absorption and to achieve a recovery to their original shape even when the honeycombs undergo compression beyond densification [66] [67]. Such honeycombs are of interest to applications such as impact absorbers and protective devices. With the use of additive manufacturing, specifically selective laser sintering technology, the authors in [68] designed and showed that constrained bistable structures exhibiting negative stiffness behavior can enhance system damping and control dynamic behavior, indicating that the system is functional for applications requiring energy absorption or vibration isolation.

(ii) An analytical study of an overall-stable system with negative stiffness element inclusions showed that the ability of tuning purely elastic wave propagation can be greatly enhanced, and even further tuning is possible when alterable damping is added to the system [74]; adequate control of negative stiffness element can prevent propagation of long-wavelength waves. An improvement of damping ratio by several orders of magnitude was modeled for flexural waves propagating within layered continuous/periodic structures having negative stiffness inclusions [72]. With the

use of bistability and negative stiffness, a combination of quasi-zero-stiffness (QZS) behavior and snap-through action that provides passive shock and vibration isolation was established [71]. This system is useful for applications that need to protect sensitive payloads from surroundings (e.g., forces and accelerations) that exceed a maximum limit. A load-bearing structure with dynamically controllable stiffness was developed experimentally based on a combination of active vibration control and nonlinear negative stiffness [73]; this structure was capable of fast and useful dynamic stiffness control regardless of the static load, and potential applications include humanoid robotic limbs and lightweight adaptive vibration isolators.

(iii) A study of negative stiffness behavior of prismatic tensegrities revealed that instabilities via snap-through behavior and specific negative structural stiffnesses as a result of the presence of multiple stable states were possible when the topological relations and geometric parameters of these structures met certain criteria in terms of three dimensionless parameters [77]. Such structures are useful in sensitivity enhancement and energy storage/absorption, yet further research is needed to reveal their mechanical responses. Energy dissipation due to snap-through behavior in negative stiffness systems may be of use in ameliorating undesired vibrations and waves. Snap-through behavior has also been used to enhance the effective piezoelectric response of structures with rib elements [78].

Negative stiffness differs from a negative Poisson's ratio, in which a material expands laterally subjected to tensional load [42] [44] [46]. Poisson's ratio, ν, is defined as the negative of the ratio of transverse strain of a stretched or compressed object to its longitudinal strain: $\nu = -\epsilon_{\text{trans}}/\epsilon_{\text{long}}$. For most solids, ν is between 0.25 and 0.33. Foams with ν as small as -0.7 with enhanced resilience [42] [43] and a planar chiral lattice with ν equal to -1 [45] have been made. For isotropic materials, Young's modulus, E, and shear modulus, G, are related to Poisson's ratio, ν, by relations such as $E = 2G(1 + \nu)$.

In this paper, a lattice that can exhibit energy absorption via snap-through behavior was designed, fabricated by 3D printing via selective laser sintering (SLS) method, and analyzed in both numerical and experimental approaches. The lattice comprised of multiple tetra-beam-plate unit

cells incorporating elastic beams and plates. All connections were designed as fixed supports for the purpose of 3D printing fabrication. The unit cell utilized negative stiffness from geometric nonlinearity caused by large deflection of the constituent elastic beams, leading to the snap-through behavior. This stimulated the use of a nonlinear finite element (FE) model to study such phenomena via the commercial finite element software ANSYS APDL 17.2. A criterion for the tetra-beam-plate unit cell to achieve the snap-through behavior was characterized numerically as a function of two selected geometric parameters: an inclined angle and a beam slenderness ratio. Such an approach was chosen to facilitate control of energy absorption in the presence of geometric imperfections. According to this criterion, geometric parameters of the unit cell for exhibiting such behavior were determined and employed to create lattices that can absorb energy. The lattices were then developed for FE simulations and fabricated by using the SLS method. The lattices' capability of absorbing energy was investigated both numerically and experimentally by analyzing those load-displacement relationship from cyclic loading tests. Lastly, the coefficient of restitution was adopted to quantify energy loss of the lattices due to an impact from drop tests.

7.2 Design

7.2.1 Tetra-beam-plate unit cell

The design of a tetra-beam-plate unit cell was inspired by bistability of inclined slender beams with both ends fixed, as shown in Figure 7.1. The unit cell was comprised of four inclined beams per side and four plates, and all connections were formulated as built-in one another. Each beam had a constant cross section and was initially straight. Snap-through behavior of the unit cell, resulting in energy absorption, was realized by the development of negative stiffness from the geometric nonlinearity in the unit cell due to large deflection of the constituent beams. In general, structures with negative stiffness are not stable by themselves. The present unit cell was designed to be in a stable configuration prior to application of load, and to enter the unstable negative stiffness region and the snap-through behavior upon application of sufficient load. Further, the unit cell does

not require hinges or residual stress, which can be difficult or impossible to fabricate. Geometric parameters defining the unit cell are given in this figure and as follows: namely, the diagonal distance from the center of the unit cell to its corner, r_t, the height of the plate, $2h$, the thickness of the plate, t_w, the radius of the beam, r_b, and the inclined angle, α. Note that this figure was generated to illustrate the unit cell in scale (except corners where the plates are connected to one another) by using ANSYS APDL with the ESHAPE option activated. The beams and the plates would be shown as lines and planes, respectively, in ANSYS APDL without this option. The material used for both the beams and plates was identical, and its material properties were $E = 0.717$ GPa, $\sigma_{\text{yield}} = 31.6$ MPa and $\nu = 0.24$. These values were determined by performing a tensile test for 3D-printed dumbbell-shaped test specimens made of polyamide (PA) as a parent material fabricated via selective laser sintering (SLS) method. More explanation about these values will be given later.

The finite element (FE) model representing the tetra-beam-plate unit cell is constructed as follows. For the beams, BEAM189 elements were used, while SHELL281 elements were used for the plates. The BEAM189 element is a three-dimensional quadratic three-node beam element with six degrees of freedom (DOFs) at each node consisting of translations in the x, y, and z directions and rotations about the x, y, and z directions. This element is appropriate for analyzing slender to moderately stubby/thick beam structures and is in accord with Timoshenko beam theory including shear-deformation effects. Thus, the BEAM189 is suitable for linear, large rotation, and/or large-strain nonlinear applications. The SHELL281 is a eight-node element with six DOFs at each node consisting of: translations in the x, y and z directions and rotations about the x, y and z directions. It is suitable for thin to moderately-thick shell structures, hence is applicable to evaluate linear, large rotation, and/or large strain nonlinear applications. Since the beam and shell FEs have the same nodal DOF, it is straightforward to mesh the unit cell with these elements, and there are no issues of nodal incompatibility, such as for example when flexural FEs (having six DOFs per node) and continuum FEs (having three DOFs per node) are meshed together. As illustrated in Figure 7.1, each beam has been meshed with four BEAM189 elements, whereas sixteen SHELL281 elements were used for each plate; this is sufficient to capture both post-buckling and snap-through

responses.

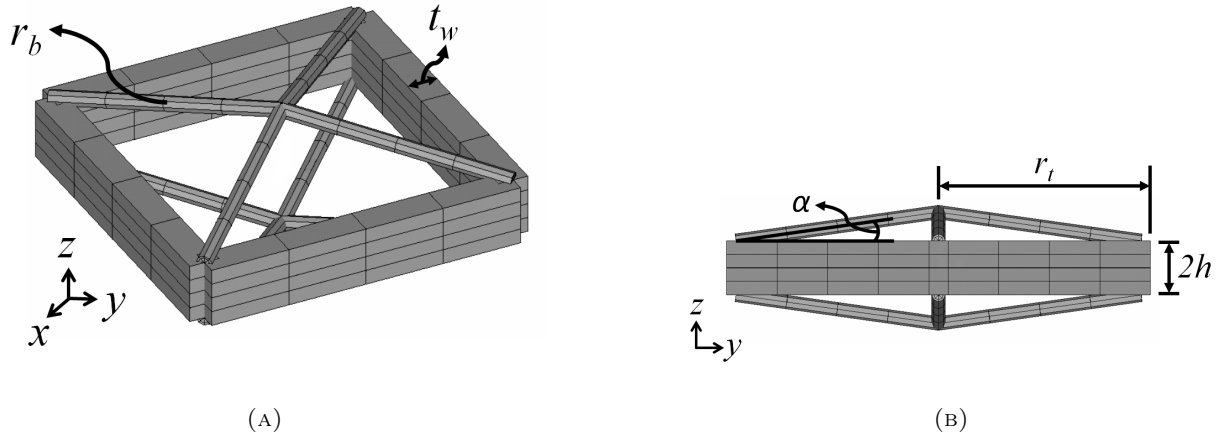

(A) (B)

FIGURE 7.1: Finite element (FE) representations of a tetra-beam-plate unit cell. (a) Isometric view. (b) Side view. Geometric parameters of the unit cell are also shown, which will be discussed later in detail. These figures are drawn in scale except corners where the plates are connected to one another.

To reveal the snap-through behavior of the tetra-beam-plate unit cell, one of its central points (where four beams merge together on the top) was subject to prescribed displacement while the opposite point on the bottom was constrained as a fixed support. These constraints allow to control displacement and automatically eliminate rigid body motions of the unit cell. The prescribed displacement, d, ranged from 0 to $p(h+\delta)$ in the $-z$ direction shown in Figure 7.1, where $\delta = r_t \tan\alpha$ and p is a multiplier that allows the prescribed displacement to achieve one of the bistable states after experiencing the snap-through behavior (i.e., a fully deformed state). This parameter depends on the inclined angle, α.

Qualitatively in an aspect of energy, while the beams deform toward the centerline of the unit cell, bending energy in these beams increases monotonically and compression energy becomes nearly its maximum at the centerline but decreases after crossing the centerline; the latter energy is similar to a sawtooth response. If such a unit cell is modeled to experience a larger decrease rate of the compression energy after passing the centerline than the rate of the increase of the bending energy, negative stiffness occurs, which is a driving factor of the snap-through behavior. Moreover, due

to this behavior, the bistable mechanism can be realized in the course of the deformation process. From its load-displacement relationship, the unit cell is expected to obtain two distinct paths from each of loading and unloading. These paths will form an area enclosed by themselves, and this is a representation of energy dissipation capability of the unit cell.

7.2.2 Energy absorption lattice

An energy absorption lattice that was analyzed, fabricated, and tested in this paper was developed by comprising multiple tetra-beam-plate unit cells. Figure 7.2 illustrates a FE representation of the lattice with the use of the ESHAPE option in ANSYS APDL. The particular lattice shown in this figure has three unit cells per side with three layers (i.e., 3×3×3 lattice).

The lattice was constructed as follows. A layer of the unit cells in the xy plane was first formulated by sharing the constituent plates with one another. This layer was then stacked in the z direction by utilizing central points of the unit cells where four beams coincide (see Figure 7.2b). Each of these points corresponds to a node in the FE model that still has 6 DOFs (translations in the x, y, and z directions and rotations about the x, y, and z directions). Prescribed displacement was applied to these nodes, and the corresponding load-displacement relationship of the lattice was analyzed to study energy loss.

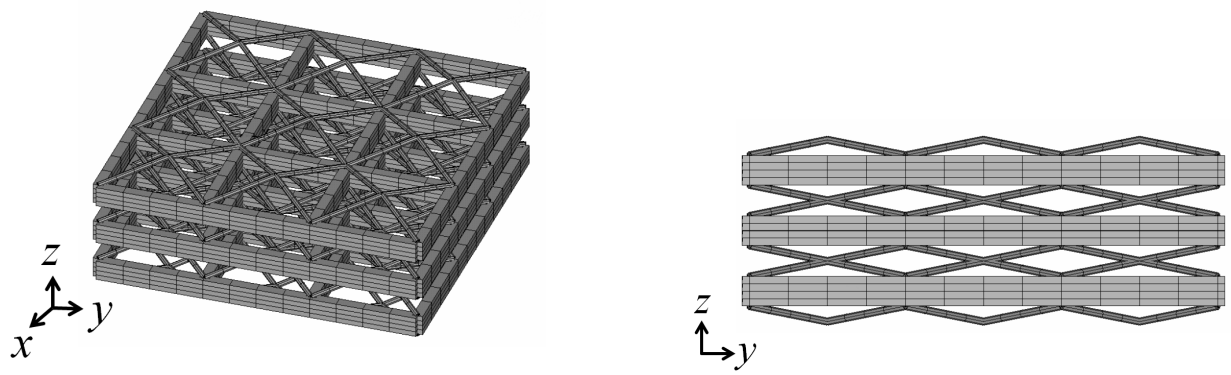

(A) (B)

FIGURE 7.2: Finite element (FE) representations of an energy absorption lattice with three cells per side and with three layers (i.e., 3×3×3 lattice). (a) Isometric view. (b) Side view.

7.3 Methods

7.3.1 Finite element simulations

To study the designed lattice consisting of multiple tetra-beam-plate unit cells, nonlinear FE models for characterizing the bistable mechanism involving both post-buckling and snap-through behavior were essential. Thus, the following solution controls in ANSYS APDL 17.2 were used; analysis type was set to static (ANTYPE,0), and large-deflection effects were enabled by activating NLGEOM (NLGEOM,1). The NLGEOM setting allows for modeling of geometric nonlinearities, stress stiffening effects, and coupling between in-plane stress and transverse stiffness, if present. The number of substeps to be taken was set to 1000 (NSUBST,1000,0,0), and automatic time stepping was turned on (AUTOTS,1). All solution data for every substep were stored to the database (OUTRES,ALL,ALL). The program's sparse direct equation solver was used for most cases along with the Newton-Raphson option when it was needed for nonlinearities. The solver continued to perform equilibrium iterations until a solution was found (i.e., until convergence criteria were satisfied). The following convergence criteria were used for all simulations: L2-norms of both force and moment (F

L2 and M L2) with a tolerance equal to 0.5 % and an infinite norm check on displacement (U INF) with a tolerance equal to 0.5 % for the displacement convergence check. The infinite norm repeats the single-DOF check at each DOF in the model, while the L2 norm performs the convergence check using the square root sum of the squares of the force (and moment) imbalance for all DOFs. The solver iterates until both the L2-norm and the infinite norm are below the selected criteria values. Once these are satisfied, it is said that the solution is within the tolerance of the correct solution and the simulation moves on to the next substep.

Applying prescribed displacement to the central point of the tetra-beam-plate unit cell induces the snap-through response due to its geometric nonlinearity. The rationale of using the prescribed displacement (i.e., displacement control) instead of prescribed load is because the complete load-displacement response can be determined, even during the negative stiffness portion of the response. The nonlinear solution provides both the corresponding load-displacement relationship at the central point of the tetra-beam-plate unit cell and the maximum equivalent stress (i.e., Von Mises stress) during the snap-through response. This information allows development of a criterion for the unit cell to exhibit the snap-through behavior in terms of the selected geometric parameters.

7.3.2 Fabrication via 3D printing

Solid models for lattices with different numbers of layers, assembled by multiple tetra-beam-plate unit cells, were developed by using the commercial CAD software SolidWorks® for the purpose of 3D printing, as shown in Figure 7.3. This figure illustrates CAD representations of the tetra-beam-plate unit cell and of the 3×3×3 lattice (i.e., a lattice structure with three cells per side and with three layers). The aim of 3D-printed lattices was to conduct laboratory experiments (i.e., cyclic loading tests and drop tests) for studying their capability of absorbing energy, which is discussed later in detail.

As illustrated in Figure 7.3b, the solid model is comprised of stalks and criss-cross structures between layers of the unit cells. The purposes of having these additional elements are to provide an adequate space between the layers during deformation, to transmit only loads to adjacent layers, and

not to undergo any appreciable deformations. Thus, they were designed as relatively rigid members compared to the constituent beams of the unit cell that governed snap-through behavior to occur, while employing the same material properties that were used for the unit cell. In contrast, the FE models (Figure 7.2) do not need these additional elements because they do not affect performance of the snap-through behavior of the designed lattices in FE simulations.

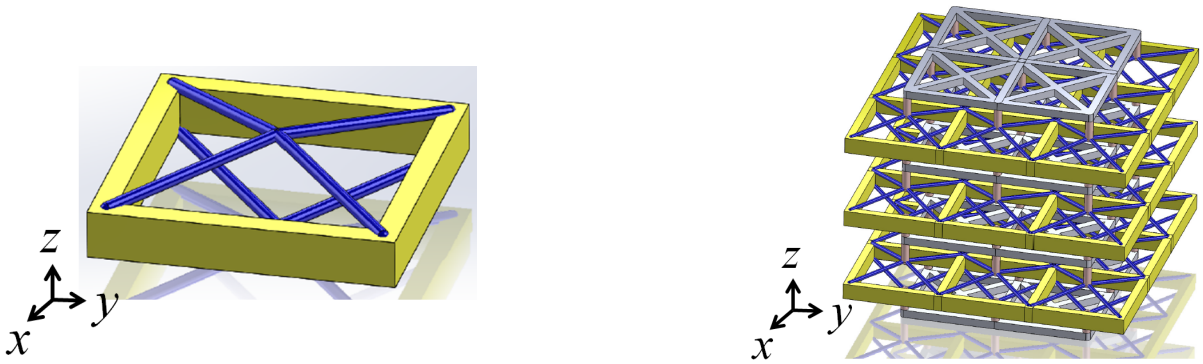

(A) (B)

FIGURE 7.3: CAD representations. (a) Tetra-beam-plate unit cell. (b) 3×3×3 lattice. The lattice is composed of the layers of the unit cells with relatively rigid stalks and criss-cross structures. These two components are to interface with the layer and they do not experience any appreciable deformations.

The lattice modeled by SolidWorks® was converted to the `STL` (STereoLithography) format for the purpose of 3D printing fabrication. Among various 3D printing (i.e., additive manufacturing) methods, a selective laser sintering (SLS), also called a laser sintering (LS), method was chosen for fabricating the lattice due to its high dimensional accuracy [146] and no need for scaffold supports. The latter aspect provides a great additional design space for designers to manufacture hollow objects or complicated structures containing porosity such as the lattices designed, fabricated, and analyzed in this paper.

The authors submitted the generated `STL` files to Midwest Prototyping [147]. A SLS-type 3D-printer used here was DTM 2500^{PLUS} providing a typical layer thickness of 0.1016 mm with a laser

diameter equal to 0.254 mm. Its tolerances are ±0.127 mm for the first 25.4 mm and ± 0.0508 mm for each additional 25.4 mm [148]. A 3D-printed 3×3×3 lattice that was fabricated by the SLS method is shown in Figure 7.4.

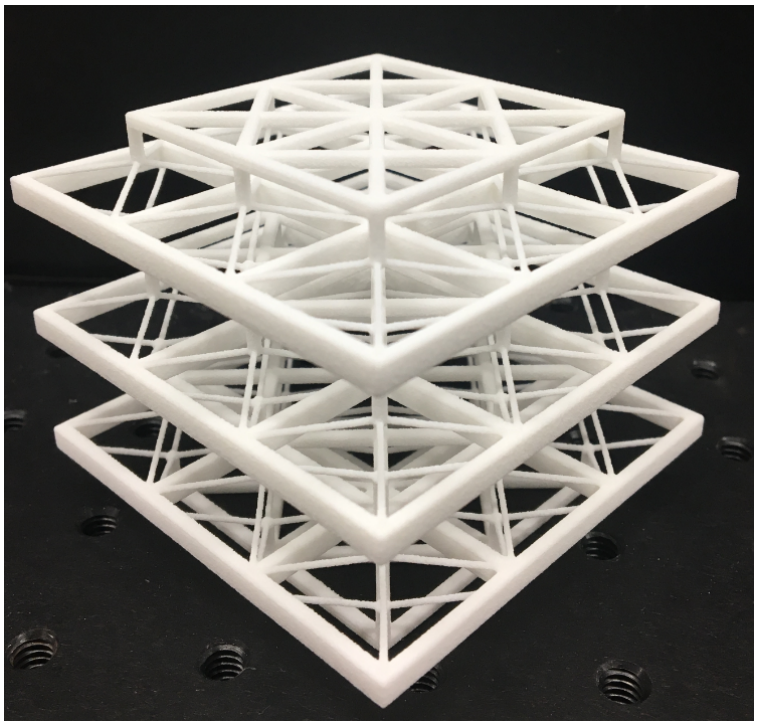

FIGURE 7.4: A photograph of a 3D-printed 3×3×3 energy absorption lattice consisting of multiple tetra-beam-plate unit cells. This lattice was fabricated by the SLS method. The parent material used for 3D printing was polyamide (PA). The lattice is about 70 mm on a side.

The parent material used to fabricate the lattice was polyamide (PA) which is a typical material for the SLS method. Recently, it was observed that material properties of 3D-printed materials are different from those of parent materials [149] [150]. This observed change of parent material properties may be due to applied high-temperature and/or high-pressure during sintering and/or solidifying process, which is necessary for current 3D printing technologies, or unintended porosity in the 3D-printed part. Thus, the authors believed that it was important to acquire accurate material properties of a 3D-printed PA before conducting any experiments.

According to ASTM D638-14 [151], we prepared several standard dumbbell-shaped test specimens fabricated from PA as a parent material via the SLS method for investigating possible changes in material properties between before and after 3D printing fabrication. Dimensions of the specimen were 19 mm × 165 mm × 2 mm. A screw-driven test frame utilizing a Sintech 10/GL load cell which has 10,000 lb capacity (calibrated on Sept. 30^{th}, 2015) was used with a constant rate of crosshead movement of 5 mm/min and data acquisition rate of 100 Hz. At room temperature, its measured material properties were $E = 0.717$ GPa, $\sigma_{\text{yield}} = 31.6$ MPa and $\sigma_{\text{ult}} = 45.3$ MPa, $\rho = 0.962$ g/cm^3. Whereas σ_{ult} was within a range of the provided value of the parent material, the elastic modulus was found to be almost half of the quoted value [152]. A yield point of the parent material was, however, not available, so a comparison was not made.

7.3.3 Experiment

Cyclic loading test

To investigate the 3D-printed lattices' capability to absorb energy, those load-displacement relationships were studied by conducting cyclic loading tests via a screw-driven test frame under displacement control at room temperature. This test frame utilizes a MTS load cell (Model #: 4501009-B) that has a load capacity of 500 N (100 lb). This load cell has a load precision of ±0.001 N and was calibrated on Apr. 15^{th}, 2016.

The cyclic loading tests were accomplished by applying loading and unloading in series to the 3D-printed lattices. This loading-unloading cycle was realized by manipulating the built-in test setups intended for compression and tensile tests, respectively, available in the provided software called TestWorks® linked to the test frame. The software as well as the provided handset allow a user to position a crosshead manually with either coarse or fine movements. For each 3D-printed lattice, a preload was utilized by moving the crosshead to load the lattices to approximately 0.2 N. A constant rate of crosshead movement was 10 mm/min and a data acquisition rate was 100 Hz. Grips were not necessary because the lattices always make contact with the load cell during both loading and unloading. Both the corresponding load and displacement carried by the lattices

were displayed and stored in real time by the software. Once the test was finished, data including these parameters was exported in the `txt` format to extract the load-displacement relationship of the lattices.

Drop test

In addition to the cyclic loading tests, drop tests were performed to determine the 3D-printed lattices' capability of absorbing energy under dynamic loading (i.e., impact). At room temperature, a steel sphere (m_{sphere} = 28.17 g and d_{sphere} = 20 mm) was dropped onto the center of the 3D-printed lattices at two different initial drop heights ($h_0 = h_{\text{low}}$ or h_{high}), and a rebound height after the impact was measured. These two different initial drop heights were chosen based on preliminary tests to introduce two distinct rebound conditions; h_{low} causes a simple rebound, and h_{high} causes an impact sufficient to give rise to snap-through behavior. This led to h_{high} being approximately a factor of two times greater than h_{low}: h_{low} = 51 mm and h_{high} = 119 mm. Note that this produced impact velocities equal to 1.00 m/s and 1.53 m/s for h_{low} and h_{high}, respectively. Thus, for a case in which the snap-through behavior occurs during the impact (i.e., a case when $h_0 = h_{\text{high}}$), the lattices are expected to produce a lower rebound height, as compared to a case when such behavior does not happen (i.e., a case when $h_0 = h_{\text{low}}$). This phenomenon represents an energy absorption due to the snap-through behavior of the lattices.

The drop tests were conducted 15 times per lattice and per initial drop height. For observations of the snap-through behavior and the rebound height due to the impact, video was recorded for each drop test by utilizing iPhone® 6s with 720 pixels of vertical resolution at 240 frames per second; this rate was superior to that of a digital camera. A thin double-sided tape was applied to the bottom of the lattice to prevent its rigid body motions after the impact; the thickness of the tape was about 0.1 mm.

Two parameters were considered to quantify energy dissipation produced by the 3D-printed lattices in response to the impact: the coefficient of restitution, e, and the ratio of the rebound height to the initial drop height, h_f/h_0. The coefficient of restitution is defined as the relation

between the post-impact (final) relative velocity and the pre-impact (initial) relative velocity of two colliding bodies. In our case, since the sphere was designed to rebound off a stationary target (i.e., the lattices), the coefficient of restitution can be simplified as follows.

$$e = \left| \frac{v_f^{\text{sphere}} - v_f^{\text{lattice}}}{v_i^{\text{lattice}} - v_i^{\text{sphere}}} \right| = \frac{v_f^{\text{sphere}}}{v_i^{\text{sphere}}} \tag{7.1}$$

where v_i denotes velocity prior to impact and v_f denotes velocity after rebound. The case when $e = 1$ represents a fully elastic collision, whereas a perfectly inelastic collision has $e = 0$. By energy conservation (neglecting air resistance), $v_i^{\text{sphere}} = \sqrt{2gh_0}$ and $v_f^{\text{sphere}} = \sqrt{2gh_f}$. By applying these to Equation 7.1, a relationship between the coefficient of restitution, e, and the ratio of the rebound height to the initial drop height, h_f/h_0, can be established as follows.

$$e = \frac{v_f^{\text{sphere}}}{v_i^{\text{sphere}}} = \frac{\sqrt{2gh_f}}{\sqrt{2gh_0}} = \sqrt{\frac{h_f}{h_0}} \tag{7.2}$$

7.4 Results and discussion

7.4.1 FE simulation

Tetra-beam-plate unit cell

For various inclined angles, α, and for several beam slenderness ratios, $r_t/2r_b$, load-displacement relationships of the tetra-beam-plate unit cells (see Figure 7.1) subjected to prescribed displacement, d, were characterized, as shown in Figure 7.5. The inclined angle was varied from 2 to 10 degrees with an increment of 1 degree, and the beam slenderness ratio equal to 5, 10, 15, 20 and 25 were considered. In this figure, displacement on the x-axis was normalized for comparison because each unit cell requires a different prescribed displacement to achieve its fully deformed state that occurs when $d/d_{\max} = 1$. Note that d_{max} represents a required prescribed displacement to give rise to the fully deformed state.

Figure 7.5 demonstrates cases only when the unit cell achieved snap-through behavior, which was revealed by a S-shaped curve in the load-displacement relationship. The unit cells with (i) beam slenderness ratio of 5 for all inclined angles, (ii) beam slenderness ratio of 10 for $\alpha = 2^\circ \sim 7^\circ$, (iii) beam slenderness ratio of 15 for $\alpha = 2^\circ \sim 5^\circ$, (iv) beam slenderness ratio of 20 for $\alpha = 2^\circ \sim 3^\circ$, and (v) beam slenderness ratio of 25 for $\alpha = 2^\circ \sim 3^\circ$ did not produce the desired snap-through behavior. Instead, the corresponding load-displacement relationships showed a monotonic increase of load with displacement. Small inclined angles do not produce a sufficient beam deflection in the unit cell, which fails to cause the constituent beams to buckle and hence does not result in negative stiffness. This indicates that such unit cells were not able to absorb energy via the snap-through behavior, thus these cases were ignored in this figure.

The maximum load magnitude was found to be inversely proportional to an increase of the beam slenderness ratio. This is due to an increase of the beam length which makes the unit cell more flexible. A range of the inclined angle that can give rise to the snap-through behavior, however, becomes larger as the beam slenderness ratio increases. In addition, a larger inclined angle produced a greater peak-to-peak load.

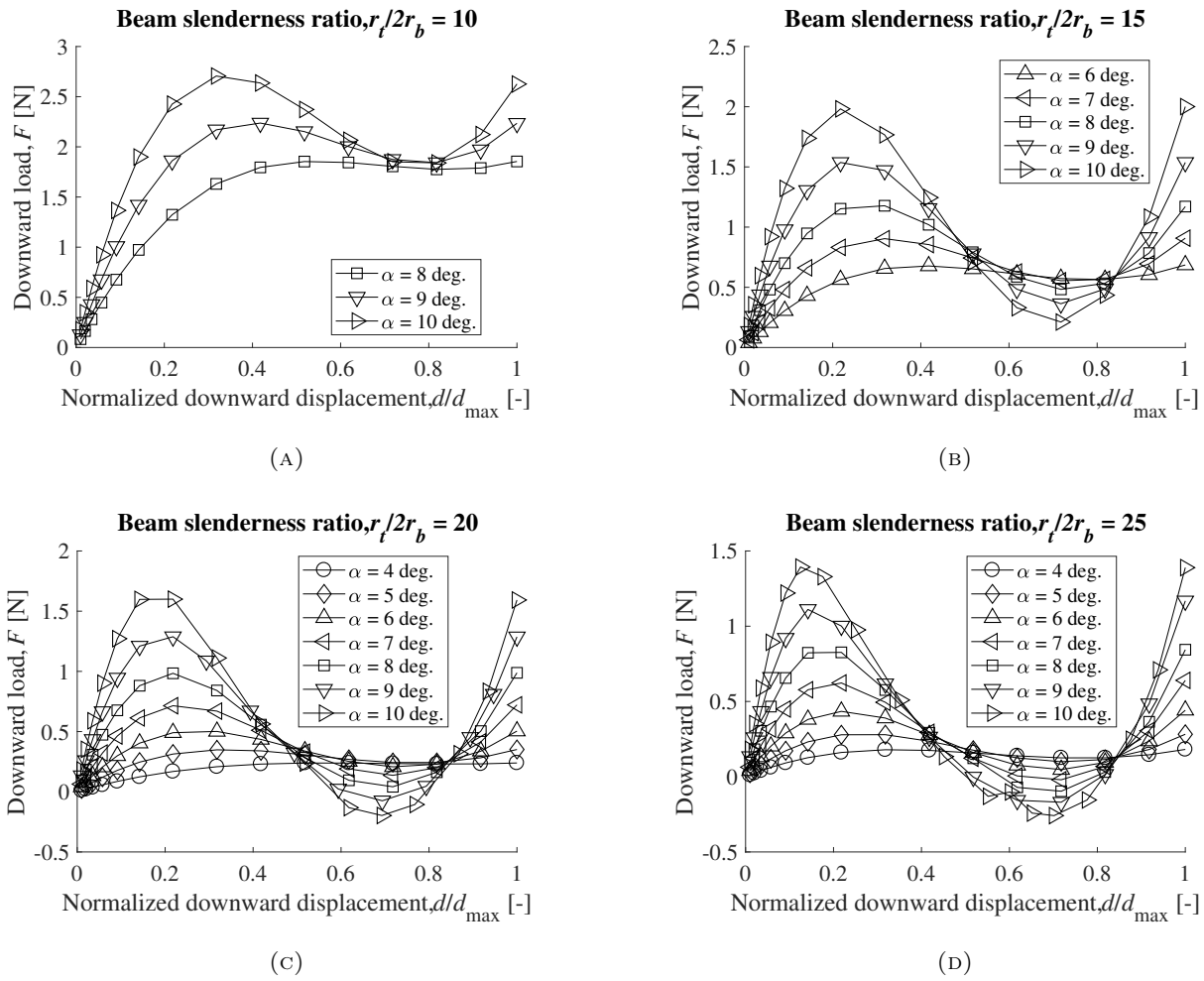

FIGURE 7.5: Numerically obtained load-displacement relationships of tetra-beam-plate unit cells for various inclined angles and for several beam slenderness ratios. The unit cells were loaded by prescribed displacement. (a) Beam slenderness ratio = 10. (b) Beam slenderness ratio = 15. (c) Beam slenderness ratio = 20. (d) Beam slenderness ratio = 25. The fully deformed unit cell occurs when $d/d_{\max} = 1$.

A criterion for achieving snap-through behavior

Numerical results of the load-displacement relationships of the tetra-beam-unit cells (see Figure 7.5), were used to produce a criterion for achieving the snap-through behavior as a function of the beam slenderness ratio, $r_t/2r_b$, and the inclined angle, α. This criterion, illustrated in Figure 7.6, is expressed by two symbols; the hollow circles indicate the unit cells without the snap-through

behavior, whereas the unit cells that can produce the snap-through behavior are denoted by the solid circles. During the snap-through process, it was seen that the maximum equivalent stress occurs when the unit cell reaches its maximum displaced position (i.e., $d/d_{max} = 1$). For a better understanding, the factor of safety, $FS = \sigma_{\text{yield}}/(\sigma_{\text{equiv}})_{\text{max}}$, was determined, which is listed next to the circles in this figure. Note that σ_{yield} was equal to 31.6 MPa that was found by performing the tensile test mentioned earlier.

As depicted in Figure 7.6, a larger inclined angle gives rise to a higher $(\sigma_{\text{equiv}})_{\text{max}}$ in the unit cell. This is mainly because the beams with a large inclined angle require more deformation to form the fully deformed unit cell, resulting in large bending energy within these beams. In contrast, $(\sigma_{\text{equiv}})_{\text{max}}$ decreases as the beam slenderness ratio increases due to a reduction of the beam deflection. Note that a lower factor of safety means larger equivalent stress.

Among geometric parameters defining the designed unit cell, the beam slenderness ratio and the inclined angle (i.e., $r_t/2r_b$ and α) are key design factors that give rise to the desired capacity of energy absorption via the snap-through behavior. Tuning these two selected parameters can also control performance of energy dissipation and further provide design freedom such as tailoring force threshold. Thus, this criterion for the newly designed structure in this study is useful as a guideline for researchers to predict whether a designed unit cell can exhibit a desired energy absorption phenomenon while ensuring the structure is in an elastic regime in which one avoids yielding.

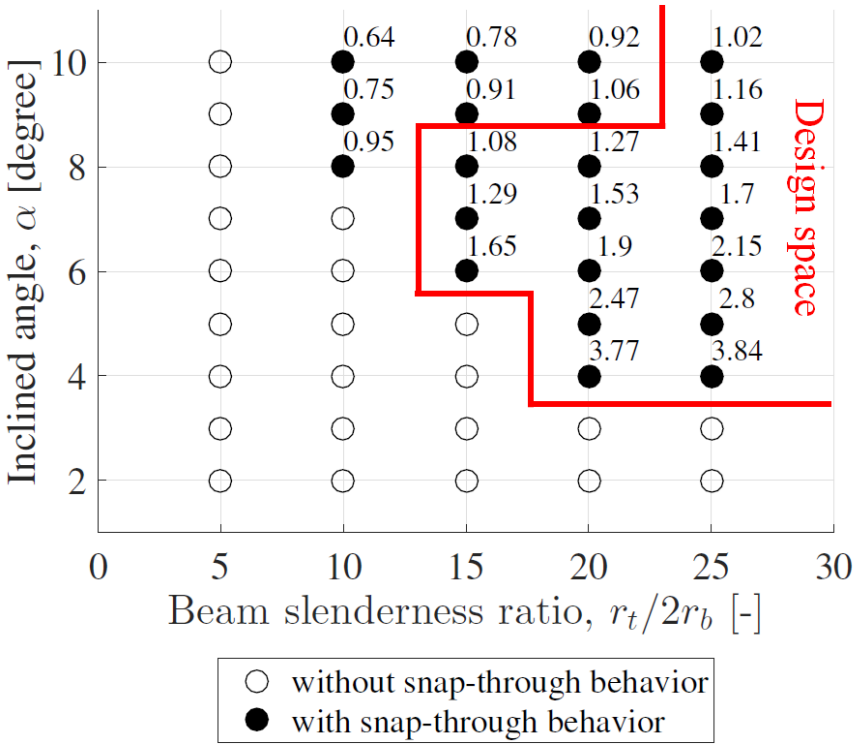

FIGURE 7.6: A numerically obtained criterion for a tetra-beam-plate unit cell to achieve snap-through behavior as a function of two selected geometric parameters. The factor of safety, based on $\sigma_{\text{yield}} = 31.55$ MPa, is shown here, and was evaluated when the unit cell was fully deformed (i.e., $d/d_{max} = 1$).

Energy absorption lattice under cyclic loading

In response to cyclic loading under displacement control, load-displacement relationships of lattices made of multiple tetra-beam-plate unit cells were obtained numerically, as given in Figure 7.7. Arrows indicate the direction of loading and unloading. According to the criterion illustrated in Figure 7.6, the selected geometric parameters of the unit cell were $r_b = 0.5$ mm, $r_t = 15$ mm, $h = 2$ mm, $t_w = 2$ mm and $\alpha = 8°$, resulting in a beam slenderness ratio of 15. These parameters were chosen by considering tolerances of the employed 3D printing method (i.e., the SLS method) in this paper and to minimize possible imperfections caused by a fabrication process of the lattices. In addition, the selected geometric parameters allowed the unit cell to avoid yielding at its fully

deformed state.

As shown in Figure 7.7, the lattices showed the snap-through behavior under the cyclic loading. As the size of the lattice increases, both the occurrence of the snap-through behavior and hysteresis (i.e., a phase lag between loading and unloading curves) become more distinct. However, for a 1×1×1 lattice (i.e., the tetra-beam-plate unit cell), these phenomena were not captured because the displacement control stabilizes the single cell through the negative stiffness region of reversed slope.

It was also observed that both the number of occurrence of the snap-through behavior and the maximum load were not dependent upon the number of the unit cells per side. Instead, the number of the snap-through occurrence increases with the number of layers of the lattices, whereas the maximum load does not vary regardless of the size of the lattice. Ideally, for each of loading and unloading, the number of the snap-through occurrence, $N_{\text{snap-through}}$, should be equal to $2N_{\text{layer}}$, where N_{layer} denotes the number of layers in the lattice.

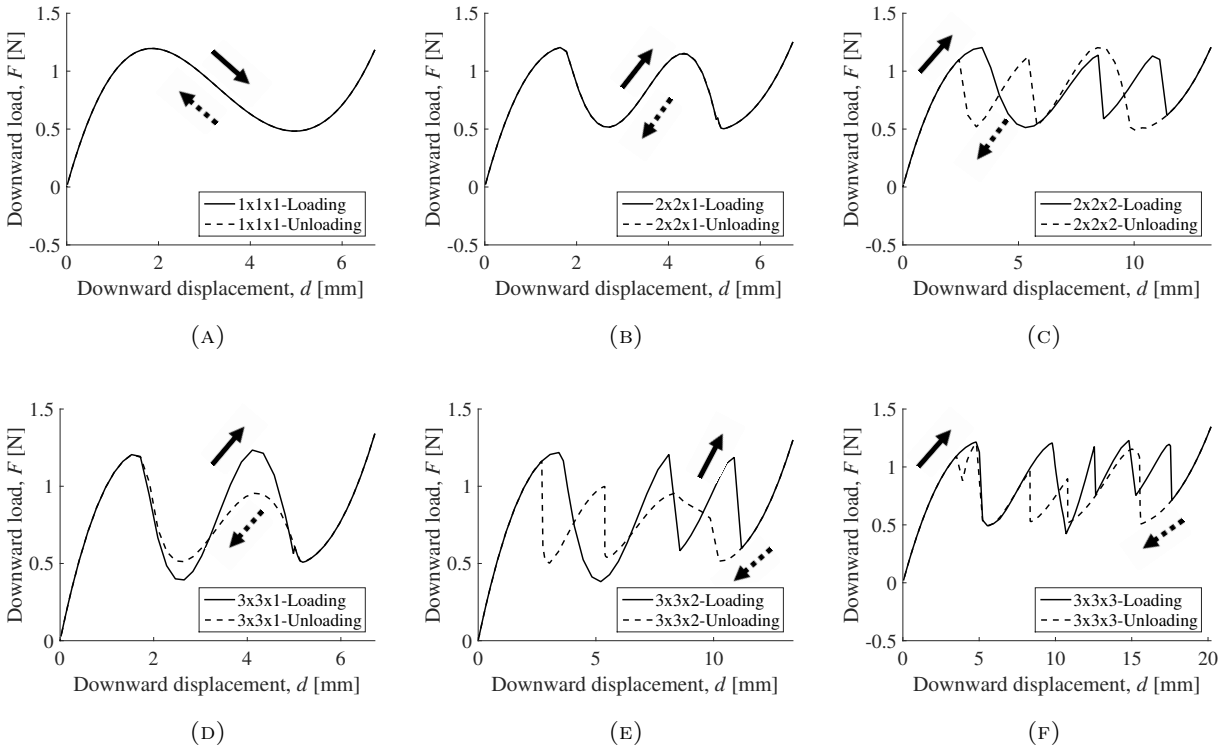

FIGURE 7.7: Numerically obtained load-displacement relationships of lattices consisting of multiple tetra-beam-plate unit cells in response to cyclic loading under displacement control. (a) 1×1×1 lattice (i.e., the unit cell). (b) 2×2×1 lattice. (c) 2×2×2 lattice. (d) 3×3×1 lattice. (e) 3×3×2 lattice. (f) 3×3×3 lattice. Arrows indicate the direction of loading and unloading. Both the occurrence of the snap-through behavior and hysteresis were observed except for the 1×1×1 lattice.

7.4.2 Experiment

Cyclic loading test

In response to cyclic loading under displacement control, load-displacement relationships of the 3×3×1, 3×3×2 and 3×3×3 lattices that were fabricated by the SLS 3D printing method were investigated experimentally, as shown in Figure 7.8. These 3D-printed lattices employ the same geometric parameters as those for the numerical models. As observed in the numerical results (shown in Figure 7.7), two distinct curves formed by each of loading and unloading (i.e., hysteresis) were also seen experimentally. This is caused by snap-through behavior due to negative stiffness of

the unit cell. The curves also form an area bounded by themselves, indicating that the lattices are capable of dissipating energy.

As illustrated in Figure 7.8, the occurrence of the snap-through behavior in the load-displacement relationships of the 3D-printed lattices was observed experimentally; such effects were also detected in the numerical results. Ideally, $N_{\text{snap-through}}$ should be equal to $2N_{\text{layer}}$ for each of loading and unloading, as stated earlier. This relationship was seen in the 3×3×1 and 3×3×2 lattices. For example, the 3×3×1 lattice exhibited the snap-through behavior twice during each of loading and unloading: one from the upper beams and the other from the lower beams of the unit cell. This, however, did not occur when the 3×3×3 lattice was unloaded (see Figure 7.8c); the snap-through behavior occurred 5 times rather than 6 times. The number of the snap-through occurrence that were observed experimentally appears to deviate from the ideal case, as the size of the lattice increases. This is because the assumed material of the lattices is perfect (i.e., flawless, non-porous, isotropic, perfectly elastic, and all cells and ribs exactly identical etc.) and because constraints such as loading condition and supports are exact (e.g., no eccentric loads or supports). Nonetheless, the load-displacement relationships of the designed lattices that were studied experimentally showed both the occurrence of the snap-through behavior and hysteresis, representing their capability of exhibiting energy absorption.

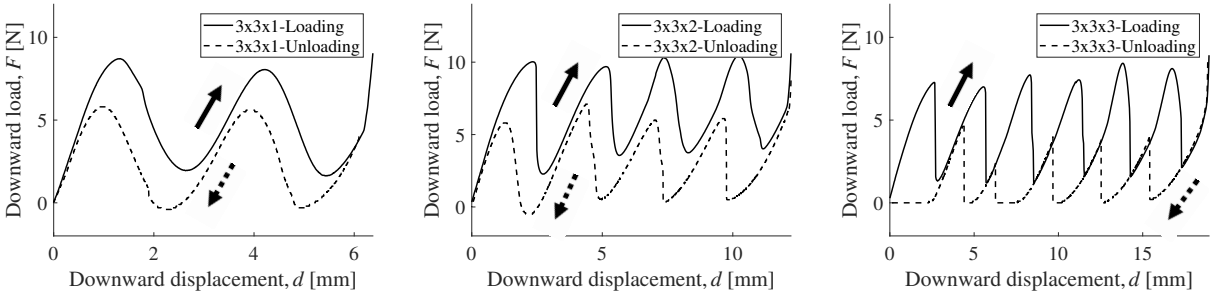

(A) (B) (C)

FIGURE 7.8: Experimentally obtained load-displacement relationships of lattices comprising multiple tetra-beam-plate unit cells in response to the cyclic loading under displacement control. (a) 3×3×1 lattice. (b) 3×3×2 lattice. (c) 3×3×3 lattice. These lattices were fabricated by the SLS method. Arrows indicate the direction of loading and unloading.

Drop test

As a result of drop tests, the coefficient of restitution, e, and the ratio of the rebound height to the initial drop height, h_f/h_0, of the 3D-printed lattices for two different initial drop heights were measured by using Equation 7.2. Table 7.1 summarizes these quantities and the corresponding standard deviation (i.e., uncertainty), σ. Figure 7.9 illustrates these quantities graphically.

When $h_0 = h_{\text{low}}$, there was no sign of snap-through behavior regardless of the number of layers in the lattices. In contrast, a case of $h_0 = h_{\text{high}}$ resulted in both a lower rebound height and snap-through behavior during the impact. Consequently, a small e was found when $h_0 = h_{\text{high}}$, as compared to e when $h_0 = h_{\text{low}}$. This finding verifies our hypothesis that the designed lattices comprising multiple tetra-beam-plate unit cells can achieve energy loss via the snap-through behavior during the impact. Moreover, the coefficient of restitution increases monotonically with N_{layer} regardless of the initial drop height.

For both the 3×3×1 and 3×3×2 lattices, a difference in the coefficient of restitution between the two cases (i.e., $h_0 = h_{\text{low}}$ and $h_0 = h_{\text{high}}$) was noticeable in contrast to that of the 3×3×3 lattice, as illustrated in Figure 7.9. For a case when $h_0 = h_{\text{high}}$, it was observed that all layers of both the 3×3×1 and 3×3×2 lattices exhibited snap-through behavior during the impact, whereas

such behavior was seen only in a single layer of the 3×3×3 lattice near the impact location. This explains a reason why the coefficient of restitution of the 3×3×3 lattice between the two cases did not produce a considerable gap similar to that which appeared for the other two lattices. A higher impact velocity would be required to activate the snap-through behavior for all layers of the 3×3×3 lattice.

TABLE 7.1: Experimentally measured coefficient of restitution, e, and the ratio of the rebound height to the initial drop height, h_f/h_0, for two different initial drop heights: h_{low} and h_{high}. The corresponding standard deviation (i.e., uncertainty), σ, values were also computed.

$h_0 = h_{\text{low}}$ (no snap-through)	3×3×1 lattice	3×3×2 lattice	3×3×3 lattice	$h_0 = h_{\text{high}}$ (snap-through observed)	3×3×1 lattice	3×3×2 lattice	3×3×3 lattice
COR, e [-]	0.6	0.61	0.64	COR, e [-]	0.54	0.55	0.62
SD, σ [-]	0.03	0.03	0.04	SD, σ [-]	0.01	0.02	0.03
h_f/h_0 [-]	0.36	0.37	0.41	h_f/h_0 [-]	0.29	0.3	0.39
SD, σ [-]	0.03	0.04	0.05	SD, σ [-]	0.01	0.02	0.04

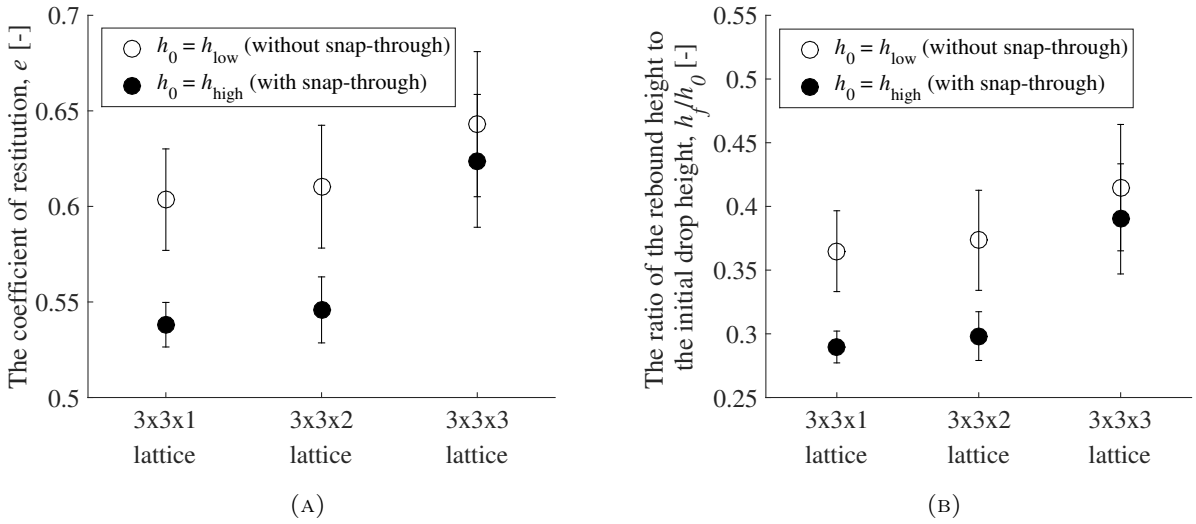

FIGURE 7.9: Results of drop tests. (a) The coefficients of restitution, e. (b) The ratio of the rebound height to the initial drop height, h_f/h_0. The impact was induced by dropping a steel sphere from two different initial drop heights (h_{low} and h_{high}) onto the 3D-printed lattices. The lattices with snap-through behavior produced lower rebound heights, indicating those lattices can exhibits enhanced energy loss.

7.4.3 Discussion

Both numerical and experimental approaches were used to determine the load-displacement behavior of the newly developed lattices consisting of tetra-beam-plate unit cells. These lattices displayed energy dissipation due to hysteresis from snap-through behavior, and multiple occurrences of this behavior depended on the number of layers of unit cells. These phenomena occur because of a bistable mechanism facilitating negative stiffness from geometric nonlinearity due to large deflection of the constituent elastic beams of the unit cell.

Although energy dissipation was successfully manifested in the lattices, the numerical and experimental cyclic loading tests showed a difference in load magnitude in the load-displacement relationships. Load magnitude measured from the experiment was approximately a factor of 6 times larger than that of the numerical analysis: $F_{\text{exp}}/F_{\text{num}} \sim 6$. This difference may be explained by several aspects as follows.

While the numerical analysis assumed the material comprising the lattices was linear elastic, the material for the 3D-printed PA via the SLS method was found to be viscoelastic. In a tensile test of the 3D-printed PA specimens that was performed in this study, the specimens produced a curved stress-strain plot, which is found in (linearly) viscoelastic materials. Moreover, considerable damping of the specimens was measured by broadband viscoelastic spectroscopy (BVS). Its tanδ was found to be 0.32 for bending and 0.30 for torsion at 1 Hz and at room temperature. Note that tanδ is an index to represent viscoelastic damping; a smaller tanδ means a lower damping. For example, at room temperature, tanδ is 5×10^{-4} at 1 Hz for steel, 10^{-3} at 1 Hz for aluminum, 0.02 at $\sim$ 1 Hz for wood and 0.1 at 1 Hz for polymethyl methacrylate (PMMA) [153]. Such large damping reduces the rebound following an impact even in the absence of the snap-through behavior. Also, tanδ varies with a frequency; the effective frequency of the impact is larger than 1 Hz. Consequently, the measured viscoelastic properties of the 3D-printed PA contributed to absorption of the impact in the drop tests and also made the observed snap-through behavior less abrupt than expected theoretically. Additionally, such viscoelastic properties can give rise to pronounced differences in load magnitude. In the cyclic loading tests that were performed in this paper, we considered only one rate of crosshead movement (this rate can be treated as a strain rate), to investigate the load-displacement relationship of the lattice. If one performs a cyclic loading test with different strain rates in the context of viscoelasticity, it is possible to probe the viscoelastic effects.

The 3D printing quality involves both unintended porosity and nonzero dimensional tolerances. Therefore the physical models differ from the numerical models. Such differences are considered to be responsible for the differences in mechanical behavior. In the numerical analysis, all constituents of the lattices were designed as solid, however unintended porosity was observed by microscopy in the 3D-printed lattices, which may have lowered load magnitude. A recent study clearly showed that mechanical properties of SLS structures can be significantly affected by a relatively high porosity at their boundaries and that such structures are greatly inhomogeneous in terms of the degree of porosity and density between layers [146]. In addition, the beam diameter of the unit cells comprising the 3D-printed lattices was not consistent; it was found that $d_{\text{beam}}^{\text{3D-printed}} = 0.8 \pm 0.02$ mm. Note

that $d_{\text{beam}}^{\text{numerical}} = 2r_b = 1$ mm. This led to $d_{\text{beam}}^{\text{3D-printed}}/d_{\text{beam}}^{\text{numerical}} \sim 0.8$. In an energy view, bending energy is one of driving factors to cause the snap-through behavior during the process of the bistable mechanism. Note that bending energy is related to bending rigidity, which is proportional to cross section radius to the 4^{th} power (i.e., r^4) for a cylindrical member. The dimensional inconsistency in the beam diameter of the 3D-printed lattice gives rise to approximately 40 % difference in bending energy, and this may have exacerbated the deviation between the numerical and experimental results. Another possible factor giving rise to the difference in load magnitude is a possibility of some plastic deformation with stress concentrations in the 3D-printed lattices as results of the 3D printing quality and viscoelastic effects.

In terms of dimensions and geometry, the beam-beam and beam-shell dimensions and intersections in the finite element (FE) models are extremely accurate replications of those in the SLS fabricated structures. In particular, in the SLS fabricated structures there are no additional geometric features at the intersections of beams and shells that would give rise to additional stiffness that the fabricated structures might have compared to the FE models. Thus, the use of beam and shell finite elements is appropriate, and these elements are ideal for the dimensions of components for which they are used. To replace the beam and/or plate elements in the FE models with solid finite elements would entail an increase in number of elements, nodes, and degrees of freedom by many orders of magnitude, and would likely render most, if not all, of the models unsolvable. Furthermore, using combinations of solid and flexural finite elements is fundamentally troublesome due to the differences in nodal degrees of freedom (solid elements have only translational degrees of freedom while flexural finite elements also have rotational degrees of freedom).

After normalizing the load and displacement plots, a comparison between the numerical and experimental results was made, as shown in Figure 7.10. It was found that normalized peaks from these two approaches occurred at almost the same location during cyclic loading. Slopes formed near both $d = 0$ and $d = d_{\max}$ were also comparable. However, normalized load magnitude still differs specifically during unloading; the magnitude from the experiments becomes zero after each snap-through.

To conclude, both the viscoelastic effects of the 3D-printed PA and fabrication variance from the SLS method may have influenced the differences between FE predictions and laboratory tests significantly. Despite these deviations, the designed lattices showed energy dissipation due to the snap-through behavior of the unit cell. This was possible because of the presence of negative stiffness due to geometric nonlinearity from large deflection of the constituent elastic beams.

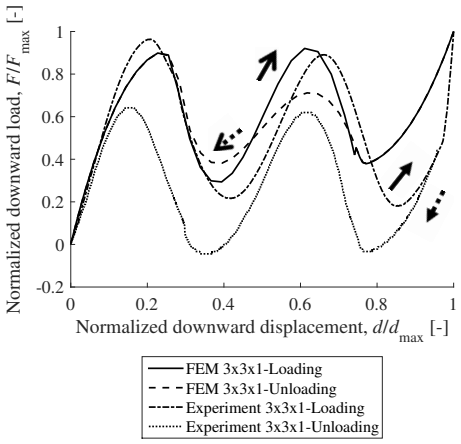

(A)

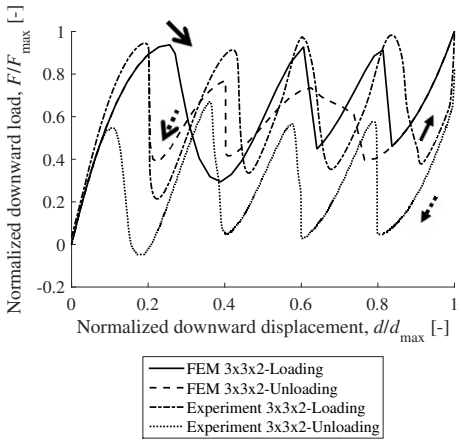

(B)

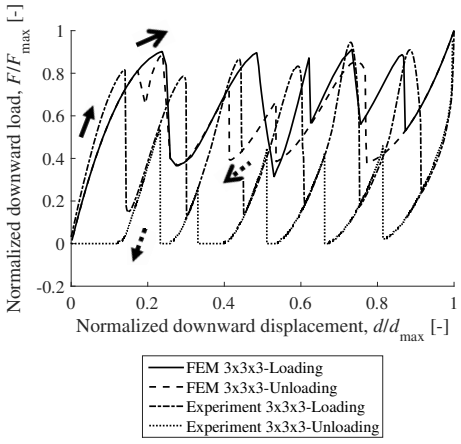

(C)

FIGURE 7.10: Comparisons of the load-displacement relationships for lattices obtained by numerical simulations and experimental testings. (a) 3×3×1 lattice. (b) 3×3×2 lattice. (c) 3×3×3 lattice. Both load and displacement were normalized. Arrows indicate the direction of loading and unloading.

7.5 Conclusions

In the present study, an energy absorption lattice consisting of multiple tetra-beam-plate unit cells

was designed, fabricated by selective laser sintering method, and analyzed numerically and experimentally. The unit cell entailed negative stiffness from the presence of geometric nonlinearity due to large deflection of the constituent beams. This caused snap-through behavior, leading to energy absorption. A criterion for the unit cell to exhibit the snap-through behavior was established as a function of the beam slenderness ratio and the inclined angle. This criterion serves as a guideline that offers to tailor performance of energy dissipation capacity and further design space such as controlling force threshold. According to this criterion, a set of geometric parameters that can give rise to such behavior was determined and adopted to create the lattices. Both numerical and experimental cyclic loading studies revealed an area enclosed by two distinct loading and unloading curves in those load-displacement relationships, indicating energy absorption capability. Energy loss of the lattices due to an impact, quantified in terms of the coefficient of restitution, was also measured by conducting drop tests. The lattices exhibiting snap-through behavior produced lower rebound heights, which demonstrates energy dissipation.

Acknowledgments

We gratefully acknowledge support of this research by the ACS Petroleum Research Foundation via Grant 52695-ND10 and by ARO U.S. Army Research Office under Grant W911NF-13-1-0484.

Chapter 8

Conclusions and future work

This dissertation consists of mainly three different, separate research topics; Chapters 2 and 3 present hierarchical structures with controllable thermal expansion, Chapters 4, 5, and 6 introduce several Cosserat structures with advanced functionalities, and Chapter 7 provide a new type of an energy absorption lattice structure. These engineered materials can possess multi-functionalities, which makes unique and beneficial themselves. Thus, they may be of considerable interest in various engineering fields such as biomedical sciences, health care, aerospace, automobile, microelectromechanical systems (MEMS), national defense, and so forth.

In Chapter 2, the feasibility of a thermoelastic triangular cell lattice composed of bi-material curved ribs connected with fixed (or bonded) joints is examined to determine if zero thermal expansion is possible. This study has practical importance since common manufacturing processes including additive manufacturing most likely require bonded (or welded) connections. Via finite element analysis (FEA) utilizing a commercial code called called ANSYS ADPL, a lattice with the bonded joints exerts significant positive thermal expansion, yet smaller in magnitude than that made of the constituent material having a higher coefficient of thermal expansion (CTE). Changes in both rib curvature and rib slenderness ratio do not influence the CTE of the lattice with the bonded joints. For achieving zero thermal expansion, a square lattice consisting of bi-material curved ribs connected with bonded joints is recommended. The rationale is as follows. Since the joint rotation of each rib is accommodated by equal rotations of neighboring ribs, there is zero moment in each

rib at each joint, although joints are bonded. This can give rise to zero net thermal expansion provided that each rib individually has zero thermal expansion subjected to temperature changes. Although the design of the square lattice is promising, further studies are needed to verify this with techniques such as experiments and numerical simulations.

By extending the idea of hierarchical structures with controllable thermal expansion in another direction, a planar chiral lattice with thermal expansion of large magnitude is presented in Chapter 3. This lattice has a Poisson's ratio approaching -1 and is inspired by the previous study [34]. Controlling thermal expansion of the lattice is achieved by employing bi-metallic rib elements and by varying geometry of the lattice. In response to temperature changes, these rib elements bend, leading to rotation of nodes and strain of the lattice. An analytical solution predicting the CTE of an individual rib element is derived by employing geometric relations and Timoshenko's beam theory. Experiments with a wide range of temperature variation provide a good agreement with the analytical solution, and the resulting CTE is found to be greater in magnitude than that of either constituent. The present lattice can also offer any desirable thermal expansion as follows. Reducing the node radius can make expansion small. If the positive axial expansion of each rib element is balanced by negative expansion from rib bending, zero expansion is possible. In addition, the designed lattice can be viewed as a Cosserat solid due to its chirality. This additional freedom associated with tunable thermal expansion may provide new design space in the context in which a large response is needed for a small input. Future research in conjunction with FEA may investigate further capabilities of the lattice.

The development and characterization of three-dimensional (3D) Cosserat structures with novel multi-functional properties are provided in Chapters 4, 5, and 6. First, a 3D chiral cubic lattice is developed in Chapter 4. This lattice is composed of multiple unit cells that can achieve stretch-twist coupling associated with chirality. Using a commercial FEA code and a customized post-processing developed in MATLAB, it is revealed that mechanical properties of the lattice are tailorable as a function of geometric parameters. With a careful adjustment, the effective Young's modulus can be maximized while Poisson's ratio is negative. Due to its stretch-twisting coupling associated with

chirality, the present lattice can be viewed as a Cosserat solid because such a coupling should be zero in the limit of a classical elastic continuum.

Chapter 5 presents a chiral 3D isotropic cubic lattice that is based on the previous study detailed in Chapter 4. Having isotropic structures offers a simpler interpretation and practical feasibility for real-life applications. A similar method to that described in the previous Chapter is employed to compute mechanical properties. An elastic relation $E = 2G(1 + \nu)$ as a measure of isotropy is utilized to design the lattice to be elastically isotropic. When the aspect ratio, defined as the ratio of the center-to-center cube spacing to the edge length of the cube, is equal to 1.64, the lattice becomes elastically isotropic. For a chiral 3D isotropic cubic lattice, an asymptotic value of Poisson's ratio is found to be approximately -0.14 by fitting the computed Poisson's ratio to a 5th degree polynomial using a least-squares best fit. Significant size effects, approaching a factor of five in torsion rigidity, are also revealed according to Cosserat elasticity. That is, such a lattice exhibits variable relative stiffness as a function of its size. This cannot be predicted by a classical theory of elasticity since a classical solid have relative stiffness equal to 1 regardless of its size. The present lattice may be of interest in the context in which the stretch-twisting coupling and tailorable mechanical properties are desirable. Future research such as experiments in conjunction with 3D printing fabrication is possible to correlate results from the present work based on FEA.

Another Cosserat structure with extreme negative Poisson's ratio, consisting of cubes connected by pivots at their corners, is presented in Chapter 6. This structure is unique in a sense that it can undergo arbitrarily large volume changes while it is compliant in tension but rigid in torsion and bending. Analytical expressions predicting strains are derived with simplifying assumptions including neglect of the effect of the tilt in the third orthogonal direction and of higher nonlinearity. To validate such expressions, a 3D numerical model representing the cube structure is developed by a commercial CAD software SolidWorks, which considers tilt in all three directions. When the tilt angles are small (i.e., in the realm of small strain), the two approaches produce a good agreement, and linear behavior is observed. In contrast, large tilt angles give rise to geometrical nonlinear effects, hence a deviation between the two approaches is observed. Such a deviation is

due to the simplifying assumptions used to derive the analytical expressions which neglect the effect of the tilt in the one of orthogonal directions. Nonetheless, for small strain, Poisson's ratio of the present structure is predicted well with a good agreement between the two approaches, and negative Poisson's ratio with large magnitude in principal directions is successfully revealed. The structure is not classically elastic because it is rigid in bending and torsion but compliant in tension and because it undergoes arbitrarily large volumetric change. Hence, it can be viewed as an extreme Cosserat solid. The present study may offer insights for future research in the context of the development of materials with unprecedented behavior beyond utilizing ideal conditions such as pivots.

The last research topic describes a 3D lattice structure capable of energy absorption, as detailed in Chapter 7. This structure is composed of multiple tetra-beam-plate unit cells made of four elastic plates and eight elastic inclined beams. This design is inspired by the concept of bistability which is often found in microelectromechanical systems (MEMS). The mechanism for achieving energy absorption employs negative stiffness facilitating snap-through behavior due to geometric nonlinearities from large deflection of the constituent beams. While objects with negative stiffness is generally considered to be instable themselves, the present structure is designed to be in a stable configuration prior to application of load, and to enter the unstable negative stiffness region. In addition, hinges or residual stress, which can be difficult or impossible to manufacture during fabrication process, are not necessary to produce snap-through response leading to energy absorption. Employing nonlinear FE models, the tetra-beam-plate unit cell is characterized in response to cyclic loading applied by prescribed displacement. A criterion for designing the unit cell to achieve the desirable snap-through behavior is developed as a function of the selected geometric parameters of the unit cell. This criterion facilitates to design a structure capable of energy absorption while ensuring it is in an elastic regime in which one avoids yielding. A set of geometric parameters is determined based on this criterion to create energy lattice structures with different sizes for nonlinear FEA and experiments utilizing physical models fabricated by using selective laser sintering (SLS) method. From load-displacement relationships in response to cyclic loading, these two approaches clearly display energy dissipation via hysteresis, yet a deviation in load magnitude is observed. This

is because the SLS method creates unexpected dimensional inconsistency and random porosity in the physical models and because a parent material used to fabricate the physical models is viscoelastic. Nonetheless, after normalizing the load-displacement curves, the resulting load magnitude from the two approaches occur almost the same location during cyclic loading, which indicates that the deviation is most likely caused by fabrication process. In addition, in a view of dynamic behavior, energy loss of the structure due to impact is quantified in terms of the coefficient of restitution. Results show that the structure can provide lower rebound heights when impact is large enough to initiate snap-through response, which demonstrates energy dissipation. The present structure can dissipate energy in one direction only. For future research, a structure capable of energy absorption in multi-directions is possible, which enhance its practicability and applicability to real-life applications.

In summary, the newly designed materials presented in this dissertation provide novel mechanical properties such as controllable thermal expansion, advanced functionalities, and energy absorption. Various approaches including theory, FEA, and experiment have been employed systematically to develop and characterize such behaviors. These engineered materials can offer access to previously unoccupied material design space that is not achievable by homogeneous material solely. Hence, their unique and tailorable mechanical properties may be beneficial to various engineering applications such as sandwich panel cores, sensors, actuators, dampers, protective devices, and so on. Moreover, the present materials may help open up new dimension for designing next-generation engineered materials with multi-functionality.

Appendix A

3D printing (additive manufacturing) resources

Abstract Available 3D printing, also called as additive manufacturing, resources both in campus and outside campus are introduced in this paper. Several categories of 3D printing process are briefly explained. The practical limitations and specifications of these different 3D printing methods and material properties used in the course of research presented in this dissertation are detailed together with printing history and comments on 3D-printed solid models developed for research.

A.1 Introduction

Additive manufacturing (AM), referred to as 3D printing nowadays, is widely used to build three dimensional (3D) physical models in manufacturing, educational, and home-use setting during the past couple of years [154] [155]. One of the most pronounced advantages of 3D printing is to allow for the manufacture of designs that could not be made through traditional manufacturing processes. 3D printing builds 3D objects by adding layer-upon-layer of bulk material(s) and has a broad range of bulk materials from polymers to metals. Due to its effectiveness and benefits, 3D printing technology is of considerable interest in various purposes such as fabricating end-use products in aircraft, dental restorations, medical implants, automobiles, and even fashion products.

In general, there are three steps for 3D printing process: modeling - printing - finishing. Each step is explained briefly as follows.

Common to this technology is the use of computer 3D modeling software (e.g. computer-aided design (CAD)), 3D printer, and layering material. Many academically and commercially available CAD software such as SolidWorks®, AutoCad®, Pro-E® are employed to create 3D printable models. There are other ways to create such models via a 3D scanner, a plain digital camera or photogrammetry software; the 3D scanner creates an electronic 3D model by digitizing real objects, which is expected to be as easy as taking a picture. 3D printable models produced by CAD software tend to result in reduced errors and can be corrected easily before printing, which provides a verification phase in the design of the object.

After 3D printable models are prepared by either CAD software or other methods, they need to be converted to a certain file format as an input to 3D printers. Commonly, a STL (STereoLithography) file format developed by 3D Systems™ is widely used. This file format is supported by many other CAD packages listed above. STL files include only the surface geometry of a three-dimensional object tessellated into multiple triangles without any representation of color, texture or other common CAD model attributes. The STL format can be represented by either ASCII or binary in which binary files are more common because they are more compact. STL files utilize a raw unstructured triangulated surface with the unit normal and vertices (defined by the right-hand rule) of the triangles using a three-dimensional Cartesian coordinate system, as shown in Figure A.1.

Various 3D printing processes are now available. The main differences between these processes are in the way layers are deposited to create parts and in the materials that are used. For example, selective laser sintering (SLS) and fused deposition modeling (FDM) melt or soften the material to produce the layers, while others cure liquid materials using different sophisticated technologies such as stereolithography (SLA). Each method has its own advantages and drawbacks. The main considerations in choosing a particular 3D printing process are generally speed, costs of the 3d-printed prototype, choice and cost of the materials, color capabilities, print resolution, and easiness

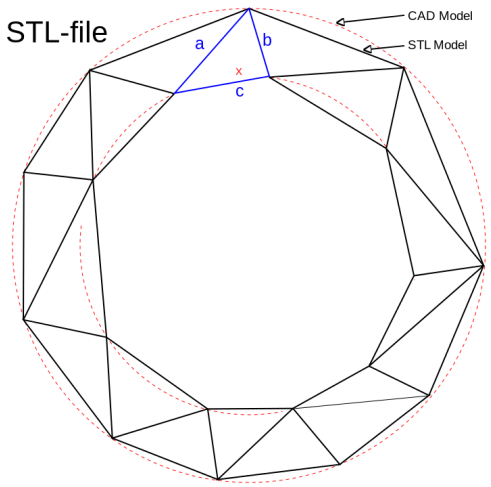

FIGURE A.1: The differences between CAD and STL models [156]. Two concentric circles are shown here highlighted as a red-dotted line. This doughnut shape illustrates a CAD model, while a series of triangles approximating this doughnut represent a STL model.

of removing support material.

In this paper, several types of 3D printers using different 3D printing methods available both in-campus and outside-campus are discussed. A brief description of these methods is provided in Section A.2. In Sections A.3 and A.4, available 3D printers in campus and outside campus are described, respectively. This paper also contains printing history and comments on 3D-printed models developed in the course of research performed in this dissertation.

A.2 3D printing (additive manufacturing) technologies

A.2.1 Fused deposition modeling (FDM)

Fused deposition modeling (FDM) technology are also known as fused filament fabrication (FFF) and fused layer modeling/manufacturing (FLM). This technology uses heat to liquefy a thermoplastic material. The thermoplastic is then extruded in a fine bead along a path set by the build file. Support structures are often necessary and can be physically broken off or dissolved once the build

is complete. *Note that there is no control over supports.* Figure A.2 illustrates how FDM works, and the process is as follows.

1. Pre-processing: Build-preparation software slices and positions a 3D CAD file and calculates a path to extrude thermoplastic and any necessary support materials.

2. Production: The FDM printer heats the thermoplastic to a semi-liquid state and deposits it in ultra-fine beads along the extrusion path. Where support or buffering is needed, the printer deposits a removable material that acts as scaffolding.

3. Post-processing: The user physically breaks away support material or dissolves it in detergent and water, and the part is ready to use.

Characteristics and restrictions

- Maximal build envelope: 914×610×914 mm^3
- Minimum feature size: 0.178 mm
- Typical tolerance: +/-0.178 mm (can be improved through post-processing)
- Minimum layer thickness: 0.178 mm

Note: These characteristics are only indicative, as there are different types of FDM printers available.

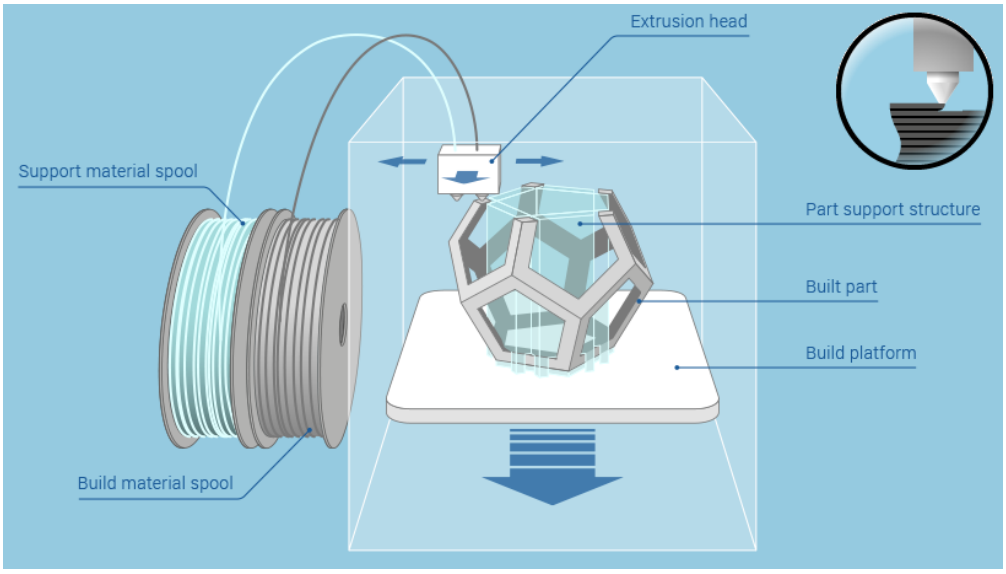

FIGURE A.2: Explanation of fused deposition modeling (FDM) [157].

A.2.2 Stereolithography (SLA)

Stereolithography (SLA), also abbreviated as SL, is a 3D printing process utilizing a controlled laser to build a 3D structure layer by layer. The process occurs in a vat of liquid photopolymer, cured upon contact with the ultraviolet laser light, as shown in Figure A.3.

Stereolithography is capable to build large parts with very good accuracy, surface finishes, and details. There is a wide range of photopolymer materials available which provide different characteristics. However, stereolithography can only handle photopolymers materials, so mechanical properties of parts are not durable or not stable over time. Further, materials are expensive and the build process is slow. It is commonly used to produce concept models, master patterns, large prototypes and investment casting patterns. *Differently from FDM method, SLA can control locations of supports manually.*

Characteristics and restrictions

- Maximal build envelope: $2100 \times 700 \times 800$ mm^3

- Minimum feature size: 0.1 mm
- Typical tolerance: +/-0.15 mm
- Minimum layer thickness: 0.016 mm

Note: These characteristics are only indicative, as there are different types of SLA printers available.

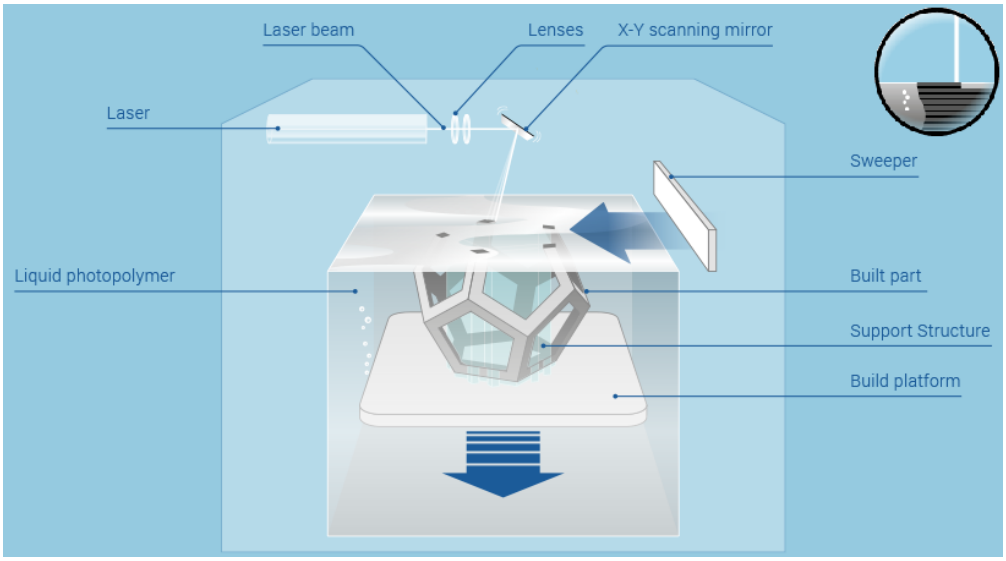

FIGURE A.3: Explanation of stereolithography (SLA) [158].

A.2.3 Selective laser sintering (SLS)

Selective laser sintering (SLS), also called laser sintering (LS), creates 3D components from powdered materials. A CO_2 laser is used to heat and fuse durable thermoplastic powders one layer at a time, creating a solid structure, as shown in Figure A.4.

SLS can fabricate parts in standard plastics with good mechanical properties. For small objects, SLS is cost competitive and often the cheapest solution. Further, SLS production parts and prototypes provide lightweight, heat and chemical resistant solutions. As for drawbacks, SLS parts do not carry over the same properties as their injection molded counterparts, especially in regards to surface finish. There is no need of support materials, which may provide additional design space to

manufacture hollow objects or complicated structure containing porosity.

Characteristics and restrictions

- Maximal build envelope: 550 × 550 × 750 mm^3
- Minimum feature size: 0.15 mm
- Typical tolerance: +/-0.25 mm (can be improved through post-processing)
- Minimum layer thickness: 0.1 mm

Note: These characteristics are only indicative, as there are different types of SLS printers available.

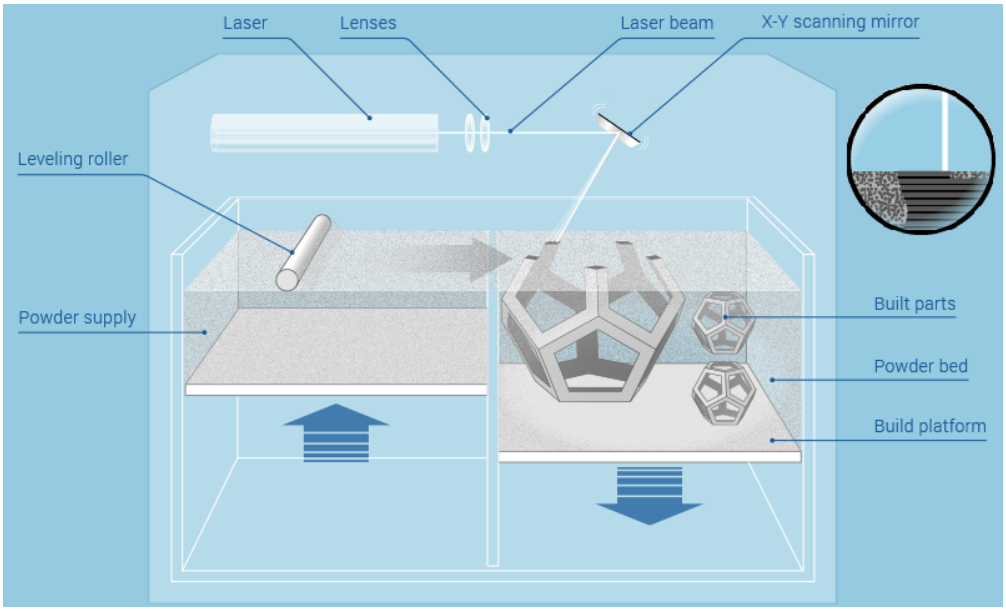

FIGURE A.4: Explanation of selective laser sintering (SLS) [159].

A.2.4 Material jetting (MJ)

Material jetting (MJ) is also known as multijet modeling, drop on demand (DOD), thermojet, and inkjet printing. This process uses inkjet print heads to jet melted wax materials onto a build platform. The material then cools and solidifies which allows to build layers on top of each other, as

shown in Figure A.5. This technology can, in a single build process, print parts and assemblies made of several materials with different mechanical and physical properties; the inkjet print head combines several resins in specific concentrations to produce a new material called as a *Digital Material* that varies in translucency, rigidity, thermal resistance and color. This enables incorporating a full range of material properties in a single print job.

MJ requires support structures for overhangs, which is usually built in a different material. This technology can also provide very good accuracy and surface finishes. However, a limited number of wax-like materials is available. Due to the type of material, parts are rather fragile, and the build process is slow. This technology is commonly used for visual, form/fit testing, medical, dental and jewelery industry. The process is as follows.

1. Pre-processing: Build-preparation software automatically calculates the placement of photopolymers and support material from a 3D CAD file.

2. Production: The MJ printer jets and instantly UV-cures tiny droplets of liquid photopolymer. Fine layers accumulate on the build tray to create one or several precise 3D models or parts. Where overhangs or complex shapes require support, the MJ printer jets a removable support material.

3. Support removal: The user easily removes the support material by hand, with water or in a solution bath. Models and parts are ready to handle and use right out of the MJ printer, with no post-curing needed.

Characteristics and restrictions

- Maximal build envelope: $300 \times 185 \times 200$ mm^3
- Minimum feature size: 0.1 mm
- Typical tolerance: +/-0.025 mm
- Minimum layer thickness: 0.013 mm

Note: These characteristics are only indicative, as there are different types of MJ printers available.

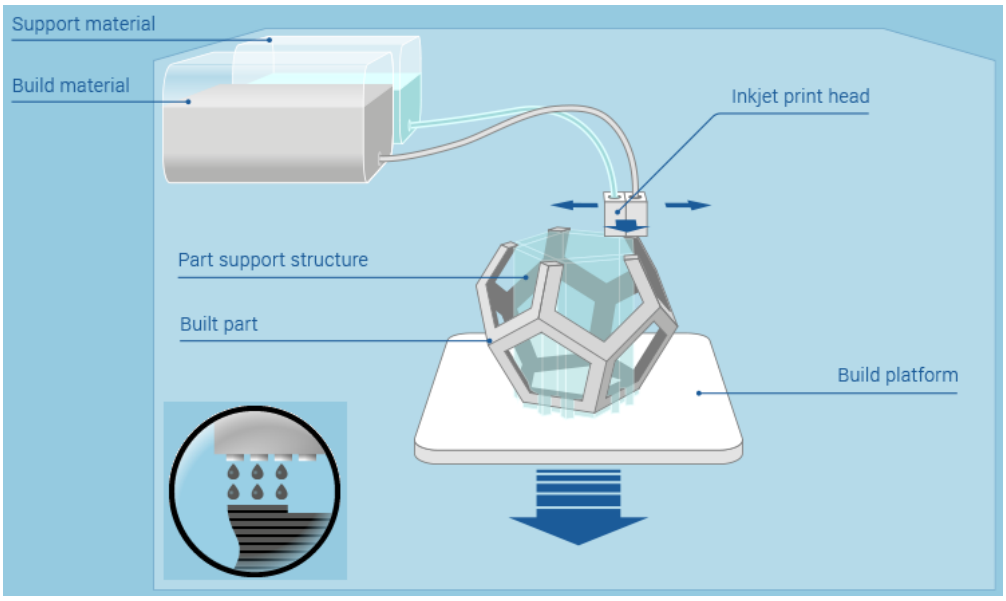

FIGURE A.5: Explanation of material jetting (MJ) [160].

A.2.5 Binder jetting (BJ)

A 3D printer performing binder jetting (BJ) distributes a layer of powder onto a build platform. Inkjet print heads which applies a liquid bonding agent glue the particles together. The build platform is then lowered and the next layer of powder is laid out on top. By repeating the process of laying out power and gluing, the parts are built up in the powder bed. A Figure A.6 illustrates the process of the BJ.

This technology does not require any support structures similar to selective laser sintering (SLS). The built parts lie in the bed of not-bonded powder. The entire build volume can therefore be filled with several parts, including stacking and pyramiding of parts. These are then all fabricated together. BJ also works with almost any material that is available in powder form.

The process is fast, simple and cheap since power particles are glued together. Colored parts is

possible by certain BJ printers along with the binding agent creating full color parts. Parts manufactured by this technology are basically particles bonded together. Thus, fabricated parts may be fragile along with limited mechanical properties if not further processed.

Characteristics and restrictions

- Maximal build envelope: $4000 \times 2000 \times 1000$ mm^3
- Minimum feature size: 0.1 mm
- Typical tolerance: +/-0.13 mm
- Minimum layer thickness: 0.09 mm
- Fast build speed
- Full color parts

Note: These characteristics are only indicative, as there are different types of BJ printers available.

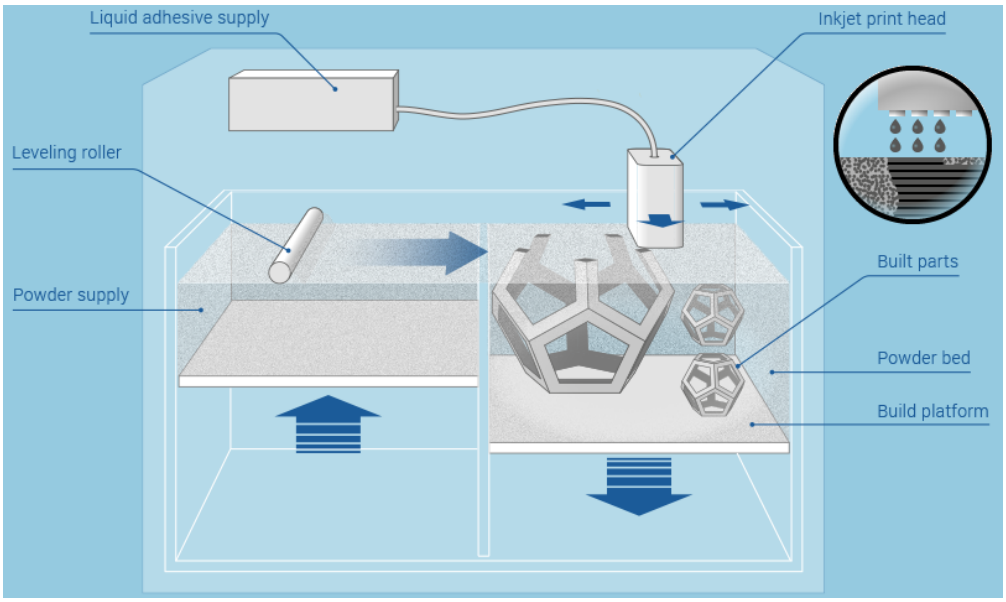

FIGURE A.6: Explanation of binder jetting (BJ) [161].

A.2.6 Laser melting (LM)

Laser melting (LM) is also known as selective laser melting (SLM), laser curing and direct metal laser sintering (DMLS). A 3D printer performing LM distributes a layer of metal powder onto a build platform, which is melted by a laser (or multiple lasers). The build platform is then lowered and the next layer of metal powder is coated on top. By recursive process of coating powder and melting where needed, the parts are built up layer by layer in the powder bed. Figure A.7 illustrates the process.

This technology requires support structures, which anchor parts and overhanging structures to the build platform. This permits the heat transfer away where the laser is melting the powder, which leads to reduction in thermal stresses and prevention against wrapping. The build volume can be filled by several parts being built in parallel as long as they are all attached to the build platform.

LS technology can fabricate parts in standard metals with high density (above 99%) and good mechanical properties similar to traditional production technologies. Parts can be further processed as any welding part. A wide range of standard metals is available. This technology is still an expensive and slow process. Although tolerances and surface finishes are limited, they can be improved through post-processing.

Characteristics and restrictions

- Maximal build envelope: $600 \times 400 \times 500$ mm^3
- Minimum feature size: $0.04 \sim 0.2$ mm
- Accuracy: +/- $0.05 \sim 0.2$ mm (+/- 0.1-0.2%)
- Minimum layer thickness: 0.03 mm
- Typical surface finish: $4 \sim 10$ microns RA
- Density: Up to 99.9%

Note: These characteristics are only indicative, as there are different types of LM printers available.

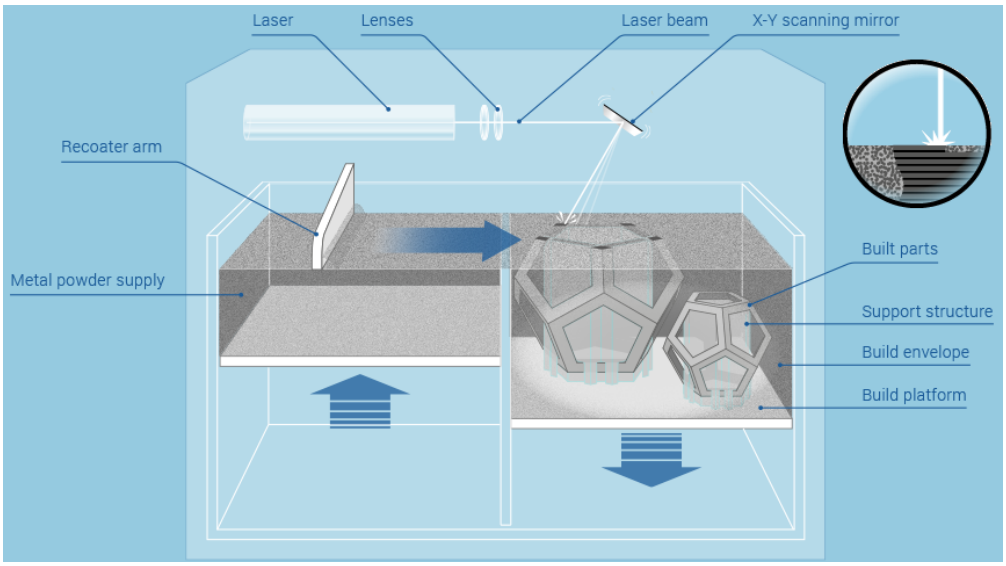

FIGURE A.7: Explanation of laser melting (LM) [162].

A.3 Campus resources

At the University of Wisconsin-Madison, 3D printing (i.e., additive manufacturing) is available in 14 different fields in 2 institutes, 4 colleges, and 2 schools at UW-Madison: TEAM Lab in College of Engineering, Polymer Engineering Center (PEC), Wisconsin Institute for Discovery (WID), Morgridge Institute for Research, Department of Art in College of Letters and Science, Department of Mechanical Engineering in College of Engineering, Department of Physics in College of Letters and Science, Department of Radiology in School of Medicine and Public Health, School of Human Ecology, College library, Department of Engineering Physics in College of Engineering and Department of Medical Physics in School of Medicine and Public Health, namely [163].

A.3.1 TEAM Lab in College of Engineering

TEAM Lab, used to be called as Student Shop, has three rapid prototyping printers: a Dimension Elite® and two RepRaps®. They all perform fused deposition modeling (FDM) with Stratasys ABSpus P430 thermoplastic [164]. Unless specified, Team Lab will print with the Dimension Elite printer with standard resolution mode.

For a cost estimate, online submission for 3D printing requests is required at their website. The following information should be included in the requests. Further contact information is as follows; phone: 608-261-1112, fax: 608-261-1111, address: Engineering Centers Building Rm. B1086, 1550 Engineering Dr. Madison, WI 53706. For more details, visit `https://teamlab.engr.wisc.edu/services/3d-printing`.

- Contact information
- Design in STL format*
- Project name
- Information about responsible faculty or principal investigator
- Course number (if applicable)

- Currently university funding number**
- Units; tell them which unit systems have used to generate STL files (e.g., inches or millimeters)

* One part per STL file. Output should be binary, not ASCII. Either inches or milimeters is okay.
** A current university funding number is needed in advance 3D printing process but not required for estimates.

Fused deposition modeling (FDM) specifications Detailed specification of the Dimension Elite 3D printer at the Team Lab can be found online [165].

- 3D printer type: Dimension Elite
- Build envelope: 8"×8"×12" (= 203×203×305 mm)
- Print resolution: ∼0.007" (= 0.178 mm) for high resolution mode and ∼0.010" (= 0.254 mm) for standard resolution mode
- Minimum size of a stand alone feature of .007" (= 0.1778 mm) and part of 0.014" (= 0.355 mm) for high resolution
- Minimum size of a stand alone feature of .010" (= 0.254 mm) and part of 0.020" (= 0.508 mm) for standard resolution
- Material: Stratasys ABSplus P430 (see Table A.1)
- Colors: Ivory, black, red, blue, nectarine, and yellow
- Printable support: Dissolvable (P400 SR)

Default settings

- Layer Resolution: 0.010"
- Model Interior: Sparse-High Density
- Support Fill: SMART
- Part orientation: Prioritize cost over quality

TABLE A.1: Mechanical properties of Stratasys ABSplus P430 [166].

Mechanical properties	Metric
Tensile strength, ultimate	33 MPa
Tensile strength, yield	31 MPa
Tensile modulus	2200 MPa
Tensile elongation at break	6 %
Tensile elongation at yield	2 %
IZOD impact, notched	106 J/m
Flexural strength	58MPa (XZ-axis); 35 MPa (ZX-axis)
Flexural modulus	2100 MPa (XZ-axis); 1650 MPa (ZX-axis)
Flexural strain at break	2 % (XZ-axis); 2 % (ZX-axis)
Coefficient of thermal expansion	8.82 x 10^{-5} mm/mm/°C
Glass transition temperature Tg	108 °C

Costs

- Model Material: $4.64 per cubic inch.
- Support Material: $4.46 per cubic inch.
- Machine Time: $3.48 per hour.
- Base: $5.00 per base.

Technical notes

- Team Lab fabricates 3D models with prioritizing cost over quality; standard resolution is used unless otherwise specified. The minimum wall thickness is available either 0.014" for high resolution mode or 0.020" for standard resolution mode. This is because FDM's extruding nozzle needs to make at least 2 passes to build a structure, hence the minimum wall thickness is twice thicker than print resolution. It is better to treat these wall thickness as the minimum dimension of a model that is planned to be designed.
- ABSplus P430 is porous and viscoelastic. In practice, since FDM requires to make 2 passes for building parts, the actual thickness is twice as a diameter of an extruding nozzle. For example, for standard resolution the minimum dimension of a part is equal to 0.508 mm.

However, a measured thickness was about 0.381 mm for the standard resolution mode. This indicates that an extruded fiber during either the first or the second pass is perhaps squeezed due to intrinsic porosity and viscoelasticity of ABSplus P430.

Printing history

- **February 09, 2016** 3D chiral isotropic lattice (5×5×5 lattice) was built. The cost of this part was $514.47, and the turnaround time was 5 days.

  Comments: Quality of this large model was sufficient for testing, as shown in Figure A.8. This model was cubical about 92 mm on a side.

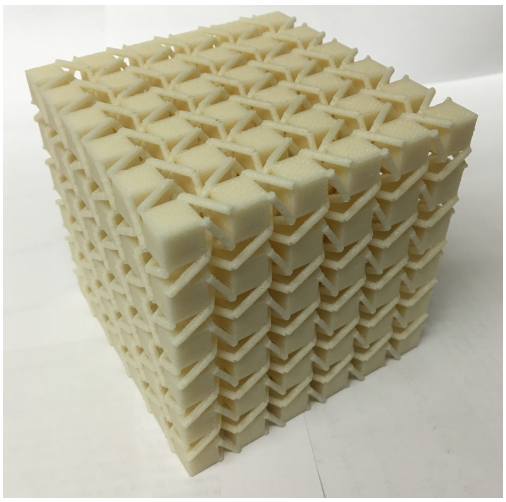

FIGURE A.8: A photograph of a 3D-printed 5×5×5 lattice with an aspect ratio of 1.642; the aspect ratio is defined to be the ratio of the center-to-center cube spacing to cube side length. The lattice is about 92 mm on a side.

- **March 30, 2016** Corrugated tubes with four different scales and 2×2×2 3D chiral isotropic lattice (4 copies) were sent to print. For both parts, the cost was $261.38. The turnaround time was 50 hours.

  Comments: The corrugated tubes were printed poorly because wall thickness was smaller than printing resolution of the FDM 3D printer, so their photographs were not taken. A 2×2×2 3D chiral isotropic lattice is cubical and 42 mm on a side, as depicted in Figure A.9.

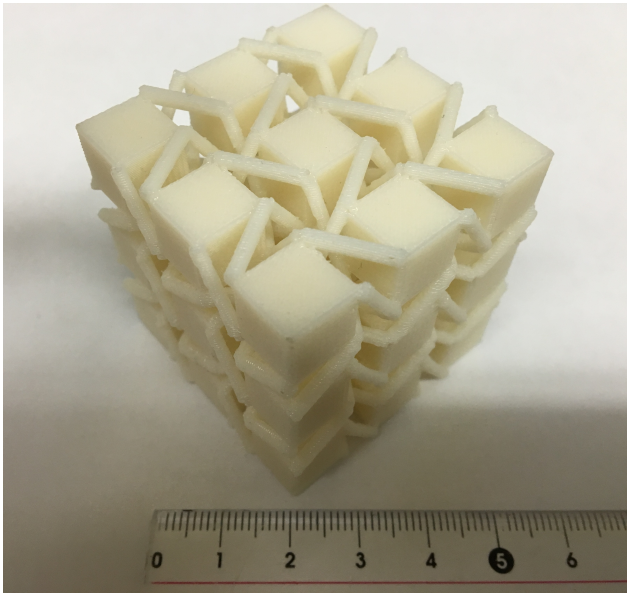

FIGURE A.9: A photograph of a 3D-printed 2×2×2 lattice with an aspect ratio of 1.642. The lattice is about 42 mm on a side.

- **April 20, 2016** Three different unit cells were printed using the standard (low) resolution mode, as shown in Figure A.10. One unit cell is printed with cylindrical corrugated tube structural elements (nicknamed as C1_rev0 shown in Figure A.10a), and a second with triangular corrugated tube elements at random orientation (nicknamed as T1_rev0 shown in Figure A.10b), and a third with triangular corrugated tube elements with three planes of symmetry (orthorhombic) (nicknamed as T2_rev0 shown in Figure A.10c). Overall dimensions of each unit cell are 8 mm on a side, and all unit cells were cubic. The cost was $37.20 for two of each model. The turnaround time was the same day when a job was requested.

  Comments: Since the dimensions of these unit cells approach to the minimum resolution of the FDM printer performing the standard resolution mode, the quality of these unit cells was unacceptable. Non-corrugated rib segments designed to be hollow were not observed; they were printed solid. In particular, the unit cells consisting of the triangular corrugated tube elements were particularly bad.

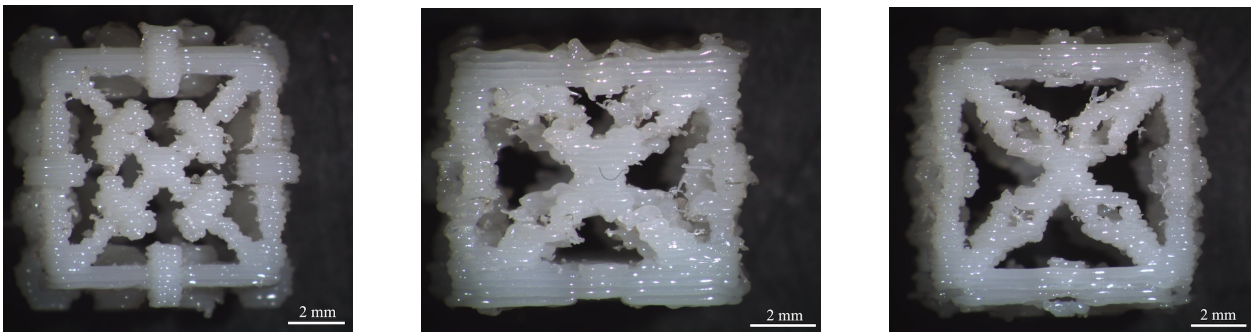

(A) (B) (C)

FIGURE A.10: Photographs taken by stereo microscope of three different unit cells printed via FDM: (a) Unit cell with cylindrical corrugated tube elements (C1_rev0). (b) Unit cell with triangular corrugated tube elements at random orientation (T1_rev0). (c) Unit cell with triangular corrugated tube elements with three planes of symmetry (T2_rev0). All unit cells are cubic and 8 mm on a side.

- **May 10, 2016** Using the standard resolution, unit cells with cylindrical corrugated tubes (C1_rev1) and with the triangular corrugated ribs with three planes of symmetry (T2_rev1) were printed, as shown in Figures A.11a and A.11b, respectively. This time, overall dimensions of these unit cells were double as compared to the unit cells shown in Figure A.10; a new parameter is 16 mm on a side. For two of each unit cell, the cost was $64.50, and the turnaround time was 1 day.

  Comments: Despite the larger dimensions, the desired slenderness was still not achieved. After dissection of the ribs, it was observed that cross sections of ribs of the unit cell with cylindrical corrugated tubes were barely hollow. In contrast, the unit cell consisting of triangular corrugated ribs showed some promise with hollowness even though the desired slenderness was not achieved.

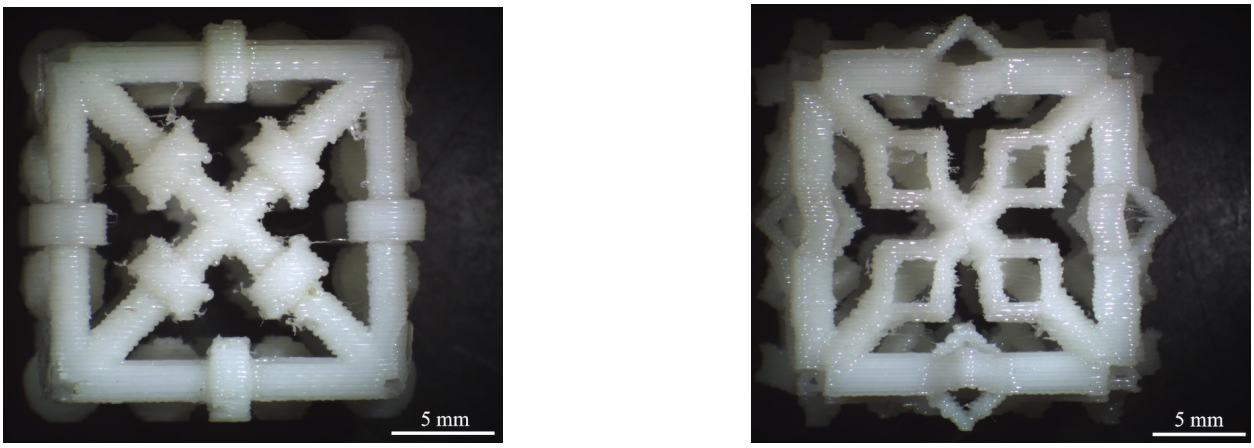

(A) (B)

FIGURE A.11: Photographs taken by stereo microscope of the unit cells printed via FDM: (a) Unit cells with cylindrical corrugated tubes (C1_rev1). (b) Unit cell with the triangular corrugated ribs with three planes of symmetry (T2_rev1). Each unit cell is 16 mm on a side.

- **July 13, 2016** Unit cell made of cylindrical corrugated tubes (C1_rev1 shown in Figure A.11a) was revised to accommodate the minimum wall thickness of FDM with the standard resolution mode as shown in Figure A.12; this new unit cell was nicknamed as C1_rev2. The wall thickness was adjusted to 0.6 mm while other dimensions were kept the same. For 2 copies, the cost: was $45.29, and the turnaround time was 1 day. Color: red.

  Comments: The fabricated models did not have the expected slenderness by looking at dissection of corrugations of ribs. The Team Lab informed this may be due to enclosing the space. Within these sections, supports materials were automatically built into these sections, which could not be physically removed or dissolved since the construction encapsulates them.

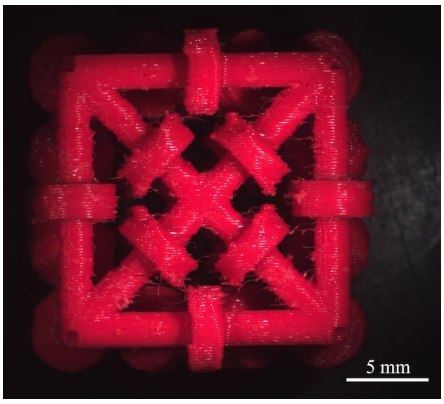

FIGURE A.12: Photographs taken by stereo microscope of unit cell made of cylindrical corrugated tubes (C1_rev2) fabricated by FDM with standard resolution mode. The wall thickness for this unit cell was 0.6mm and all other dimensions remained the same.

- **July 18, 2016** The same unit cell printed on July 13, 2016 (C1_rev2) was printed but this time with *high resolution* mode, as shown in Figure A.13. The cost was $50.88 for two copies of the part, and the turnaround time was 1 day.

  Comments: By observing dissection of corrugations of ribs, hollowness of ribs printed longitudinal direction seemed to be improved and was visible with naked eyes whereas similar hollowness as the previous printed models in the transverse direction was observed. For the ribs in the transverse direction, support materials were filled inside due to different resolutions of FDM printer in printing directions. Ribs were not sufficiently slender regardless of directions.

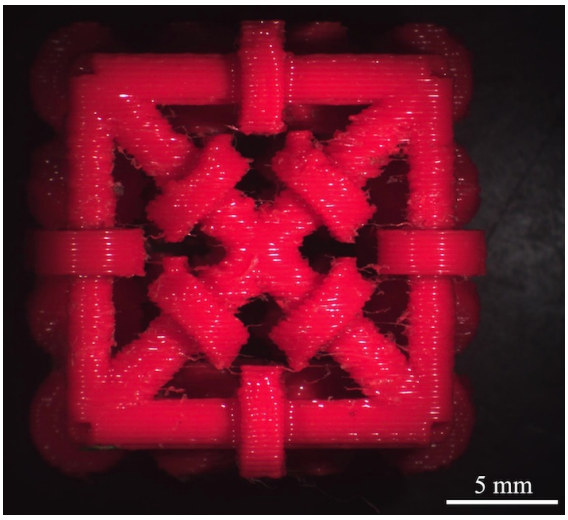

FIGURE A.13: Photographs taken by stereo microscope of unit cell made of cylindrical corrugated tubes (C1_rev2) fabricated by FDM with high resolution mode. The wall thickness for this unit cell was 0.6mm.

- **July 22, 2016** A new unit cell design consisting of square cross-section tube segments with a four fold plate element corrugation segments (S1_rev1) was printed via FDM with *high resolution* mode, as shown in Figure A.14. Since the desired slenderness was not exhibited even for high resolution mode as observed in the previous unit cells, this unit cell was scaled up to 28 mm on a side. For two copies of the part, the cost was $113.01, and the turnaround time was 1 day. The color of ABSplus P430 (parent material) was red.

  Comments: The expected slenderness was achieved however there are some printing defects. Large square holes centered in the intersection of the ribs composing the top and the bottom faces of the unit cell were created during the process. Small triangular shaped holes at each of the corners on these same faces were also present. These defects are shown clearly in Figure A.14b. After discussion with the lab manager, Charles Allhands, at Team Lab, these unexpected holes were probably generated during conversion process from 3D software file to STL format, which is necessary to print on this FDM printer. The lab manager did not know any way to re-construct the model to eliminate these holes from the conversion process.

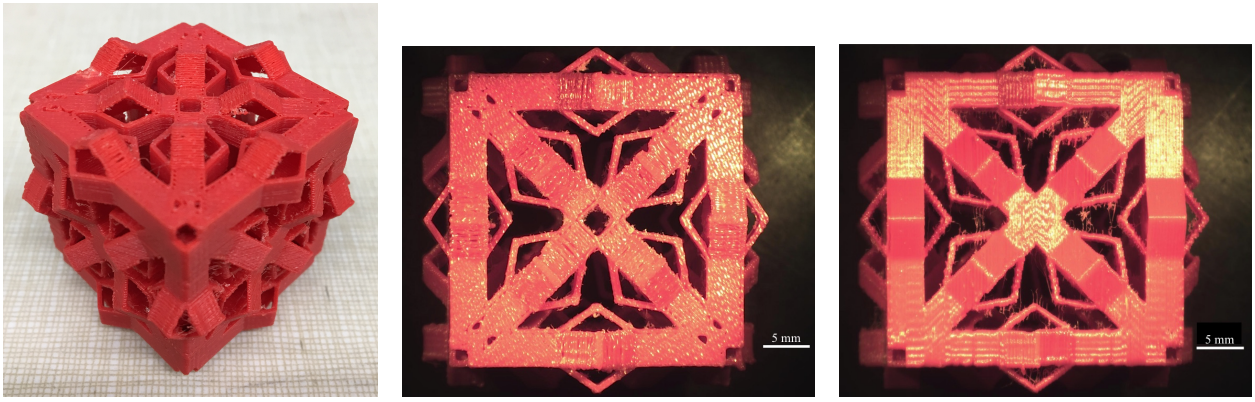

(A) (B) (C)

FIGURE A.14: Photographs taken by stereo microscope of unit cell design consisting of square cross-section tube segments with a four fold plate element corrugation segments (S1_rev1) fabricated via with high resolution mode. (a) Isometric view (b) A top (or bottom) view. (c) A side view. This unit cell is 28 mm on a side.

A.3.2 Wisconsin Institute for Discovery (WID)

Wisconsin Institute for Discovery (WID) has two different types of 3d printers: FDM and SLA. Robert Swader and George Petry are responsible for 3D printing requests. In particular, for printing via SLA, contact Robert Swader or Ben Cox. Further information can be found at `http://prototype.wisc.edu`.

Contact information

- Robert Swader
  - RSwader@morgridge.org
  - (608) 316-4706
- George Petry
  - gpetry@morgridge.org

– (608) 316-4379

Fused deposition modeling (FDM)

Specifications A FDM type 3D printer at WID is identical to the one in Team Lab; the printer is the Dimension Elite® printer made of Stratasys [167] using ABSplus thermoplastic [166].

Costs In house (university) cost: $5 per cubic inch + $5 per hour (1" height takes about 2 to 3 hours)

Stereolithography (SLA)

Specifications

- SLA printer type is unknown
- Resolution: a wall thickness is 150 micron, possibly as low as 100 microns (= ∼0.004")
- Material: Accura 60 (it is clear and is not very flexible; see Table A.2)

Table A.2: Mechanical properties of Accura 60 [168].

Mechanical properties	Metric
Tensile strength	58-68 Mpa
Tensile modulus	2.69-3.10 GPa
Elongation at break (%)	5-13 %
Flexural strength	87-101 MPa
Flexural modulus	2,700-3,000 MPa
Impact Strengh (Notched Izod)	15-25 J/m
Heat deflection temperature	53-55 °C at 455 kPa 48-50 °C at 1820 kPa
hardness, Shore D	86
Coefficient of thermal expansion	71-131 μm-°C for 0-40 °C 153 μm-°C for 75-140 °C
Glass transition (Tg)	58 °C

Costs In house (university) cost: $5 per cubic inch + $20 per hour (1" height takes about 2 to 3 hours).

Technical notes

- Support structures need to be removed after fabrication. The thickness of these support structure was similar to a diameter of non-corrugated portion of the tubes ($\sim$ 0.9 mm). Support material is the same as that of a structure.
- 3D chiral isotropic lattices (shown in Figure A.8) were said to be very difficult to make with SLA method because it would be impossible to clean out all the supports.
- For unit cells either made of cylindrical tubes or of triangular corrugated ribs with 8 mm on a side, the first copy would cost $\sim$$25, and its duplicate would cost additional $5.

Printing history

- **October 28, 2014** At 12:30 PM, Prof. Lakes, Prof. Plesha, and I took a tour to WID for SLA and FDM methods. The tour was was led by Blair Martin and Thomas Mackie who is the chair of the department that manages the 3D printers.
- **November 6, 2015** A 1×1×1 chiral unit cell was printed by both FDM and SLA. The estimated cost was $\sim$$200 for FDM and $\sim$$300 for SLA but the first printing was complimentary. The unit cell was printed for one of each printing method.
  Comments: Unit cell printed by SLA showed superior resolution than one built by FDM. Support material was hard to be taken out for both prototypes, because ribs connecting cubes were weak; only quarter of cross section of the ribs was designed to be bonded to the cubes.
- **May 3, 2016** Unit cell composed of cylindrical corrugated tubes with 8 mm on a side (C1_rev0) was printed by SLA with high resolution option. The estimated cost was $15 $\sim$ $20 per unit cell and $5 for additional duplicates. One copy was printed, and the turnaround time was 1 day.

Comments: For this unit cell, Robert Swader had about 100 supports in the model and took about 20 minutes to move them around to have no support structures inside unit cell. The thickness of the support structures was comparable to the diameter of the non-corrugated portion of ribs. Some ribs were not printed completely; the gap was generated because Robert removed the support structures near these ribs. The reason why he removed the support structures was that he won't be able to remove them without breaking the structure after printing.

- **July 13, 2016** Zach Rueger (colleague in the lab) and I had a discussion with Robert Swader about the unit cell with cylindrical corrugated tube elements (C1_rev0). Since a corrugated portion of ribs is closed structure, it is impossible to take support structures or left-over material out from inside corrugations; such a structure will be filled by liquid resin. A hole or a drain may be a feasible solution to remove the resin by either pressurized air or water, however it is still challenging to remove them completely because the unit cell is comparably small and the resin is viscous.

A.3.3 Polymer Engineering Center (PEC) in Department of Mechanical Engineering

Full descriptions are available at `http://pec.engr.wisc.edu/SLS-printing.html`.

Location

ME 1042 Laboratory, Mechanical Engineering Building, 1513 University Ave, Madison, WI 53706.

Contact information

Neil Doll; email: ndoll@wisc.edu

Selective laser sintering (SLS)

Specifications (for Nylon 12)

- 3D printer type: DTM Sinterstation 2500 Laser Sintering printer built by 3D Systems
- Materials are limited to powder form items
- Machine increments in 0.004" (= 0.1016 mm) for each new layer of powder
- Wall thickness: 0.030" (= 0.762 mm)
- tolerances: +/-0.015" (= +/-0.381 mm)
- Maximum printing volume: 14" × 12" × 12"
- Material: Nylon 12 laser sintering material (Pa650); see Table A.3

Table A.3: Mechanical properties of Nylon 12 (Pa650).

Mechanical properties	Metric
Ultimate tensile strength	48 MPa
Tensile modulus	1,700 MPa
Flexural modulus	1,500 MPa
Elongation at break (%)	24 %
IZOD impact strength (unnotched)	440 J/m
IZOD impact strength (notched)	220 J/m

Notes

- SLS method prints without support structures; no scaffolds is needed.
- Avoid thick volumes in geometry (>0.5"); shrinkage, warpage and peeling effects might be more pronounced on these.
- When designing, consider the mechanics of the process and leave space to empty non-sintered powder out of the finished part.

A.3.4 Material Science and Engineering

Contact information

Chris Kailhofer (chris.kailhofer@wisc.edu)

Fused deposition modeling

Specifications

- 3D printer type: Makerbot filament-style-printers. For more information about this printer, visit `http://www.makerbot.com/`
- Build volume: 25.2 L × 19.9 W × 15.0 H in centimeters (= 9.9 L × 7.8 W × 5.9 H in inches)
- Layer thickness: 0.1 mm (= 100 microns = 0.069 in)
- Nozzle diameter: 0.4 mm (= 0.015 in)
- Two available options for material selection.

Materials

- ABS
  - Impact (Un-notched IZOD): 5.7 ft-lb/in (std); 6.2 ft-lb/in (max)
  - Compressive Strength: 1100 psi (std); 7100 psi (max)
  - Tensile Strength: 4936 psi or 34 MPa(std); 5532 psi (max)
  - Flexural Strength: 5344 psi (std); 8646 psi (max)
- PLA (polyactic acid; polyactide)
  - Impact (Un-notched IZOD): 1.8 ft-lb/in (std); 4.1 ft-lb/in (max)
  - Compressive Strength: 2600 psi (std); 13600 psi (max)
  - Tensile Strength: 6783 psi or 47 MPa (std); 9531 psi (max)
  - Flexural Strength: 8970 psi (std); 13731 psi (max)

Costs Costs: about $50/kg (the first job is free).

Notes The Makerbot printer performing FDM had hard time to print a 2×2×2 3D chiral isotropic lattice; nozzles continue to malfunction. A 2×2×2 3D chiral isotropic lattice 3D-printed by PLA was lighter than one fabricated by Team Lab and printing resolution seems to be comparable, as given in Figure A.15.

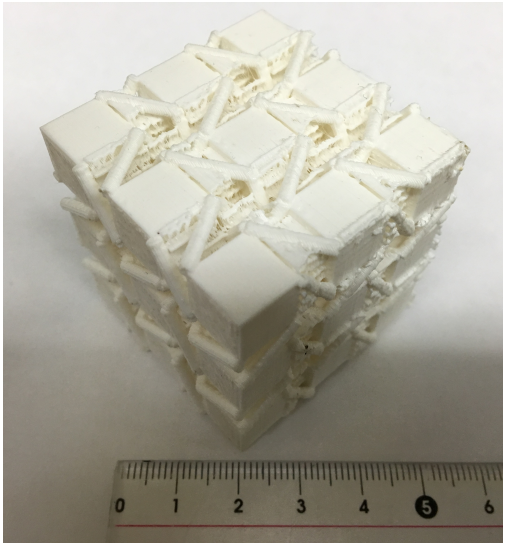

FIGURE A.15: A photograph of a 3D-printed 2×2×2 lattice with an aspect ratio of 1.642 which was printed via Makerbot with PLA material. This is an identical structure to one shown in Figure A.9.

A.4 Commercial resources

This section contains several commercial resources for 3D printing. They are usually expensive to fabricate models compared to those at the university. However, various 3D printing technologies including material jetting (MJ) and binder jetting (BJ) are available, which provides superior print resolutions compared to FDM method. In addition, a wide range of bulk materials from flexible materials like elastomer to powdered materials such as steel powder is available.

A.4.1 Midwest Prototyping

Midwest Prototyping is a local company near Madison, WI. It takes about 40 minute drive from Engineering Research Building, 1500 Engineering Drive in Madison. This company provides the best quality and a quick turnaround time by far. Staffs are also kind and willing to help. (Zach and I had a tour on May 26, 2016 at 1PM). STL files need to be submitted online via company's website (`https://www.midwestproto.com/ftp-upload`). Usual turnaround is less than 3-4 business days. Parts are shipped via UPS ground.

Location

Address: 10949 Blackhawk Dr. Blue Mounds, WI 53517.

Website: `https://www.midwestproto.com`

Contact information

- Mike Roosa (Business & Application development)
  - mike.roosa@midwestproto.com
  - Office: 608-437-1400
  - Cell: 608-445-9266

  - Fax: 608-437-1409

- Alfredo Jijon (Prototype specialist)

  - alfredo@midwestproto.com
  - Office: 608-437-1400
  - Fax: 608-437-1409

- Laura Mason (Project manager)

  - laura.mason@midwestproto.com
  - Office: 608-437-1400
  - Fax: 608-437-1409

Available 3D printers

The company possesses various types of 3D printers that perform different AM technologies as follows.

- Stereolithography (SLA)
- Selective laser sintering (SLS)
- Fused deposition modeling (FDM)
- Material jetting via Polyjet/Objet
- Binder jetting via Z-Corp
- Continuous liquid interface production (CLIP)

Cast urethane services and CNC machining are also available. The following sections include specifications as well as bulk material properties for 3D printing methods that are listed above. For more details, visit `https://www.midwestproto.com`

Stereolithography (SLA) A 3D printer performing SLA is suitable for highly accurate components for use in design verification and presentation models. A variety of materials that simulate many common thermoplastics is available. Such materials can provide great finishing, clearness and high toughness. Further, they can be used for high heat and fluid applications.

Specifications

- 3D printer type: iPro 8000 (See Table A.4 for build specifications).
- Tolerances: +/- 0.005" (= +/- 0.127 mm) for the first inch and +/- 0.0015" (= +/- 0.0381 mm) for each additional inch.
- Available bulk materials: Accura® 25, Accura® 60, Accura® Xtreme, Accura® Xtreme White 200, Accura® Bluestone, Somos® 8120, Somos® PerFORM (See Table A.5 for bulk material properties).

Table A.4: SLA build specifications [169].

Build Envelope [mm]								
X	Y	Z	Accura® 25	Accura® 60	Accura® Xtreme	Accura® XtremeWhite 200	Accura® Bluestone	Somos 8120
635	736.6	533.4	X	X		X		
508	508	609.6	X		X	X	X	
254	254	254	X	X	X	X		X
127	127	254	HR	HR	HR	HR		HR

HR: Designates High Resolution, available only on the 127 mm × 127 mm × 254 mm build envelope

TABLE A.5: Available bulk materials and material properties for SLA [170].

	Accura 25	Accura 60	Accura Xtreme	Accura Xtreme White 200	Accura Bluestone	Somos 8120	Somos PerFORM
Appearance	Off-white	Clear	Grey	White	Opaque blue	Semi-transparent	White
Notable for	- Durability - Master patterns - Functional prototypes	- Clarity and transparency - Visualization models - Stiffness	- Durability - Functional prototypes - Impact resistance	- Durability - Break resistance - Detail fidelity	- Exceptional stiffness - High humidity resistance - High temp resistance	- Flexibility - Snap-fits - Impact strength	- Exceptional stiffness - High humidity resistance - High temp resistance
Simulates or comparable to	Polypropylene	Polycarbonate	ABS Polypropylene	ABS	Ceramic	Polyethylene	Ceramic
Tensile Ultimate Strength (ASTM D648)	38 MPa	58-68 MPa	38-44 MPa	45-50 MPa	66-68 MPa	26 MPa	68 MPa
Tensile Modulus (ASTM D648)	1.59-1.66 GPa	2.67-3.10 GPa	1.79-1.98 GPa	2.30-2.63 GPa	7.60-11.7 GPa	276-703 MPa	10.5 GPa
Elongation at break, ϵ_{break}	0.13-0.20	0.05-0.13	0.14-0.22	0.07-0.20	0.014-0.024	0.27	0.011
Flexural Ultimate Strength (ASTM D790)	55-58 MPa	87-101 MPa	52-71 MPa	75-79 MPa	127-154 MPa	26 MPa	120 MPa
Flexural Modulus (ASTM D790)	1.38-1.66 GPa	2.70-3.00 GPa	1.52-2.07 GPa	2.35-2.55 GPa	8.3-9.8 GPa	0.69 GPa	10 GPa
Impact Strength (IZOD) (ASTM D256)	19-24 J/m	15-25 J/m	35-52 J/m	55-66 J/m	13-17 J/m	59 J/m	17 J/m
Heat Deflection Temperature at 0.45 MPa (ASTM D648)	58-63 °C	53-55 °C	62 °C	47 °C	65-66°C	54 °C	132 °C

Selective laser sintering (SLS) The SLS-type 3D printer has been employed to fabricate a variety of parts used in agricultural environments, off road vehicles, functional parts in lab equipment, race cars and aircrafts. The final components are thus ideal for use in harsh environments and demanding applications. For build specification of the SLS-type 3D printer, please see Table A.6.

Table A.6: SLS build specifications [148].

Printer	Build Envelope [mm]			Typical Layer	Available Powders		
	X	Y	Z	Thickness [mm]	PA	GF	Alulon
DTM 2500^{PLUS}	381	330.5	457.2	0.1016	X	X	X
sPro 60 HS-HD	381	330.2	457.2	0.1016	X	X	X
EOS P760	711.2	381	584.2	0.1016	X		

Specifications

- 3D printer type: unknown
- Available powders: Polyamide (also called as PA, base nylon or nylon 12), glass filled (GF), Alulon (blend of nylon and aluminum powder) (See Table A.7 for bulk material properties).
- Tolerances: +/- .005" for the first inch and +/- .002" for each additional inch.
- Typical layer thickness: 0.004" (= 0.1016 mm)
- Laser diameter: 0.01" (= 0.254 mm)

TABLE A.7: Available bulk materials and material properties for SLS [171].

	Polyamide (PA)	Glass Filled (GF)	Alulon
Appearance	White	Light grey	Metallic grey
Notable for	- Good chemical resistance - USP Class VI complaint - Low moisture absorption	- Temperature resistance - Functional parts - Structural integrity	- Functional parts - Structural integrity - Feels like aluminum - Good machinability
Simulates or comparable to	Nylon 12	30% glass-filled nylon	Blend of nylon and aluminum powder
Tensile Ultimate Modulus (ASTM D638)	43 MPa	26 MPa	39.2 MPa
Tensile Modulus (ASTM D638)	1.59 GPa	4.07 GPa	3 GPa
Elongation at break, ϵ_{break}	0.14	0.014	0.025
Flexural Ultimate Strength (ASTM D790)	48 MPa	37 MPa	n/a
Flexural Modulus (ASTM D790)	1.39 GPa	3.11 GPa	n/a
Impact Strength (IZOD) (ASTM D256)	32 J/m	41 J/m	n/a
Heat Deflection Temperature at 0.45 MPa (ASTM D648)	180 °C	179 °C	175 °C

Notes

- The most popular material is the base nylon (PA), a bright white strong and flexible material. It can be drilled and tapped easily and will accept thread forming screws and heat staked inserts.

Printing history

- **July 20, 2016** Unit cell consisting of cylindrical corrugated tubes C1_rev3 (Figure A.16a) and one made of triangular corrugated ribs with three fold plate elements T2_rev1 (Figure A.16b) were fabricated with finish level one which included removal of excess powder and light bead blasting. Overall dimensions of both unit cells were 16 mm on a side. For either unit

cell, the desired slenderness was achieved and no dimensional distortion was observed. These unit cells were sent to print on July 20, 2016, and the turnaround time was 6 days (received on July 26, 2016). One copy of each unit cell was printed, and the cost was $35. Materials used to fabricate was PA 2200.

Comments: These were by far the highest quality models of all printing methods. Expected slenderness was achieved and hollowness was observed. Deformation of unit cell T2_rev1 was visible by naked eyes.

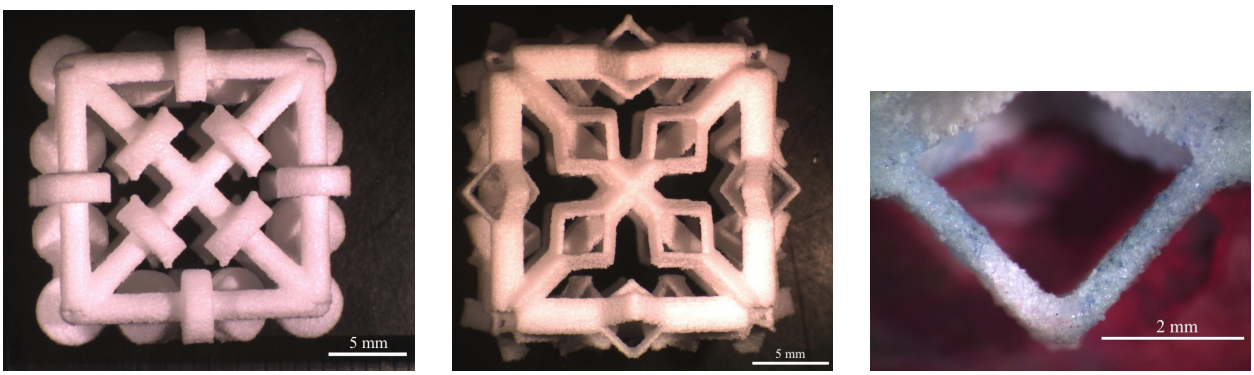

(A) (B) (C)

FIGURE A.16: Photographs taken by stereo microscope. (a) Unit cell consisting of cylindrical corrugated ribs (C1_rev3). (b) Unit cell made of triangular ribs with three fold plate elements (T2_rev1). (c) A closed up view of the triangular rib of unit cell T2_rev1. Size of both unit cells are 16 mm on a side.

- **August 29, 2016** - Two unit cells with different lattice parameters were submitted to 3d-printed. One of which had a side length of 14 mm (S1_rev2) as shown in Figure A.17 and the other that had a side length of 8 mm (S1_rev3) as shown Figure A.18. Both of these unit cells were composed of square ribs with four fold plate element corrugations. Polyamide (nylon 12) was used as a parent material, and finish level 1 was employed. Three copies of each unit cell were printed for $48 and were arrived in the lab on September 1, 2016.

  Comments: Both received models had evident defects in their structures. The plate elements in the corrugations for both unit cells , which were parallel to the top and the bottom faces,

were all incomplete, as shown in Figures A.17b and A.18b. This was caused by their need to be self supported during the printing process, which they were not because of their orientation. All of plate elements would be supported during the printing process and would result in a successful part, if they were rotated by 45°. In addition, for the unit cell of 8 mm side length (S1_rev3), ribs were not 3d-printed with an acceptable resolution. The plate elements were nearly indistinguishable because the size of this unit cell was too small for the practical capabilities of the SLS printer. In despite of aforementioned printing defects, the unit cell with 14 mm side length (S1_rev2) were of acceptable resolution.

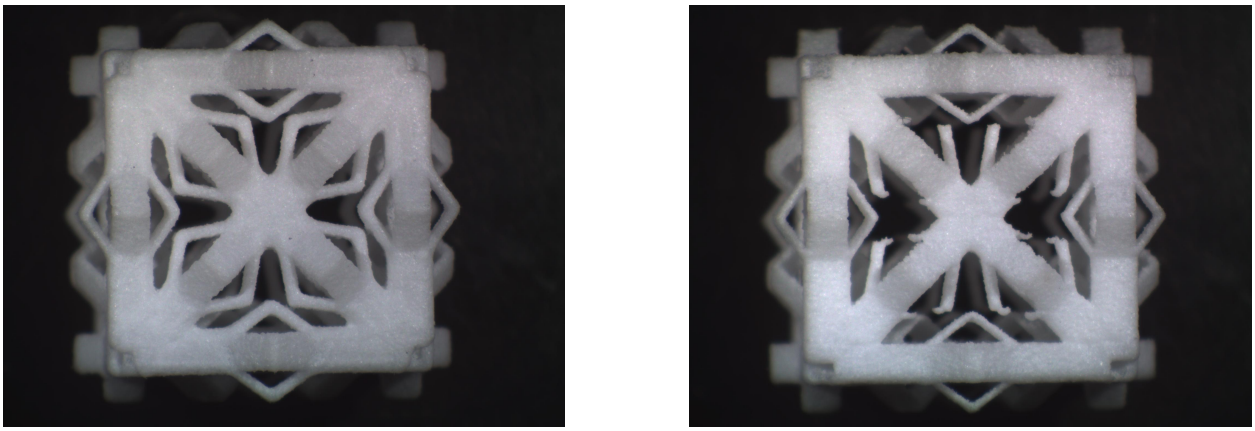

(A) (B)

FIGURE A.17: Photographs taken by stereo microscope of the unit cell consisting of square ribs with four fold plate elements corrugation (S1_rev2). Overall dimensions were 14 mm on a side. (a) Top (or bottom) surface and (b) Side surface.

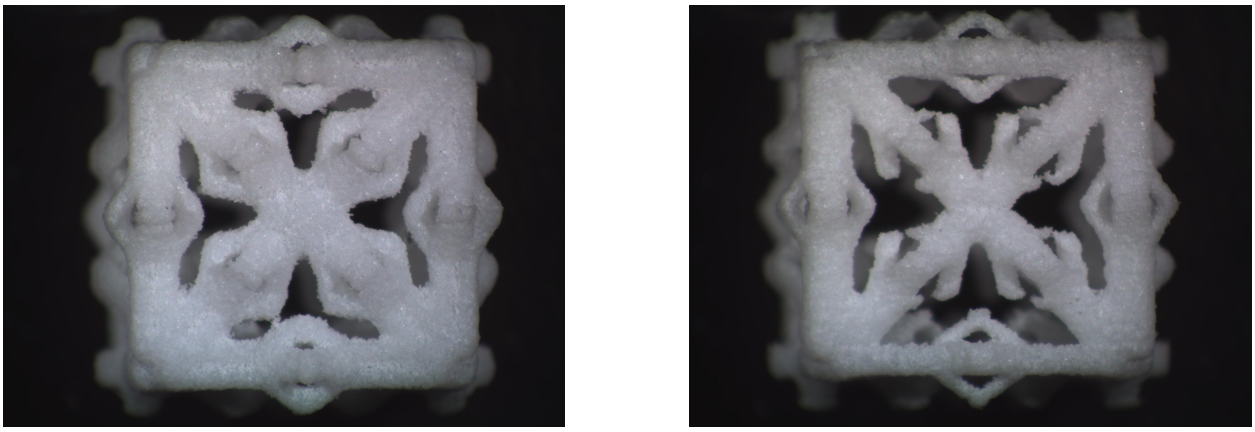

(A) (B)

FIGURE A.18: Photographs taken by stereo microscope of the unit cell consisting of square ribs with four fold plate elements corrugation (S1_rev3). Overall dimensions were 8 mm on a side (a) Top (or bottom) surface and (b) Side surface.

- **September 6, 2016** - A revised unit cell with square ribs and four fold plate element corrugations rotated 45° about their longitudinal axes (S1_rev4) as compared to S1_rev3 shown in Figure A.18 were 3d-printed. This unit cell shares the same ribs with S1_rev3, thus its overall dimension is 14 mm on a side. Three copies of each unit cell was fabricated with finish level 1 for $48 and was arrived in the lab on Sep. 14, 2016. Polyamide (nylon 12) was used as a parent material.

  Comments: As shown in Figure A.19, the corrugated segments were all totally complete. No printing defects were observed, and the expected slenderness was achieved.

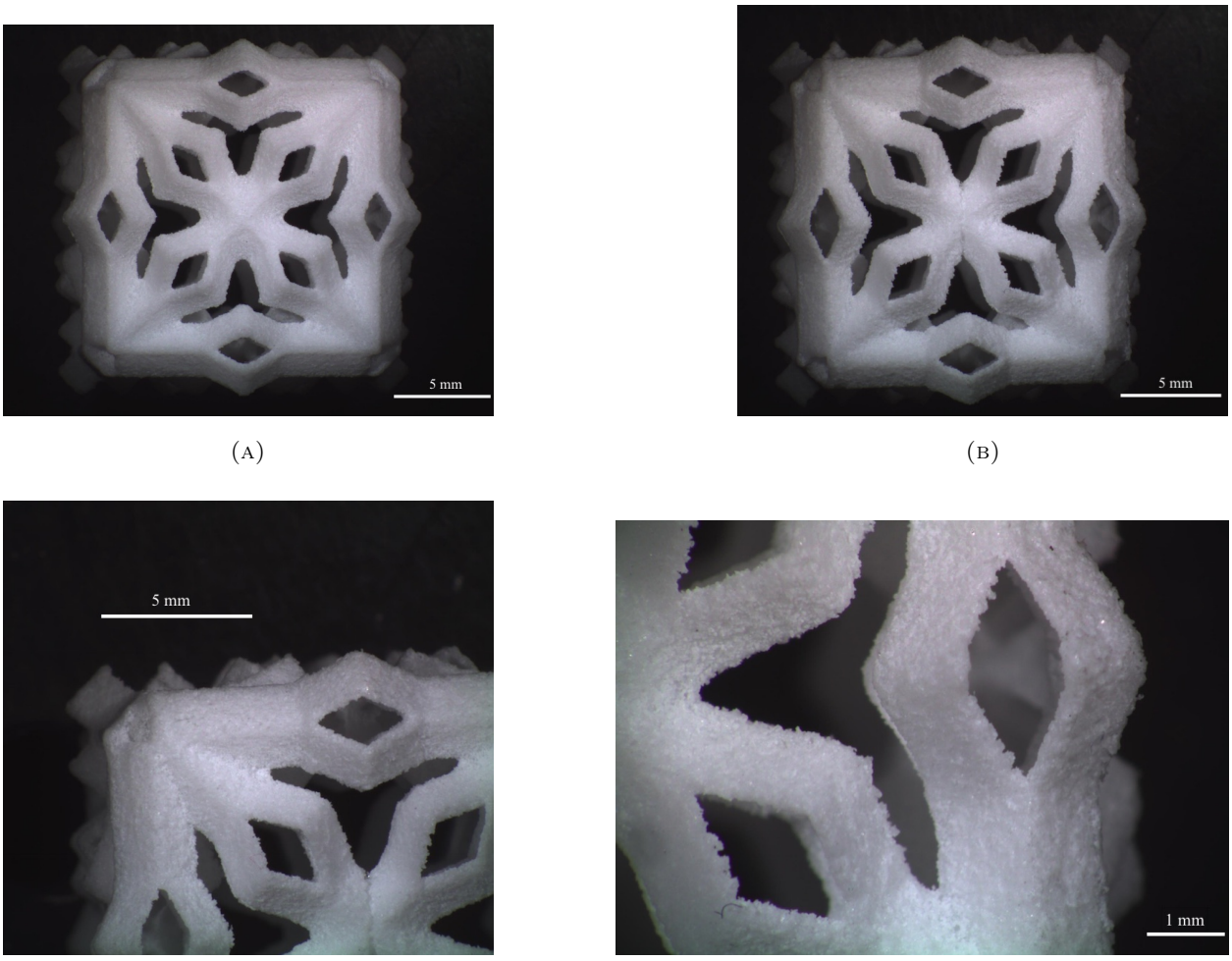

(A) (B)

(C) (D)

FIGURE A.19: Photographs taken by stereo microscope of a revised unit cell with square ribs and four fold plate element corrugation rotated 45° about their longitudinal axes (S1_rev4). Overall dimensions were 14 mm on a side. (a) Top (or bottom) surface, (b) Side surface, (c) A close-up view of joints, (d) A close-up view of open portion (i.e., corrugations).

- **September 22, 2016** - The previously created unit cell composed of triangular corrugation ribs with three plans of symmetry (T2_rev1 shown in Figure A.16b) was revised to have side length of 14 mm and 3d-printed for comparison to unit cell S1_rev4 shown in Figure A.19. Three copies of each were fabricated with finish level 1 for $36. Polyamide (nylon 12) was

used as a parent material. These specimens were received on September 28, 2016.

Comments: As shown in Figure A.20, the final products were in excellent condition. No printing defects were visible, and the desired slenderness was achieved.

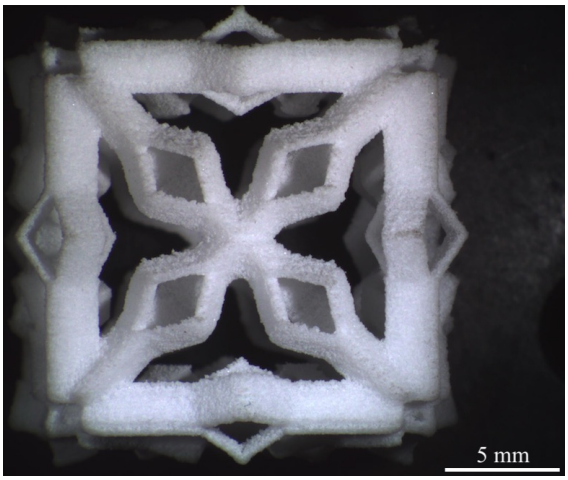

FIGURE A.20: Photographs taken by stereo microscope of unit cell consisting of triangular ribs with three corrugations where ribs are oriented to have three planes of symmetry (T2_rev2). Overall dimensions were 14 mm on a side.

- **April 19, 2017** - 3×3×1, 3×3×2, and 3×3×3 energy absorption lattice structures presented in Chapter 7 were fabricated for the purpose of correlation analysis between finite element analysis and cyclic loading experiments. Two copies of each structure with finish level one were priced at $522. Polyamide (nylon 12) was used as a parent material. These specimens were received on April 30, 2017.

  Comments: Figure A.21 shows a photograph of a 3×3×3 energy absorption lattice structure. The final product disclosed adequate slenderness giving rise to the desired snap-through behavior, hence hysteresis in a load-displacement relationship subjected to cyclic loading was seen experimentally. As a result, energy absorption phenomenon was successfully observed.

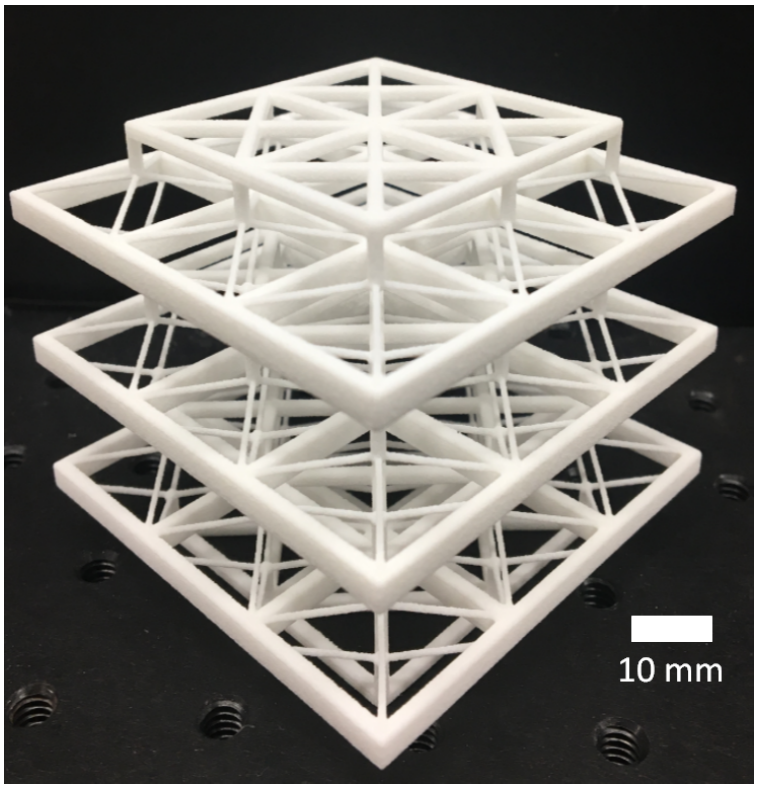

FIGURE A.21: A Photograph of a 3×3×3 energy absorption lattice structure which is also shown in Figure 7.4. This structure is approximately 70 mm on a side.

- **November 15, 2017** - 2×2×2 and 3×3×3 cubic lattice structures with negative stiffness were fabricated to conduct cyclic loading experiments for future research. These structures are expected to absorb energy similar to the previously developed structures shown in Figure A.21 but has a cubic symmetry, hence energy absorption in three principal directions is achievable. Two copies of each structure with finish level one were priced at $366. Polyamide (nylon 12) was used as a parent material. These specimens were received on November 22, 2017.

  Comments: Figure A.22 shows a photograph of a 3×3×3 cubic lattice structure with negative stiffness. The expected slenderness was achieved. Cyclic loading tests showed hysteresis in its load-displacement relationship.

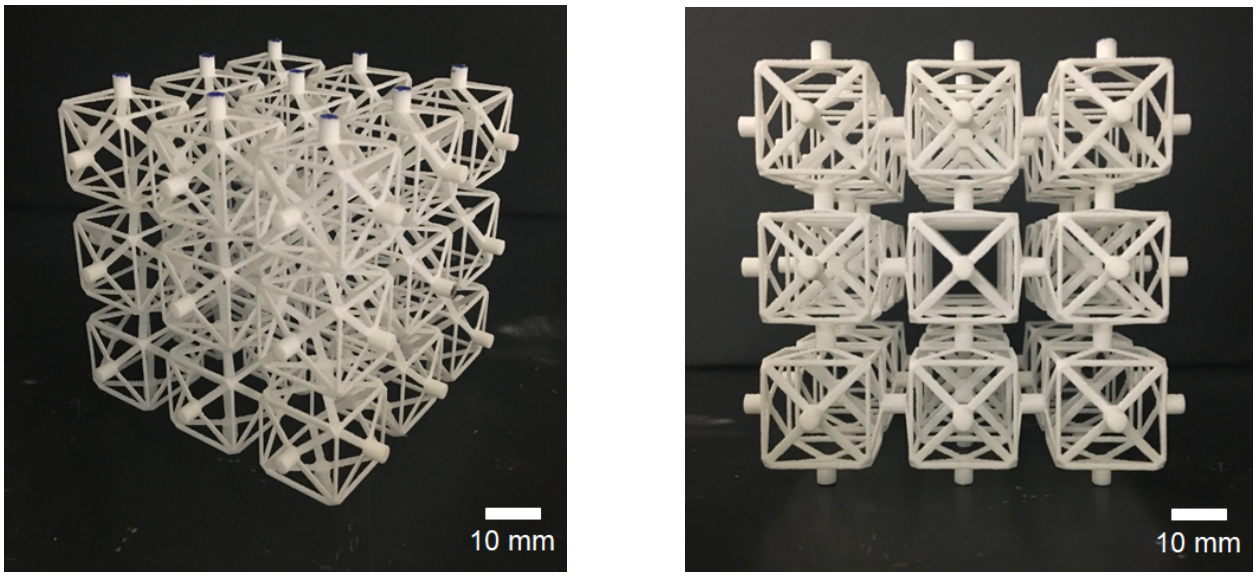

(A) (B)

FIGURE A.22: A photograph of 3×3×3 negative stiffness lattice structure with a side length of approximately 80 mm. (a) Isometric view. (b) Side view.

- **January 30, 2018** - 2×2×6 and 3×3×9 negative stiffness cubic lattice structures were fabricated for the purpose of wave experiments for future research, as shown in Figures A.23 and A.24. Two copies of each structure with finish level one were priced at $264. Polyamide (nylon 12) was used as a parent material. These specimens were received on February 8, 2017.

  Comments: The expected slenderness was achieved.

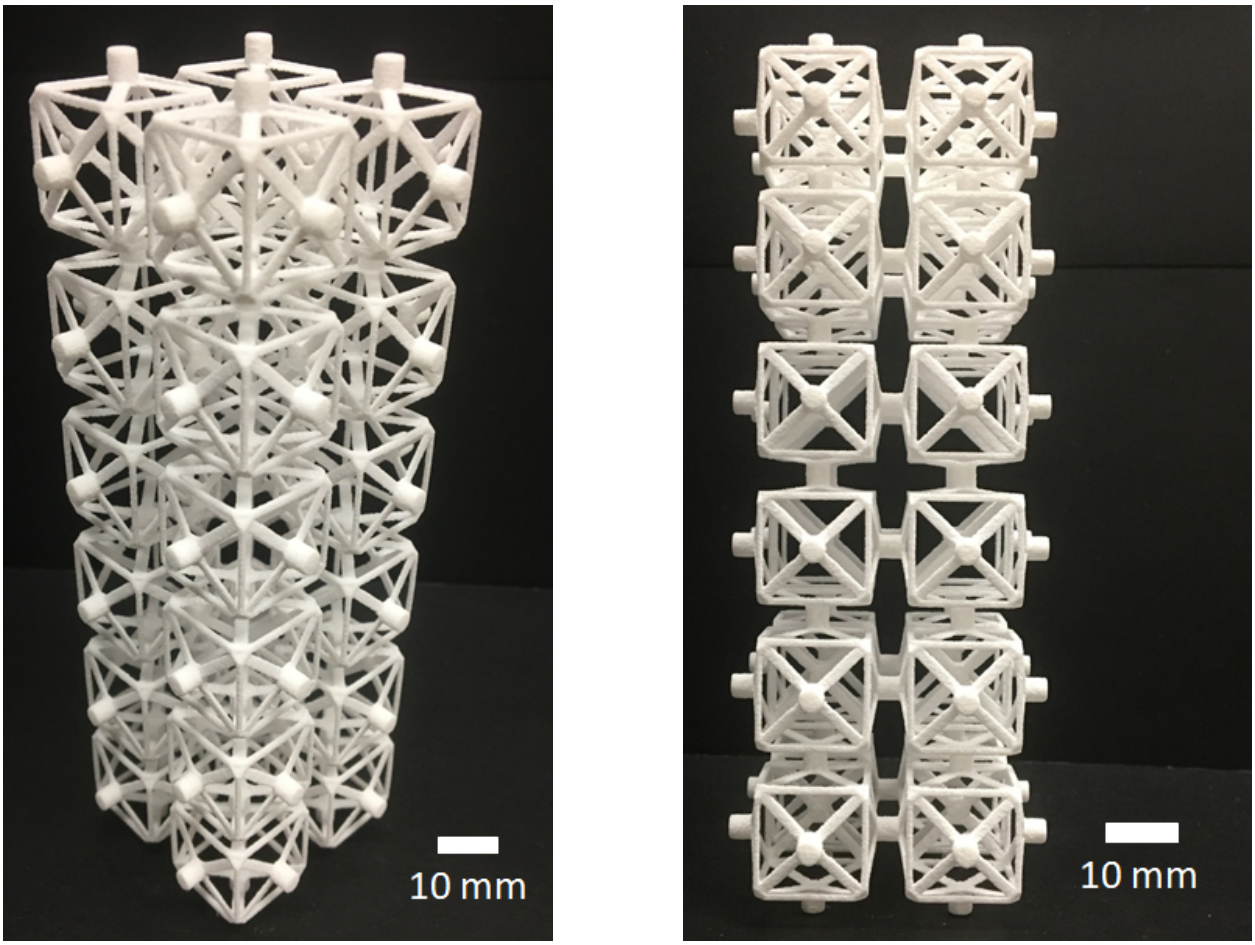

(A) (B)

FIGURE A.23: A photograph of 2×2×6 negative stiffness lattice structure. Overall dimensions are 48.50×48.50×138.35 mm. (a) Isometric view. (b) Side view.

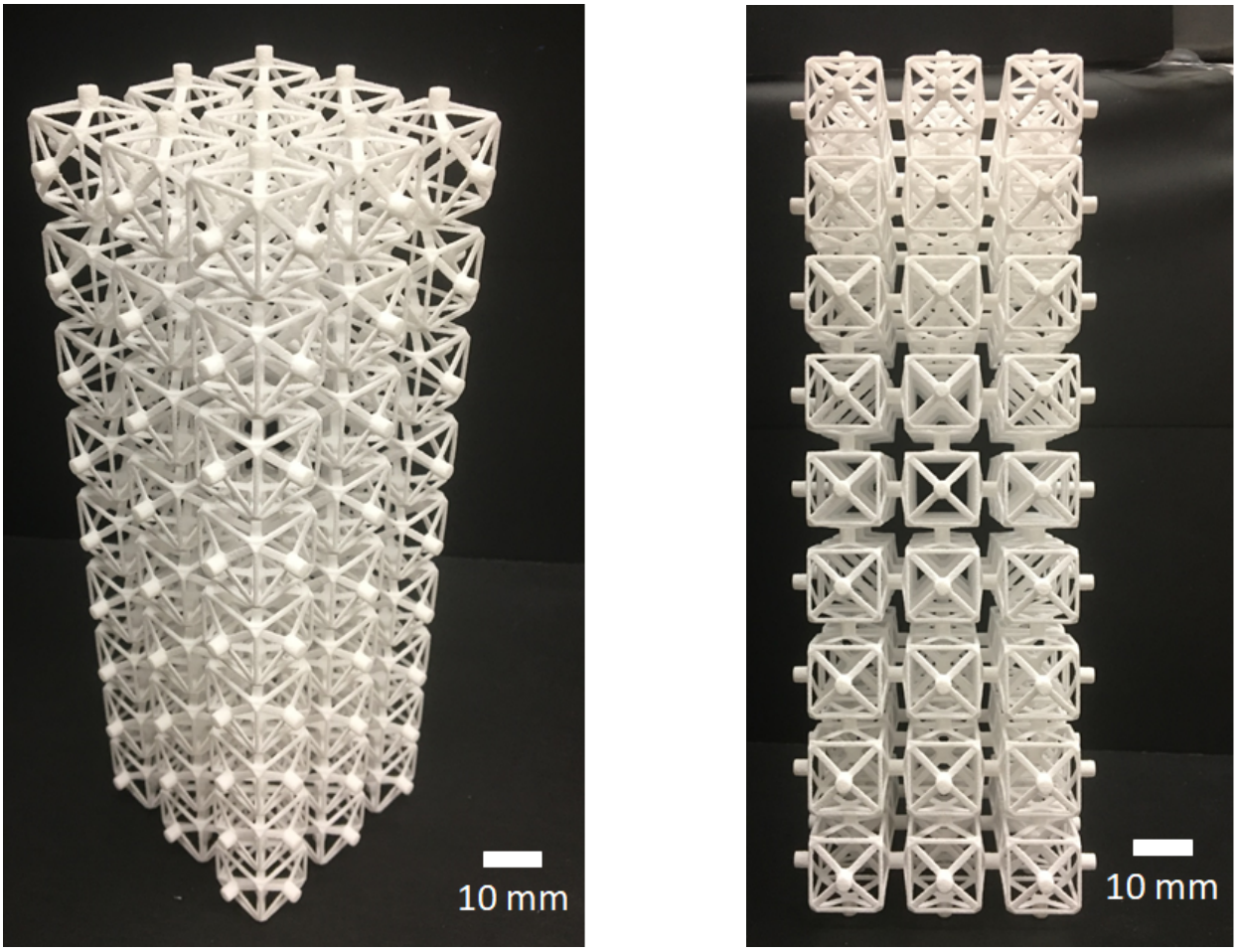

(A) (B)

FIGURE A.24: A photograph of 3×3×9 negative stiffness lattice structure. Overall dimensions are 70.97×70.97×205.74 mm. (a) Isometric view. (b) Side view.

Fused deposition modeling (FDM) Fused deposition modeling (FDM) utilizes thermoelastic extrusion to build parts layer by layer. Parts fabricated via FDM are suitable from unique prototypes to production parts.

Specifications

- 3D printer type: Stratasys FORTUS 400mc

- Available materials: ULTEM 9085, Polycarbonate (PC), ABBS-M30 (See Table A.8 for bulk material properties)
- Build envelope: 16" × 14" × 16" (= 355 × 254 × 254 mm)
- Layer thickness will vary between 0.005" - 0.013" (= 0.127 mm - 0.3302 mm), dependent on material selection.
- Minimum size of part: 0.01" - 0.026" (= 0.254 mm - 0.6604 mm), assuming FDM needs to make 2 passes to make a structure.
- Tolerances: parts are produced within an accuracy of +/- .005 inch or +/-.0015 inch per inch, whichever is greater.

Notes

- Some designs sometimes require support structures during printing, easily removed during post-process.
- Part geometry, wall thickness, and build orientation can have an effect on tolerances.

TABLE A.8: Available bulk materials and material properties for FDM [172].

	ULTEM 9085	Polycarbonate (PC)	ABS-M30
Available colors	Tan	White	White Dark gray Black
Notable for	- High heat and chemical resistance - FST (flame, smoke, toxicity) certified Thermoplastic - Ideal for commercial transportation applications	- High tensile and flexural strength - Ideal for demanding jobs, including tool, metal bending and composite work - Feature Definition and Surface Appeal	- Ideal for conceptual modeling and end-use parts - Higher impact and tensile strength than traditional ABS - Production grade thermoplastic
Properties	n/a	n/a	n/a

Polyjet/Objet (material jetting) This 3D printer, which performs material jetting (MJ) technology, offers a diverse range of materials and is an excellent option for realistic, high-resolution models and prototypes, short-run injection molds and master patterns for urethane casting. MJ utilizes multiple print nozzles jetting one or more liquid photopolymers onto a build platform. The jetted photopolymer are cured by UV light passes and solidified layer by layer. This process is repeated until the model is complete. Materials of different colors and/or durometers can be deposited in the same part if desired to simulate overmolded parts.

Specifications

- Available materials: TangoBlack FLX973, TangoGray FLX950, VeroClear RGD810 (See Table A.9 for bulk material properties).
- Maximum build envelope of 11.57" × 7.55" × 5.85" (= 29.38 × 19.18 × 14.86 in centimeters)
- High resolution layer thickness will vary between 0.0006" - 0.0011" (= 0.01524 mm - 0.002794 mm), dependent on material selection.
- Tolerances: parts are produced with a resolution of less than 0.002" (= 0.0508 mm) and an accuracy of +/- 0.004" (= +/- 0.1016 mm)for the first inch and +/- 0.0015" (= +/- 0.0381) for each additional inch.

Notes

- Wax-like structures are built to support the model during printing, easily removed during post-process.
- Part geometry, wall thickness, and build orientation can have an effect on tolerances.

TABLE A.9: Available bulk materials and material properties for Polyjet [173].

	TangoBlack FLX973	TangoGray FLX950	VeroClear RGD810
Appearance	Black	Gray	Clear
Notable for	Flexible, elastomer-like	Flexible, elastomer-like	Rigid, fine details
Tensile Ultimate Modulus (ASTM D638)	0.8-2.4 MPa	3-5 MPa	49.99-65.15 MPa
Tensile Modulus (ASTM D638)	n/a	n/a	2-3 GPa
Elongation at break, ϵ_{break}	0.45-0.55	0.45-0.55	0.10-0.25
Flexural Ultimate Strength (ASTM D790)	n/a	n/a	75-110 MPa
Flexural Modulus (ASTM D790)	n/a	n/a	2.2-3.2 GPa
Impact Strength (IZOD) (ASTM D256)	n/a	n/a	20-30 J/m
Heat Deflection Temperature at 0.45 MPa (ASTM D648)	n/a	n/a	45-50 °C
Glass Transition temperature (Tg)	n/a	n/a	52-54 °C
Shore hardness	60-62	73-77	83-86
Water absorption (ASTM D570)	n/a	n/a	1.1-1.5 %

Printing history

- **July 20, 2016** The same triangular unit cell printed by FDM previously (T2_rev1 shown in Figure A.11b) was 3d-printed via material jetting method with finish level one which included

removal of supports and light beading blasting. A parent material was Veroblue, and one copy of this unit cell was fabricated for $70. The part was received on July 26, 2016.

Comments: Print resolution was superficial and a fabricated model was flexible. However, the model was dimensionally inconsistent, as shown in Figure A.25. Most of the faces were not square and many of the ribs were warped. These shrinkage and distortion seemed to be caused by the curing process.

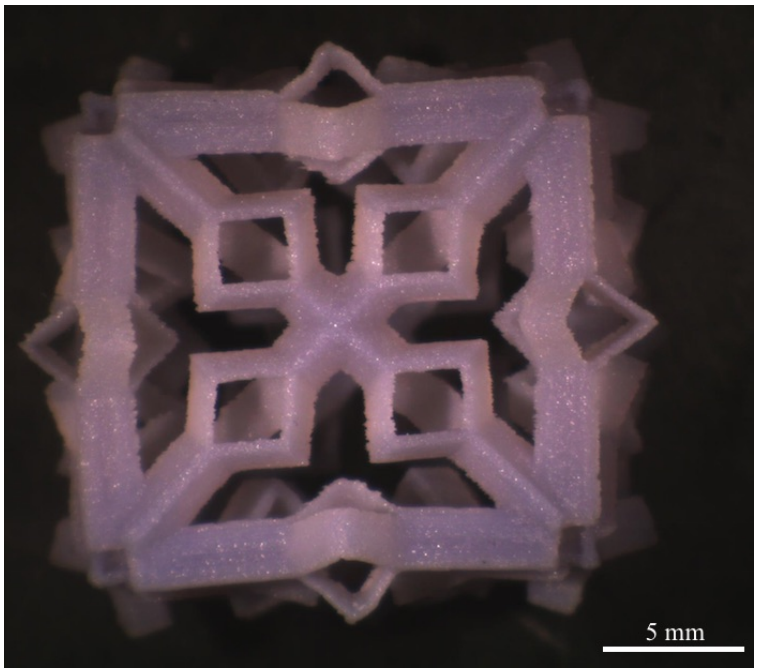

FIGURE A.25: A photograph of the unit cell consisting of triangular ribs with three fold plate elements corrugations where ribs are oriented to have three planes of symmetry (T2_rev1) was printed by material jetting method. Overall dimensions were 16 mm on a side. Superficial print resolution was observed, however dimensionally inconsistent was found due to shrinkage/distortion during the curing process.

Z Corp (binder jetting) Z Corp uses 5 color printheads (CYMK and clear) to deposit small droplets of color binder to solidify a powder bed. The powdered material, often referred to as plaster, starch, or gypsum powder, has a granular finish and is brittle out of the machine. After printing, the parts are cleaned of any powder, coated in super glue to add strength, and sprayed with a clear lacquer to protect and smooth the surface. Parts created by binder jetting are most

often used for visual display models and not for functional prototypes.

Specifications

- Max build size: 15" × 10" × 8" (= 381 mm × 254 mm × 203.2 mm)
- Resolution: 600 × 540 dpi (equivalent to 0.042 mm; *the author is not sure about this*)
- Layer thickness: 0.004" (= 0.1016 mm)
- Printheads: 5 (CYMK and clear)

Material information

- Color: 24 bit color
- Material: Visijet PXL
- Finish: Granular or Sandstone
- Coating: Matte or Gloss

Design recommendations

- Minimum wall thickness: 0.080" (= 2.032 mm)
- Minimum standalone features: 0.040" (= 1.1016 mm)
- Minimum detail: 0.020" (= 0.508 mm)
- Clearances: 0.016" (= 0.4064 mm)
- File type: PLY, VRML, COLOR STL

Finishing and post-processing The Midwest Prototyping provides finishing and post-processing with cost; these are recommended for prototypes printed via SLA in particular, because SLA requires to have supports during printing which need to be removed during post processing.

SLA finish levels

Finishing level: process inclusions

Level 1 Supports removed, support faces sanded and lightly bead blasted

Level 2 Supports removed, support faces sanded and entire part bead blasted

Level 2+ Sanded to 180 grit - blending all accessible layer lines (sand marks will still be present), and entire part bead blasted

Level 3 Sand to 320 removing all accessible layer lines so it's ready to prime/paint

Level 4 Sanded to 600 Wet **Required when parts are to be plated or to enhance transparency (Accura 60)**

SLS finish levels

Finishing level: process inclusions

Level 1 Excess powder removed, lightly bead blasted.

Level 2 Excess powder removed, lightly bead blasted, and sealed to make the product watertight.

Level 3 Excess powder removed, lightly bead blasted, sealed and sanded to promote a smoother appearance

Tumbling Parts can be tumbled for a smooth surface finish

Dying Various colors available

Paint/cosmetic options

Process Offered: level availability

Primer Available at any finish level

Paint (Gloss or Matte) Available at any finish level

Clear Coat Available at any finish level

Soft Touch Available at any finish level

Texture Available at any finish level

Dye Available at any finish level

Optical Clear Level 4 Finish Required

Vacuum Metalizing Level 4 Finish Required

A.4.2 EIGERlab

This labratory was referred by one of representatives (Mike Roosa) at Midwest Prototyping. Detailed information can be found at `http://www.eigerlab.org`.

Location

EIGERlab has two offices as follows.

1. Northern Illinois University (NIU) EIGERlab CoWorking Space - NIU-Rockford: 8500 E. State St., Rockford, IL 61108
2. NIU EIGERlab Center for Product Development: 5299 Zenith Parkway, Loves Park, IL 61111

Contact information

Office: 815-965-3522

Fax: 815-316-6345

A.4.3 Stratasys Direct

Stratasys Direct is a sub-company of Stratasys that is a leading company who builds various types of 3D printers with different technologies including FDM, SLS and Polyjet. Free online quote service is available at `http://www.stratasysdirect.com`.

Location

28309 Ave Crocker, Valencia, CA 91355

Contact information

Toll-free: 1-888-311-1017

info@stratasysdirect.com

Notes

- Online quote for 5×5×5 3D chiral lattices via FDM was $1080 (about twice expensive than that quoted by Team Lab).

A.4.4 Online resources

Recently, 3D printing becomes popular for various purposes including fabricating prototypes for production and research. There are many online 3D printing companies available. By uploading STL files (sometimes CAD files), quotations are available at no cost. As mentioned before, the cost for printing is expensive as compared to in-campus resources.

- Midwest Prototyping `https://www.midwestproto.com`
- EIGERlab `http://www.eigerlab.org`
- 3D printing price check `http://3Dprintingpricecheck.com`
- The UPS store `https://madison-wi-3391.theupsstorelocal.com/products-services/new-3D-printing`
- Ponoko `http://www.ponoko.com/3D-printing`
- Shapeways `http://www.shapeways.com`
- Xcentric `https://www.xcentricmold.com/rapid-prototyping.php`
- Stratasys direct manufacturing `https://www.stratasysdirect.com`
- Additively `https://www.additively.com`
- Xometry `https://www.xometry.com`

Appendix B

Tensile properties of 3D-printed test specimens

Abstract This paper presents a comparison of material properties between parent (prior to 3D printing fabrication) and (after) 3D-printed materials. Per ASTM D638-14, tentile tests were conducted for test specimens prepared by two different 3D printing processes: selective laser sintering (SLS) and material jetting (MJ), namely. Polyamide was a parent material for SLS-fabricated specimens, while test specimens prepared by MJ adopted VeroClear RGD810 as a parent material. Overall, significant differences in material properties between the parent and 3D-printed materials were seen. The elastic moduli for both the SLS-fabricated and MJ-fabricated specimens were almost a factor of two lower than that of the corresponding parent materials provided by a reference. In addition, the SLS-fabricated specimens experienced a higher elongation at break than that of the parent material, whereas an elongation at break similar to the reference was measured for the MJ-fabricated specimens. A difference in the ultimate tensile strength between the parent materials and test specimens was found to be minimal regardless of the two 3D printing methods. Poisson's ratio was measured to be 0.24 for both test specimens, and viscoelastic damping for these specimens was measured via broadband viscoelastic spectroscopy. These two quantities were not provided by the reference, so comparisons were not made.

B.1 Introduction

Nowadays, 3D printing, also called additive manufacturing, has been adopted to create a variety of complicated 3D microstructures such as microsensors, medical devices, or micro-optical systems [174]. This is due to its applicability and advantages compared to traditional manufacturing processes. In the course of my research presented in this dissertation, 3D printing has been utilized to fabricate several micro/smart-structures in order to conduct various experiments for validating results obtained from either theory or finite element analysis (FEA).

There is a wide range of parent materials (prior to 3D printing fabrication) from polymers to metals available for 3D printing prototyping. Although these parent material properties are available in the literature, there is very little material property information available for (after) 3D-printed materials [150]. In addition, there is a high chance that parent material properties may be transformed randomly due to applied temperature and/or pressure during sintering or solidifying processes which are necessary for 3D printing technology. For example, selective laser sintering (SLS) utilizes a high-temperature laser to sinter layers of fine powders selectively, and material jetting (MJ) uses inkjet print heads to jet melted wax-like materials which cool and solidify themselves.

Therefore, it is reasonable to argue that material properties of the 3D-printed materials need to be known before any structures fabricated by 3D printing are to be analyzed. In this study, 3D-printed test specimens fabricated by either SLS or MJ were prepared to conduct tensile tests according to ASTM-D638-14 [151]. Tensile properties such as a tensile strength, modulus of elasticity, yield strength, Poisson's ratio, and viscoelastic damping were measured. Finally, a comparison of material properties between the parent and the 3D-printed materials was developed.

B.2 Methods

B.2.1 Test methods

Tensile tests in this study have followed ASTM D638-14 [151]; this test method is standard test method for tensile properties of plastics.

A testing machine was a screw-driven test frame (model: MTS Sintech 10-GL) utilizing a load cell (model #: 27-00079) with 10,000 lb capacity. This load cell has a load precision of ±0.01 lb of an indicated load; digital noise is about less than one thousandth of pound-force. Both the test frame and the load cell were calibrated on September 30$^{\text{th}}$ in 2015.

A constant rate of a crosshead movement, simulating a constant strain rate, was employed for all tensile tests, which was achieved by controlling velocity to the movable member with respect to the stationary member via the provided software (called TestWorks®) linked to the test frame. The software as well as the provided handset also allow the user to position the crosshead manually with coarse and fine movements. For test specimens fabricated by material jetting (MJ), the constant rate of the crosshead movement was 50 mm/min, while 5 mm/min constant rate was applied to test specimens 3D-printed by selective laser sintering (SLS).

The test specimen was held by grips composed of a fixed member and a movable member attached to the crosshead. These grips are self-aligning type in such a manner that they will move freely into alignment once any load is applied so that the longitudinal axis of the test specimen will align with the direction of the crosshead through the center line of the grip assembly. Possible slippage relative to the grips was prevented by grip surfaces that are serrated with a pattern.

Both total tensile load and the corresponding displacement carried by the test specimen were displayed and stored in real time by the software. Once the tests were completed, data including both the load and the displacement was exported as a file in a form of `txt` format.

B.2.2 Test specimen fabrication

3D-printed test specimens fabricated by either selective laser sintering (SLS) or material jetting (MJ) employed a standard dumbbell shape, conforming to the dimensions according to ASTM D638-14 [151], as shown in Figure B.1. These specimens are considered as rigid or semi-rigid plastics per this standard.

These test specimens were modeled by SolidWorks®, and the corresponding `STL` files were generated and submitted to Midwest Prototyping (located in Blue Mounds, WI [147]) for 3D printing fabrication; detailed information of this company can be found in Appendix A. Parent material for SLS-fabricated specimens was polyamide (PA), while VeroClear RGD810 was used for MJ-prepared specimens.

Three test specimens were 3D-printed by SLS; they are modeled based on the Type I specifications according to ASTM D638-14. These dimensions are listed in Table B.1.

Unlike aforementioned SLS-fabricated test specimens, only two test specimens that followed the Type III specifications were prepared by MJ. The rationale is that most micro/smart-structures in my research have been fabricated via SLS. Hence, it is reasonable to allocate available resources for a study of structures fabricated by SLS instead of that prepared by MJ.

For measuring Poisson's ratio ν, square beam test specimens for each 3D printing method were prepared. Dimensions of the square beam were 10 mm $\times$ 10 mm $\times$ 50 mm. Digital images were taken when these specimens subjected to 2 % strain. For easy measurements, all test specimens were marked on edges.

Loss tangent tanδ representing damping caused by viscoelastic effects was measured by broadband viscoelastic spectroscopy (BVS). Circular rods for each 3D printing method were prepared, and they had the diameter of 0.5 mm with the length of 30 mm. Details of BVS measurement can be found in Ref. [38].

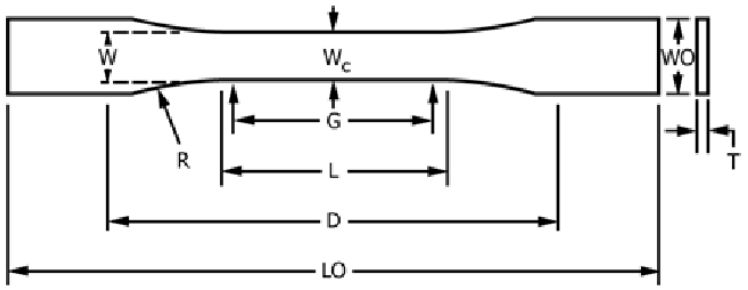

FIGURE B.1: Drawing of the test specimen per ASTM D638-14 [151].

TABLE B.1: Test specimen dimensions.

	Type I [mm]	Type III [mm]
W - Width of narrow section	13	19
L - Length of narrow section	57	57
WO - Width overall, min	19	29
LO - Length overall, min	165	246
G - Gage length	50	50
D - Distance between grips	115	115
R - Radius of fillet	76	76
T - Thickness	2	7

B.2.3 Calculations

Tensile Strength

The tensile strength can be calculated by dividing the maximum load sustained by a specimen by its original cross-sectional area in the gage length segment of the specimen.

$$\sigma_{\text{ult}} = \frac{P_{\text{max}}}{A_{\text{orig}}} \tag{B.1}$$

where P_{max} is the maximum load carried by the specimen and $A_{\text{orig}} = WT$.

Modulus of elasticity

The modulus of elasticity E, also called Young's modulus, can be determined by dividing the difference in stress corresponding to any segment on the initial straight line of a stress-strain curve by the corresponding difference in strain. The original cross-sectional area in the gage length segment of a specimen was used for calculating Young's modulus. It is most likely to observe some curvature instead of the straight line, since test specimens fabricated by 3D printing utilizes polymers as their parent materials that are known to contain viscoelastic behavior. Thus, in order to obtain the modulus of elasticity, a linear fitting was applied to the initial curve of the load extension curve with the goodness of fit R^2 at least equal to 0.995.

Poisson's ratio

By definition, Poisson's ratio ν is the ratio of transverse contraction strain to longitudinal extension strain in the direction of the applied load as follows.

$$\nu = -\frac{\epsilon_{\text{transverse}}}{\epsilon_{\text{longitudinal}}} \tag{B.2}$$

B.3 Results

Measured tensile properties of 3D-printed test specimens made of either polyamide (PA) via selective laser sintering (SLS) or VeroClear RGD810 via material jetting (MJ) are listed in Table B.2. Note that these values are averaged over results from either three test specimens fabricated by SLS or two test specimens prepared by MJ. Parent material property values are also given in parentheses for a comparison in this table.

In general, considerable differences in material properties between the parent and 3D-printed materials were observed. For both 3D-printed test specimens prepared by either SLS or MJ, the measured moduli of elasticity E were found to be almost half of that of the corresponding parent materials. While elongation at break ϵ_{break} for test specimens fabricated by MJ was found to be

within the range of the provided value of the parent material, test specimens prepared by SLS obtained much higher value of ϵ_{break}. However, the measured ultimate tensile strength σ_{ult} of both specimens were similar with that of the parent materials, regardless of 3D printing methods.

Poisson's ratio was computed to be 0.24 ± 0.0084 for both 3D-printed test specimens fabricated via SLS and via MJ. This value is rather low for polymers; Poisson's ratio of typical polymers is approximately equal to 0.3.

In Table B.1, tanδ for each test specimen fabricated by either SLS or MJ is given. High tanδ means high damping. For example, at room temperature tanδ is 0.0005 at 1 Hz for steel, 0.001 at 1 Hz for aluminum, 0.02 at $\sim$ 1 Hz for wood and 0.1 at 1 Hz for polymethyl methacrylate (PMMA) [153]. Measured tanδ at 1 Hz for the test specimen prepared by SLS was 0.32 and 0.30 for bending and torsion tests, respectively. Similar values were observed for the test specimen fabricated by MJ: 0.33 from bending and 0.32 from torsion at 1 Hz. These values represent moderate damping and are consistent with the curvature of the stress-strain plot in the small strain region, as shown in Figure B.2.

TABLE B.2: Measured tensile properties of 3D-printed test specimens. Parent material property values are given in parentheses for comparison [171].

	Tensile tests per ASTM D638-14						Simple compression test	BVS test
	E [GPa]	σ_{yield} [MPa]	ϵ_{yield} [-]	σ_{ult} [MPa]	ϵ_{ult} [-]	ϵ_{break} [-]	ν [-]	tanδ @ 1 Hz
Specimen via SLS (PA)	0.717 (1.59)	31.55 (unknown)	0.044 (unknown)	45.26 (43)	0.19 (unknown)	0.21 (0.14)	0.24 (unknown)	0.32 (bending) 0.30 (torsion)
Specimen via MJ (VeroClear RGD810)	0.819 (2-3)	39.07 (unknown)	0.048 (unknown)	66.49 (49.99-65.15)	0.11 (unknown)	0.14 (0.10-0.25)	0.24 (unknown)	0.33 (bending) 0.32 (torsion)

Figure B.2 shows stress-strain curves of 3D-printed test specimens fabricated by 3D printing. Viscoelastic damping effect, represented by tanδ, can be seen in these figures. In general, all test specimens 3D-printed by SLS experienced noticeable plastic deformation before fracture as do ductile materials, as shown in Figure B.2a. On the other hand, test specimens prepared by MJ behaved

like brittle materials since they were fractured after very small plastic deformation, as depicted in Figure B.2b.

As shown in Figure B.2b, one of MJ-fabricated test specimens, denoted as Test 1 in this figure, showed a bump in the plastic region. This was because a smooth surface of this specimen which resulted in a slippage between itself and grips of a test frame. Although σ_{ult} and ϵ_{break} were affected by this slippage for this test specimen, values of E, σ_{yield} and ϵ_{yield} were still meaningful values since these tensile properties were measured within elastic regime prior to the bump. In contrast, the other test specimen was fractured without strain-gardening and necking regions; the ultimate strength and the breaking strength occurred at the same time. This was because the specimen broke at grips rather than within the desired gage length .

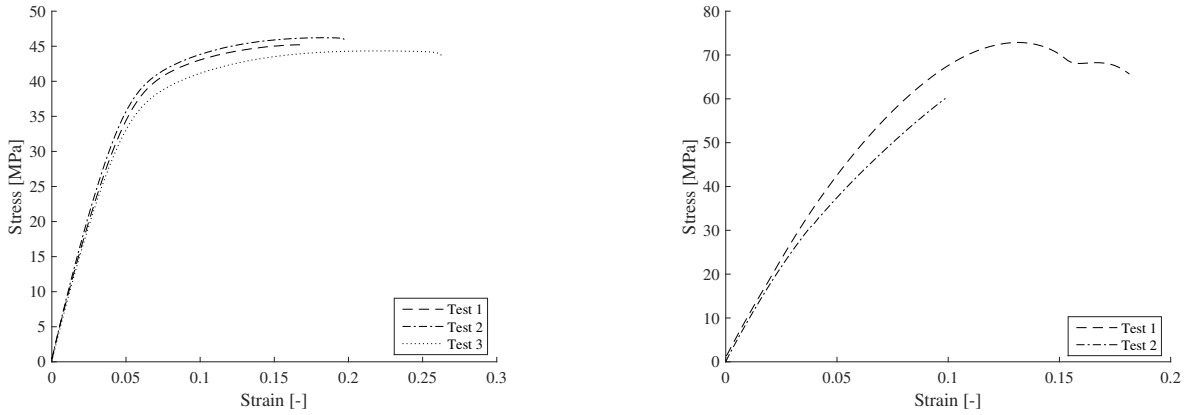

(A) (B)

FIGURE B.2: Stress-strain curves for selected 3D-printed test specimens: (a) Selective laser sintering (SLS) method. (b) Material jetting (MJ) method.

B.4 Conclusions

Tensile properties of 3D-printed test specimens fabricated via either selective laser sintering (SLS) or material jetting (MJ) were measured by conducting tensile tests according to ASTM D638-14.

A parent material was polyamide for SLS-fabricated specimens and VeroClear RGD810 for MJ-fabricated specimens. In general, significant differences in material properties between the parent and 3D-printed materials were observed. Regardless of 3D printing methods, the elastic moduli of 3D-printed test specimens were about half of the provided value of the corresponding parent materials. However, the ultimate tensile strength was found to be similar with that of the parent materials. While the elongation at break for test specimens fabricated by MJ was within the window of the provided values, test specimens 3D-printed by SLS experienced much higher elongation at break. Moreover, the Poisson's ratio of 0.24 and viscoelastic damping of approximately 0.3 were measured for all test specimens independent of 3D printing methods.

Bibliography

[1] M. M. Toropova and C. A. Steeves. "Bimaterial lattices with anisotropic thermal expansion". In: *Journal of Mechanics of Materials and Structures* 9.2 (2014). DOI: http://dx.doi.org/10.2140/jomms.2014.9.227.

[2] I. S. Sokolnikoff. *Mathematical theory of elasticity*. 2nd ed. Malabar, FL: Krieger Pub. Co., 1983.

[3] R. S. Lakes. "Solids with tunable positive or negative thermal expansion of unbounded magnitude". In: *Applied physics letters* 90.22 (2007), p. 221905. DOI: https://doi.org/10.1063/1.2743951.

[4] J. L. Cribb. "Shrinkage and thermal expansion of a two phase material". In: *Nature* 220.5167 (1968), pp. 576–577.

[5] B. Paul. *Prediction of elastic constants of multi-phase materials*. No. TR3. BROWN UNIV PROVIDENCE RI, 1959.

[6] Z. Hashin. "Analysis of composite materials-a survey". In: *Journal of Applied Mechanics* 50.3 (1983), pp. 481–505. DOI: 10.1115/1.3167081.

[7] G. W. Milton. *The theory of composites (Cambridge monographs on applied and computational mathematics)*. Cambridge, UK: Cambridge University Press, 2002.

[8] R. A. Schapery. "Thermal expansion coefficients of composite materials based on energy principles". In: *Journal of Composite Materials* 2.3 (1968), pp. 380–404. DOI: https://doi.org/10.1177/002199836800200308.

[9] B. W. Rosen and Z. Hashin. "Effective thermal expansion coefficients and specific heats of composite materials". In: *International Journal of Engineering Science* 8.2 (1970), pp. 157–173. DOI: https://doi.org/10.1016/0020-7225(70)90066-2.

[10] L. J. Gibson and M. F. Ashby. *Cellular Solids*. 2nd ed. Cambridge, UK: Cambridge Press University, 1997.

[11] R. S. Lakes. "Cellular solid structures with unbounded thermal expansion". In: *Journal of Materials Science Letters* 15.6 (1996), pp. 175–477.

[12] O. Sigmund and S. Torquato. "Composites with extremal thermal expansion coefficients". In: *Applied physics letters* 69.21 (1996), pp. 3203–3205. DOI: https://doi.org/10.1063/1.117961.

[13] R. S. Lakes. "Dense solid microstructures with unbounded thermal expansion". In: *Journal of the Mechanical Behavior of Materials* 7.2 (1996), pp. 85–92. DOI: https://doi.org/10.1515/JMBM.1996.7.2.85.

[14] R. S. Lakes. "Piezoelectric composite lattices with high sensitivity". In: *Philosophical Magazine Letters* 94.1 (2014), pp. 37–44. DOI: https://doi.org/10.1080/09500839.2013.855331.

[15] B. Rodriguez, H. Kalathur, and R. Lakes. "A sensitive piezoelectric composite lattice: Experiment". In: *physica status solidi (b)* 251.2 (2014), pp. 349–353. DOI: https://doi.org/10.1002/pssb.201384253.

[16] W. Voigt. *Theoretische studien über die elasticitätsverhältnisse der krystalle*. Königliche Gesellschaft der Wissenschaften zu Göttingen, 1887.

[17] E. Cosserat and F. Cosserat. *Théorie des corps déformables, Paris*. 1909.

[18] R. D. Mindlin and H. F. Tiersten. "Effects of couple-stresses in linear elasticity". In: *Archive for Rational Mechanics and analysis* 11.1 (1962), pp. 415–448.

[19] A. C. Eringen and E. S. Suhubi. "Nonlinear theory of simple micro-elastic solids-I". In: *International Journal of Engineering Science* 2.2 (1964), pp. 189–203. DOI: https://doi.org/10.1016/0020-7225(64)90004-7.

[20] E. S. Suhubi and A. C. Eringen. "Nonlinear theory of micro-elastic solids-II". In: *International Journal of Engineering Science* 2.4 (1964), pp. 389–404. DOI: https://doi.org/10.1016/0020-7225(64)90017-5.

[21] R. D. Mindlin. "Microstructure in Linear Elasticity". In: *Archive for Rational Mechanics and Analysis* 16.1 (1964), pp. 51–78.

[22] A. C. Eringen. "Linear Theory of Micropolar Elasticity". In: *Journal of Mathematics and mechanics* 15.6 (1966), pp. 909–923.

[23] A. C. Eringen. "Theory of micropolar elasticity". In: *Fracture Vol.* Ed. by H. Liebowitz. New York: Academic Press, 1968, pp. 621–729.

[24] S. C. Cowin. "Stress functions for Cosserat elasticity". In: *International Journal of Solids and Structures* 6.4 (1970), pp. 389–398. DOI: https://doi.org/10.1016/0020-7683(70)90091-0.

[25] S. C. Cowin. "An incorrect inequality in micropolar elasticity theory". In: *Zeitschrift für Angewandte Mathematik und Physik (ZAMP)* 21.3 (1970), pp. 494–497. DOI: https://doi.org/10.1007/BF01627956.

[26] R. D. Gauthier and W. E. Jahsman. "A quest for micropolar Elastic Constants". In: *Journal of Applied Mechanics* 42.2 (1975), pp. 369–374. DOI: 10.1115/1.3423583.

[27] G. V. Krishna Reddy and N. K. Venkatasubramanian. "On the flexural rigidity of a micropolar elastic circular cylinder". In: *Journal of Applied Mechanics* 45.2 (1978), pp. 429–431.

[28] R. D. Mindlin. "Effect of couple stresses on stress concentrations". In: *Experimental Mechanics* 3 (1963), pp. 1–7.

[29] P. N. Kaloni and T. Ariman. "Stress concentration effects in micropolar elasticity". In: *Zeitschrift für Angewandte Mathematik und Physik (ZAMP)* 18.1 (1967), pp. 136–141. DOI: https://doi.org/10.1007/BF01593904.

[30] B. S. Kim and A. C. Eringen. "Stress distribution around an elliptic hole in an infinite micropolar elastic plate". In: *Letters in Applied and Engineering Sciences* 1 (1973), pp. 381–390.

[31] H. C. Park and R. S. Lakes. "Cosserat micromechanics of human bone: strain redistribution by a hydration sensitive constituent". In: *Journal of biomechanics* 19.5 (1986), pp. 385–397. DOI: https://doi.org/10.1016/0021-9290(86)90015-1.

[32] R. S. Lakes and R. L. Benedict. "Noncentrosymmetry in micropolar elasticity". In: *International Journal of Engineering Science* 20.10 (1982), pp. 1161–1167. DOI: https://doi.org/10.1016/0020-7225(82)90096-9.

[33] X. N. Liu, G. L. Huang, and G. K. Hu. "Chiral effect in plane isotropic micropolar elasticity and its application to chiral lattices". In: *Journal of the Mechanics and Physics of Solids* 60.11 (2012), pp. 1907–1921. DOI: https://doi.org/10.1016/j.jmps.2012.06.008.

[34] D. Prall and R. S. Lakes. "Properties of a chiral honeycomb with a Poisson's ratio -1". In: *International Journal of Mechanical Sciences* 39.3 (1996), pp. 305–314. DOI: https://doi.org/10.1016/S0020-7403(96)00025-2.

[35] R. S. Lakes. "Experimental microelasticity of two porous solids". In: *International Journal of Solids and Structures* 22.1 (1986), pp. 55–63. DOI: https://doi.org/10.1016/0020-7683(86)90103-4.

[36] W. B. Anderson and R. S. Lakes. "Size effects due to Cosserat elasticity and surface damage in closed-cell polymethacrylimide foam". In: *Journal of Materials Science* 29.24 (1994), pp. 6413–6419. DOI: https://doi.org/10.1007/BF00353997.

[37] R. Lakes. "On the torsional properties of single osteons". In: *Journal of biomechanics* 28.11 (1995), pp. 1409–1409.

[38] Z. Rueger and R. S. Lakes. "Cosserat elasticity of negative Poisson's ratio foam: experiment". In: *Smart Materials and Structures* 25.5 (2016), p. 054004. DOI: 10.1088/0964-1726/25/5/054004.

[39] Z. Rueger and R. S. Lakes. "Experimental Cosserat elasticity in open-cell polymer foam". In: *Philosophical Magazine* 96.2 (2016), pp. 93–111. DOI: https://doi.org/10.1080/14786435.2015.1125541.

[40] R. S. Lakes. "Negative-Poisson's-ratio materials: auxetic solids". In: *Annual Review of Materials Research* 47 (2017). DOI: https://doi.org/10.1146/annurev-matsci-070616-124118.

[41] S. D. Poisson. *Traité de mécanique*. Paris: Société belge de librairie, 1938.

[42] R. S. Lakes. "Foam structures with a negative Poisson's ratio". In: *Science* 235.4792 (1987), pp. 1038–1040.

[43] R. S. Lakes, P. Rosakis, and A. Ruina. "Microbuckling instability in elastomeric cellular solids". In: *Journal of Materials Science* 28.17 (1993), pp. 4667–4672. DOI: https://doi.org/10.1007/BF00414256.

[44] A. Yeganeh-Haeri, D. J. Weidner, and J. B. Parise. "Elasticity of a-cristobalite: a silicon dioxide with a negative Poisson's ratio". In: *Science* 257.5070 (1992), pp. 650–652. DOI: 10.1126/science.257.5070.650.

[45] D. Prall and R. S. Lakes. "Properties of a chiral honeycomb with a Poisson's ratio of -1". In: *International Journal of Mechanical Sciences* 39.3 (1997), pp. 305–314. DOI: https://doi.org/10.1016/S0020-7403(96)00025-2.

[46] R. H. Baughman et al. "Negative Poisson's ratios as a common feature of cubic metals". In: *Nature* 392.6674 (1998), pp. 362–365. DOI: https://doi.org/10.1038/32842.

[47] H. Yasuda and J. Yang. "Reentrant origami-based metamaterials with negative Poisson's ratio and bistability". In: *Physical review letters* 114.18 (2015), p. 185502. DOI: https://doi.org/10.1103/PhysRevLett.114.185502.

[48] J. Glieck. "Anti-rubber". In: *New York Times* 14 (1987).

[49] K. E. Evans et al. "Molecular network design". In: *Nature* 353.6340 (1991). DOI: https://doi.org/10.1038/353124a0.

[50] G. W. Milton. "Composite materials with Poisson's ratios close to -1". In: *Journal of the Mechanics and Physics of Solids* 40.5 (1992), pp. 1105–1137. DOI: https://doi.org/10.1016/0022-5096(92)90063-8.

[51] Y. C. Fung. *Foundations of solid mechanics*. Englewood, NJ: Prentice Hall, 1965.

[52] J. M. T. Thompson. "Stability predictions through a succession of folds". In: *Philosophical Transactions of the Royal Society of London A* 292.1386 (1979), pp. 1–23. DOI: 10.1098/rsta.1979.0043.

[53] R. S. Lakes. "Extreme damping in compliant composites with a negative-stiffness phase". In: *Philosophical Magazine Letters* 81.2 (2001), pp. 95–100. DOI: https://doi.org/10.1080/09500830010015332.

[54] Z. P. Bažant and L. Cedolin. *Stability of structures*. Oxford: University Press, 1991.

[55] R. S. Lakes. "Extreme Damping in Composite Materials with a Negative Stiffness Phase". In: *Physical review letters* 86.13 (2001), p. 2897. DOI: https://doi.org/10.1103/PhysRevLett.86.2897.

[56] R. S. Lakes et al. "Extreme damping in composite materials with negative-stiffness inclusions". In: *Nature* 410.6828 (2001), p. 565. DOI: https://doi.org/10.1038/35069035.

[57] Y. C. Wang and R. S. Lakes. "Extreme thermal expansion, piezoelectricity, and other coupled field properties in composites with a negative stiffness phase". In: *Journal of Applied Physics* 90.12 (2001), pp. 6458–6465. DOI: https://doi.org/10.1063/1.1413947.

[58] R. S. Lakes and W. J. Drugan. "Dramatically stiffer elastic composite materials due to a negative stiffness phase?" In: *Journal of the Mechanics and Physics of Solids* 50.5 (2002), pp. 979–1009. DOI: https://doi.org/10.1016/S0022-5096(01)00116-8.

[59] Y. C. Wang and R. S. Lakes. "Extreme stiffness systems due to negative stiffness elements". In: *American Journal of Physics* 72.1 (2004), pp. 40–50. DOI: https://doi.org/10.1119/1.1619140.

[60] T. Jaglinski and R. S. Lakes. "Adaptive Structures: Engineering Applications". In: *Adaptive Structures–Engineering Applications*. Ed. by D. Wagg et al. Chichester, England: John Wiley & Sons, 2007, pp. 231–246.

[61] T. Jaglinski et al. "Composite Materials with Viscoelastic Stiffness Greater Than Diamond". In: *Science* 315.5812 (2007), pp. 620–622. DOI: https://doi.org/10.1016/S0022-5096(01)00116-8.

[62] Z. Hashin and S. Shtrikman. "A variational approach to the theory of the elastic behaviour of multiphase materials". In: *Journal of the Mechanics and Physics of Solids* 11.2 (1963), pp. 127–140. DOI: https://doi.org/10.1016/0022-5096(63)90060-7.

[63] M. Caruel, J. M. Allain, and L. Truskinovsky. "Mechanics of collective unfolding". In: *Journal of the Mechanics and Physics of Solids* 76 (2015), pp. 237–259. DOI: https://doi.org/10.1016/j.jmps.2014.11.010.

[64] S. Schaare et al. "Point loading of assemblies of interlocked cube-shaped elements". In: *International Journal of Engineering Science* 46.12 (2008), pp. 1228–1238. DOI: https://doi.org/10.1016/j.ijengsci.2008.06.012.

[65] E. B. Duoss et al. "Three-dimensional printing of elastomeric, cellular architectures with negative stiffness". In: *Advanced Functional Materials* 24.31 (2014), 4905–4913. DOI: https://doi.org/10.1002/adfm.201400451.

[66] D. M. Correa, C. C. Seepersad, and M. R. Haberman. "Mechanical design of negative stiffness honeycomb materials". In: *Integrating Materials and Manufacturing Innovation* 4.1 (2015), pp. 1–11. DOI: https://doi.org/10.1186/s40192-015-0038-8.

[67] D. M. Correa et al. "Negative stiffness honeycombs for recoverable shock isolation". In: *Rapid Prototyping Journal* 21.2 (2015), pp. 193–200. DOI: https://doi.org/10.1108/RPJ-12-2014-0182.

[68] L. Kashdan et al. "Design, fabrication, and evaluation of negative stiffness elements using SLS". In: *Rapid Prototyping Journal* 18.2 (2012), p. 185502. DOI: https://doi.org/10.1108/13552541211218108.

[69] L. Dong and R. S. Lakes. "Advanced damper with high stiffness and high hysteresis damping based on negative structural stiffness". In: *International Journal of Solids and Structures* 50.14-15 (2013), pp. 2416–2423. DOI: https://doi.org/10.1016/j.ijsolstr.2013.03.018.

[70] H. Kalathur and R. S. Lakes. "Column dampers with negative stiffness: high damping at small amplitude". In: *Smart Materials and Structures* 22.8 (2013), p. 084013. DOI: 10.1088/0964-1726/22/8/084013.

[71] B. A. Fulcher et al. "Analytical and experimental investigation of buckled beams as negative stiffness elements for passive vibration and shock isolation systems". In: *Journal of Vibration and Acoustics* 136.3 (2014), p. 031009. DOI: 10.1115/1.4026888.

[72] D. Chronopoulos et al. "Enhancement of wave damping within metamaterials having embedded negative stiffness inclusions". In: *Wave Motion* 58 (2015), pp. 165–179. DOI: 10.1115/1.4026888.

[73] C. B. Churchill et al. "Dynamically variable negative stiffness structures". In: *Science advances* 2.2 (2016), e1500778. DOI: 10.1126/sciadv.1500778.

[74] W. J. Drugan. "Wave propagation in elastic and damped structures with stabilized negative-stiffness components". In: *Journal of the Mechanics and Physics of Solids* 106 (2017), pp. 34–45. DOI: https://doi.org/10.1016/j.jmps.2017.04.007.

[75] S. P. Balch and R. S. Lakes. "Lumped negative stiffness damper for absorption of flexural waves in a rod". In: *Smart Materials and Structures* 26.4 (2017), p. 045022. DOI: https://doi.org/10.1088/1361-665X/aa6122.

[76] R. S. Lakes. "Giant enhancement in effective piezoelectric sensitivity by pyroelectric coupling". In: *EPL (Europhysics Letters)* 98.4 (2012), p. 47001. DOI: 10.1209/0295-5075/98/47001.

[77] L. Y. Zhang and G. K. Xu. "Negative stiffness behaviors emerging in elastic instabilities of prismatic tensegrities under torsional loading". In: *International Journal of Mechanical Sciences* 103 (2015), 189–198. DOI: https://doi.org/10.1016/j.ijmecsci.2015.09.009.

[78] H. Kalathur and R. S. Lakes. "Enhancement in piezoelectric sensitivity via negative structural stiffness". In: *Journal of Intelligent Material Systems and Structures* 27.18 (2016), 2568–2573. DOI: https://doi.org/10.1177/1045389X15624802.

[79] H. U. Schuerch. *Thermally stable macro-composite structures*. National Aeronautics and Space Administration, 1972.

[80] E. G. Collins and S. Richter. "Linear-quadratic-Gaussian-based controller design for Hubble Space Telescope". In: *Journal of Guidance, Control, and Dynamics* 18.2 (1995), pp. 208–213. DOI: http://dx.doi.org/10.2514/3.21371.

[81] C. Lind et al. "Synthesis and Properties of the Negative Thermal Expansion Material Cubic ZrMo2O8". In: *Chemistry of materials* 10.9 (1998), pp. 2335–2337. DOI: http://dx.doi.org/10.1021/cm980438m.

[82] O. Sigmund and S. Torquato. "Design of materials with extreme thermal expansion using a three phase topology optimization method". In: *Journal of the Mechanics and Physics of Solids* 45.6 (1997), pp. 1037–1067. DOI: http://dx.doi.org/10.1117/12.267131.

[83] J. S. Evans, T. A. Mary, and A. W. Sleight. "Negative thermal expansion materials". In: *Physica B: Condensed Matter* 241 (1998), pp. 311–316. DOI: http://dx.doi.org/10.1016/S0921-4526(97)00571-1.

[84] R. S. Lakes. "Cellular solids with tunable positive or negative thermal expansion of unbounded magnitude". In: *Applied Physics Letters* 90.22 (2007), p. 211905. DOI: http://dx.doi.org/10.1063/1.2743951.

[85] J. J. Lehman and R. S. Lakes. "Stiff lattices with zero thermal expansion". In: *Journal of Intelligent Material Systems and Structures* 23.11 (2012), pp. 1263–1268. DOI: http://dx.doi.org/10.1177/1045389X12445647.

[86] S. P. Timoshenko. "Analysis of bi-metal thermostats". In: *JOSA* 11.3 (1925), pp. 233–355.

[87] L. J. Gibson et al. "The mechanics of two dimensional cellular solids". In: *Proc. Royal Society London A* 382 (1982), pp. 25–42.

[88] A. Spadoni and M. Ruzzene. "Elasto-static micropolar behavior of a chiral auxetic lattice". In: *Journal of the Mechanics and Physics of Solids* 60.1 (2012), pp. 156–171. DOI: https://doi.org/10.1016/j.jmps.2011.09.012.

[89] D. Bornengo, F. Scarpa, and C. Remillat. "Evaluation of hexagonal chiral structure for morphing airfoil concept". In: *Proceedings of the Institution of Mechanical Engineers, Part G: Journal of Aerospace Engineering* 219.3 (2005), pp. 185–192. DOI: https://doi.org/10.1243/095441005X30216.

[90] J. Martin et al. "The hexachiral prismatic wingbox concept". In: *physica status solidi (b)* 245.3 (2008), pp. 570–571. DOI: https://doi.org/10.1002/pssb.200777709.

[91] A. Spadoni, M. Ruzzene, and F. Scarpa. "Global and local linear buckling behavior of a chiral cellular structure". In: *physica status solidi (b)* 242.3 (2005), pp. 695–709. DOI: https://doi.org/10.1002/pssb.200460387.

[92] A. Spadoni et al. "Phononic properties of hexagonal chiral lattices". In: *Wave Motion* 46.7 (2009), pp. 435–450. DOI: https://doi.org/10.1016/j.wavemoti.2009.04.002.

[93] H. Abramovitch et al. "Smart tetrachiral and hexachiral honeycomb: Sensing and impact detection". In: *Composites Science and Technology* 70.7 (2010), pp. 1072–1079. DOI: https://doi.org/10.1016/j.compscitech.2009.07.017.

[94] Engineered Materials Solutions, ed. *P675R strip specification.* Attleboro, MA, USA.

[95] R. S. Dean. *Manganese alloys. U.S. Patent 2,982,646.* Tech. rep. Chicago Dev Corp, 1961.

[96] J. J. Lehman and R. S. Lakes. "Stiff, strong zero thermal expansion lattices via the Poisson effect". In: *Journal of Materials Research* 29.17 (2013), pp. 2499–2508. DOI: https://doi.org/10.1557/jmr.2013.154.

[97] A. Merkel, V. Tournat, and V. Gusev. "Experimental evidence of rotational elastic waves in granular phononic crystals". In: *Physical Review Letters* 107.22 (2011), p. 225502. DOI: https://doi.org/10.1103/PhysRevLett.107.225502.

[98] M. Warner et al. "Untwisting of a cholesteric elastomer by a mechanical field". In: *Physical review letters* 85.11 (2000), pp. 2320–2324. DOI: https://doi.org/10.1103/PhysRevLett.85.2320.

[99] W. Miller et al. "Flatwise buckling optimization of hexachiral and tetrachiral honeycombs". In: *Composites Science and Technology* 70.7 (2010), pp. 1049–1056. DOI: https://doi.org/10.1016/j.compscitech.2009.10.022.

[100] A. A. Pozniak and K. W. Wojciechowski. "Poisson's ratio of rectangular anti-chiral structures with size dispersion of circular nodes". In: *physica status solidi (b)* 251.2 (2014), pp. 367–374. DOI: https://doi.org/10.1016/j.compscitech.2009.10.022.

[101] R. Gatt and J. N. Grima. "Negative Compressibility". In: *physica status solidi (RRL)–Rapid Research Letters* 2.5 (2008), pp. 236–238. DOI: https://doi.org/10.1002/pssr.200802101.

[102] A. J. Jacobsen, W. Barvosa-Carter, and S. Nutt. "Compression behavior of micro-scale truss structures formed from self-propagating polymer waveguides". In: *Acta Materialia* 55.20 (2007), pp. 6724–6733. DOI: https://doi.org/10.1016/j.actamat.2007.08.036.

[103] A. Alderson and K. E. Evans. "Rotation and dilation deformation mechanisms for auxetic behavior in the α-cristobalite tetrahedral framework structure". In: *Physics and Chemistry of Minerals* 28.10 (2001), pp. 711–718. DOI: https://doi.org/10.1007/s002690100209.

[104] N. Gaspar et al. "A generalised three-dimensional tethered-nodule model for auxetic materials". In: *Journal of Materials Science* 46.2 (2011), pp. 372–384. DOI: https://doi.org/10.1007/s10853-010-4846-0.

[105] K. L. Alderson, R. S. Webber, and K. E. Evans. "Microstructural evolution in the processing of auxetic microporous polymers". In: *physica status solidi (b)* 244.3 (2007), pp. 828–841. DOI: https://doi.org/10.1002/pssb.200572702.

[106] T. Buckmann et al. "On three-dimensional dilational elastic metamaterials". In: *New Journal of Physics* 16.3 (2014), p. 033032.

[107] R. D. Cook et al. *Concepts and Applications of Finite Element Analysis*. 4th ed. New York: John Wiley and Sons, 2002.

[108] J. F. Nye. *Physical properties of crystals: their representation by tensors and matrices*. Clarendon: Oxford university press, 1976.

[109] K. L. Alderson, A. P. Kettle, and K. E. Evans. "Novel fabrication route for auxetic polyethylene. Part 1 Processing and microstructure". In: *Polymer Engineering and Science* 45.4 (2005), pp. 568–578. DOI: https://doi.org/10.1002/pen.20311.

[110] C. Ha, M. E. Plesha, and R. S. Lakes. "Chiral three dimensional lattices with tunable Poisson's ratio". In: *Smart Materials and Structures* 25.5 (2016), p. 054005. DOI: 10.1088/0964-1726/25/5/054005.

[111] R. D. Mindlin. "Stress functions for a Cosserat continuum". In: *International Journal of Solids and Structures* 1.3 (1965), pp. 265–271. DOI: https://doi.org/10.1016/0020-7683(65)90033-8.

[112] R. Brezny and D. J. Green. "Characterization of edge effects in cellular materials". In: *Journal of Materials Science* 25.11 (1990), pp. 4571–4578. DOI: https://doi.org/10.1007/BF01129908.

[113] K. W. Wojciechowski. "Constant thermodynamic tension Monte Carlo studies of elastic properties of a two-dimensional systems of hard cyclic hexamers". In: *Molecular Physics* 61.5 (1987), pp. 1247–125. DOI: https://doi.org/10.1080/00268978700101761.

[114] K. W. Wojciechowski. "Two-dimensional isotropic systems with a negative Poisson ratio". In: *Physics Letters A* 137.1-2 (1989), pp. 60–64. DOI: https://doi.org/10.1016/0375-9601(89)90971-7.

[115] R. S. Lakes. "Third-rank piezoelectricity in isotropic chiral solids". In: *Applied Physics Letters* 106.21 (2015), p. 212905. DOI: https://doi.org/10.1063/1.4921846.

[116] R. F. Almgren. "An isotropic three dimensional structure with Poisson's ratio -1". In: *Journal of Elasticity* 15.4 (1985), pp. 427–430.

[117] J. N. Grima, A. Alderson, and K. E. Evans. "Auxetic behaviour from rotating rigid units". In: *physica status solidi (b)* 242.3 (2005), pp. 561–575. DOI: https://doi.org/10.1002/pssb.200460376.

[118] G. W. Milton. "Complete characterization of the macroscopic deformations of periodic unimode metamaterials of rigid bars and pivots". In: *Journal of the Mechanics and Physics of Solids* 61.7 (2013), pp. 1543–1560. DOI: https://doi.org/10.1016/j.jmps.2012.08.011.

[119] D. Attard and J. N. Grima. "Auxetic behaviour from rotating rhombi". In: *physica status solidi (b)* 245.11 (2008), pp. 2395–2404. DOI: https://doi.org/10.1002/pssb.200880269.

[120] J. N. Grima and K. E. Evans. "Auxetic behavior from rotating triangles". In: *Journal of Materials Science* 41.10 (2006), pp. 3193–3196. DOI: 10.1007/s10853-006-6339-8.

[121] D. Attard and J. N. Grima. "A three-dimensional rotating rigid units network exhibiting negative Poisson's ratios". In: *physica status solidi (b)* 249.7 (2012), pp. 1330–1338. DOI: https://doi.org/10.1002/pssb.201084223.

[122] R. S. Lakes. "Negative Poisson's ratio materials". In: *Science* 238.4826 (1987), p. 551. DOI: 10.1126/science.238.4826.551.

[123] P. A. Gourgiotis and D. Bigoni. "Stress channelling in extreme couple-stress materials Part I: Strong ellipticity, wave propagation, ellipticity, and discontinuity relations". In: *Journal of the Mechanics and Physics of Solids* 88 (2016), pp. 150–168. DOI: https://doi.org/10.1016/j.jmps.2015.09.006.

[124] D. Bigoni and P. A. Gourgiotis. "Folding and faulting of an elastic continuum". In: *Proceedings of the Royal Society A* 472.2187 (2016), p. 20160018. DOI: 10.1098/rspa.2016.0018.

[125] C. Wu, M. Lin, and R. Chen. "The derivation of a bistable criterion for double V-beam mechanisms". In: *Journal of Micromechanics and Microengineering* 23.11 (2013), p. 115005. DOI: 10.1088/0960-1317/23/11/115005.

[126] J. Zhao et al. "Post-buckling and snap-through behavior of inclined slender beams". In: *Journal of Applied Mechanics* 75.4 (2008), p. 041020. DOI: 10.1115/1.2870953.

[127] M. R. Brake et al. "Modeling and measurement of a bistable beam in a microelectromechanical system". In: *Journal of Microelectromechanical Systems* 19.6 (2010), pp. 1503–1514. DOI: 10.1109/JMEMS.2010.2076781.

[128] J. H. Lee et al. "Bistable planar polysilicon microactuator with shallow arch-shaped leaf springs". In: *Micromachined Devices and Components V*. International Society for Optics and Photonics., 1999, pp. 274–280.

[129] I. H. Hwang, Y. S. Shim, and J. H. Lee. "Modeling and experimental characterization of the chevron-type bi-stable microactuator". In: *Journal of Micromechanics and Microengineering* 13.6 (2003), p. 948.

[130] J. Qui and H. Lang. "A curved-beam bistable mechanism". In: *Journal of microelectromechanical systems* 13.2 (2004), pp. 137–146. DOI: 10.1109/JMEMS.2004.825308.

[131] M. Capanu, J. G. Boyd, and P. J. Hesketh. "Design, fabrication, and testing of a bistable electromagnetically actuated microvalve". In: *Journal of Microelectromechanical Systems* 9.2 (2000), pp. 181–189. DOI: 10.1109/84.846698.

[132] B. J. Hansen et al. "Plastic latching accelerometer based on bistable compliant mechanisms". In: *Smart Materials and Structures* 16.5 (2007), p. 1967. DOI: 10.1088/0964-1726/16/5/055.

[133] J. Beharic, T. M. Lucas, and C. K. Harnett. "Analysis of a compressed bistable buckled beam on a flexible support". In: *Journal of Applied Mechanics* 81.8 (2014), p. 081011. DOI: 10.1115/1.4027463.

[134] T. Gomm, L. L. Howell, and R. H. Selfridge. "In-plane linear displacement bistable microrelay". In: *Journal of Micromechanics and Microengineering* 12.3 (2002), p. 257.

[135] M. Hafez, M. D. Lichter, and S. Dubowsky. "Optimized binary modular reconfigurable robotic devices". In: *IEEE/ASME transactions on mechatronics* 8.1 (2003), pp. 18–25. DOI: 10.1109/TMECH.2003.809156.

[136] B. Ando et al. "Investigation on mechanically bistable MEMS devices for energy harvesting from vibrations". In: *Journal of Microelectromechanical Systems* 21.4 (2012), pp. 779–790. DOI: 10.1109/JMEMS.2012.2192912.

[137] M. Hoffman, K. Peter, and V. Edgar. "All-silicon bistable micromechanical fiber switch based on advanced bulk micromachining". In: *IEEE Journal of selected topics in quantum electronics* 5.1 (1999), pp. 46–51. DOI: 10.1109/2944.748104.

[138] X. Sun, K. R. Farmer, and W. N. Carr. "A bistable microrelay based on two-segment multimorph cantilever actuators". In: *Micro Electro Mechanical Systems MEMS 98. Proceedings., The Eleventh Annual International Workshop, IEEE* (1998), pp. 154–159. DOI: 10.1109/MEMSYS.1998.659746.

[139] B. D. Jensen et al. "Design optimization of a fully-compliant bistable micro-mechanism". In: *Ann Arbor MI 48109* 8109.2125 (2001).

[140] E. Kruglick and K. Pister. "Bistable MEMS relays and contact characterization". In: *Proceedings of IEEE Solid-State Sensor Actuator Workshop* (1998), pp. 333–337.

[141] M. Saif and A. Taher. "On a tunable bistable MEMS-theory and experiment". In: *Journal of microelectromechanical systems* 9.2 (2000), pp. 157–170. DOI: 10.1109/84.846696.

[142] M. Vangbo. "Analytical analysis of a compressed bistable buckled beam". In: *Sensors and Actuators A: Physical* 69.3 (1998), pp. 212–216. DOI: https://doi.org/10.1016/S0924-4247(98)00097-1.

[143] Y. Yang and C. J. Kim. "Testing and characterization of a bistable snapping microactuator based on thermo-mechanical analysis". In: *IEEE* 2 (1995), pp. 337–340. DOI: 10.1109/SENSOR.1995.721815.

[144] B. Wagner et al. "Bistable microvalve with pneumatically coupled membranes". In: *IEEE* (1996), pp. 384–388. DOI: 10.1109/MEMSYS.1996.494012.

[145] H. Nan and R. Burgueno. "Buckling-induced smart applications: recent advances and trends". In: *Smart Materials and Structures* 24.6 (2015), p. 063001. DOI: 10.1088/0964-1726/24/6/063001.

[146] B. Shaw and S. Dirven. "Investigation of porosity and mechanical properties of nylon SLS structures". In: *IEEE* (2016), pp. 1–6. DOI: 10.1109/M2VIP.2016.7827297.

[147] Midwest Prototyping LLC. "Midwest Prototyping". URL: https://midwestproto.com/.

[148] Midwest Prototyping LLC. "Selective Laser Sintering (SLS)". 2017. URL: https://midwestproto.com/SLS.

[149] B. M. Tymrak, M. Kreiger, and J. M. Pearce. "Mechanical properties of components fabricated with open-source 3-D printers under realistic environmental conditions". In: *Materials & Design* 58 (2014), pp. 242–246. DOI: https://doi.org/10.1016/j.matdes.2014.02.038.

[150] P. Cruz et al. "Tensile strengths of polyamide based 3D printed polymers in liquid nitrogen". In: *IOP Publishing* 102.1 (2015), p. 012020. DOI: 10.1088/1757-899X/102/1/012020.

[151] ASTM. "Standard Test Method for Tensile Properties of Plastics". URL: https://www.astm.org/Standards/D638.htm.

[152] Midwest Prototyping LLC. "Compare All Materials". URL: https://www.midwestproto.com/sites/midwestproto.com/assets/files/default/PA2200_updated.pdf.

[153] R. S. Lakes. *Viscoelastic materials*. New York NY: Cambridge University Press, 2009.

[154] B. Berman. "3-D printing: the new industrial revolution". In: *Business horizons* 55.2 (2012), pp. 155–162.

[155] J. L. Chulilla-Cano. "The cambrian explosion of popular 3D printing". In: *International Journal of Interactive Multimedia and Artificial Intelligence* 1.4 (2011), pp. 30–32.

[156] Wikimedia Commons. "The differences between CAD and STL Models". 2016. URL: https://commons.wikimedia.org/wiki/File:The_differences_between_CAD_and_STL_Models.svg.

[157] Additively. "Fused Deposition Modeling (FDM)". 2016. URL: https://www.additively.com/en/learn-about/fused-deposition-modeling.

[158] Additively. "Stereolithography (SLA)". 2016. URL: https://www.additively.com/en/learn-about/stereolithography.

[159] Additively. "Laser Sintering (LS)". 2016. URL: https://www.additively.com/en/learn-about/laser-sintering.

[160] Additively. "Material Jetting (MJ)". 2016. URL: https://www.additively.com/en/learn-about/material-jetting.

[161] Additively. "Binder Jetting (BJ)". 2016. URL: https://www.additively.com/en/learn-about/binder-jetting.

[162] Additively. "Laser Melting (LM)". 2016. URL: https://www.additively.com/en/learn-about/laser-melting.

[163] University of Wisconsin-Madison. "3D Printing". 2018. URL: http://3Dprinting.wisc.edu/.

[164] Team Lab. "3D printing". 2018. URL: https://teamlab.engr.wisc.edu/services/3d-printing.

[165] Stratasys. "FDM Technology". 2016. URL: http://www.stratasys.com/fdm-technology.

[166] Stratasys. "ABSplus Material Property". 2016. URL: http://www.stratasys.com/materials/search/absplus.

[167] Stratasys. "Dimension Elite 3D Printer". 2016. URL: http://www.stratasys.com/3D-printers/design-series/dimension-elite.

[168] 3D Systems. "Accura 60 (SLA)". 2018. URL: https://www.3dsystems.com/materials/accura-60.

[169] Midwest Prototyping LLC. "SLA Capabilities". 2017. URL: https://www.midwestproto.com/SLA-Build-Specs.

[170] Midwest Prototyping LLC. "SLA Materials". URL: https://www.midwestproto.com/SLA-Materials.

[171] Midwest Prototyping LLC. "SLS Materials". URL: https://www.midwestproto.com/SLS-Materials.

[172] Midwest Prototyping LLC. "FDM Materials". URL: https://www.midwestproto.com/Technologies/FDM-Materials.

[173] Midwest Prototyping LLC. "Polyjet Materials". URL: https://www.midwestproto.com/Technologies/Objet-Materials.

[174] M. Vaezi, H. Seitz, and S. Yang. "A review on 3D micro-additive manufacturing technologies". In: *The International Journal of Advanced Manufacturing Technology* 67.5-8 (2013), pp. 1721–1754. DOI: http://dx.doi.org/10.1007/s00170-013-4962-5.